

UCSF

UC San Francisco Electronic Theses and Dissertations

Title

Infrared Methods for Lesion Activity Assessment

Permalink

<https://escholarship.org/uc/item/40f7r5rk>

Author

Chang, Nai-Yuan Nicholas

Publication Date

2022

Peer reviewed|Thesis/dissertation

Infrared Methods for Lesion Activity Assessment

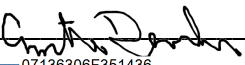
by
Nai-Yuan Nicholas Chang

DISSERTATION
Submitted in partial satisfaction of the requirements for degree of
DOCTOR OF PHILOSOPHY

in
Oral and Craniofacial Sciences

in the
GRADUATE DIVISION
of the
UNIVERSITY OF CALIFORNIA, SAN FRANCISCO

Approved:


DocuSigned by:

07136306F351436... Cynthia Darling
Chair

DocuSigned by:

Daniel Fried

DocuSigned by:

DONALD A. CURTIS

DocuSigned by:

44B728A7773C418... Ram Vaderhobli

Committee Members

Copyright 2022

by

Nai-Yuan Nicholas Chang

DEDICATION

To my mother, Crystal, my father, Joey, my brother, Nelson, and my wife, Leticia

ACKNOWLEDGEMENTS

This work was supported by NIH/NIDCR grants F30-DE027264, R01-DE027335, R01-DE014698, R01-DE028295, and T32-DE007306.

First, I am extremely grateful for Dr. Daniel Fried, my dissertation advisor. I could not have completed my training without his constant guidance and support. For the past seven years, his enthusiasm, knowledge, patience, and care fostered an environment where I could freely think, learn, and succeed. Thank you Dr. Fried.

I would also like to thank the members of my Dissertation and Qualifying Exam committees: Drs. Cynthia Darling, Don Curtis, and Ram Vaderhobli; Drs. Michal Staninec, Duygu Tosun-Turgut, and Andrew Jheon. I am grateful for their invaluable advice throughout my research and clinical career development.

In addition, I want to thank the current and past members of Dr. Fried's lab who contributed to my academic achievements: Dr. Robert Lee, Dr. Andrew Jang, Dr. Kenneth Chan, Dr. Jacob Simon, Dr. Marwa Abdelaziz, Dr. Oanh Le, Jamison Jew, Vincent Yang, Yihua Zhu, Tina Dillas, William Fried, John Tressel, Filipp Kashirtsev, and the summer dental students and clinical residents. My work could not have been completed without their tremendous help.

I am thankful to my graduate advisor, Dr. Wenhan Chang, my clinical coach, Dr. Kim Morita, my group practice leader, Dr. Ana Casal, and the program directors of the Oral and Craniofacial Science (OCS) program, Drs. Pam Den Besten and Ralph Marcucio for their guidance throughout my training. I am also thankful to Roger Mraz, the late Kathryn Gabriel, and Sujata Lama for their administrative support necessary for my progress throughout the training.

Finally, I would like to acknowledge the following scientific journals and their publishers for their permission to use the following publications within this dissertation:

Chapter II

Used with permission from Society of Photo-optical Instrumentation Engineers:

Chang NY, Jew JM, Fried D (2018) Lesion dehydration rate changes with the surface layer thickness during enamel remineralization. In *Lasers in Dentistry XXIV* (Vol. 10473, p. 104730D). International Society for Optics and Photonics

Chapter III

Used with permission from Society of Photo-optical Instrumentation Engineers:

Chang NY, Tressel J, Kashirtsev F, & Fried D. (2022) Use of SWIR dehydration and OCT to assess the complete arrest of simulated incipient caries lesions. In *Proc. of SPIE Vol* (Vol. 11942, pp. 119420A-1). International Society for Optics and Photonics.

Chapter IV

Used with permission from Society of Photo-optical Instrumentation Engineers:

Chang NY, Abdelaziz M, Fried D (2019) The relationship of dehydration rate and transparent surface layer thickness for coronal lesions on extracted teeth. In *Lasers in Dentistry XXV* (Vol. 10857, p. 108570D). International Society for Optics and Photonics.

Chapter V

Used with permission from Society of Photo-optical Instrumentation Engineers:

Chang NY, Dillas T, & Fried D. (2022) Assessing lesion activity of secondary lesions on extracted teeth by thermal dehydration measurement and optical coherence tomography. In *Proc. of SPIE Vol* (Vol. 11942, pp. 1194204-1). International Society for Optics and Photonics.

Chapter VI

Used with permission from Society of Photo-optical Instrumentation Engineers:

Yang VB, Chang NY, Fried D (2020) A thermal imaging handpiece for the clinical assessment of lesion activity on root surfaces via dehydration. In *Lasers in Dentistry XXVI* (Vol. 11217, p. 112170H). International Society for Optics and Photonics.

Fried WA, Zhu Y, Yang V, Chang NY, Fried D (2020) A SWIR imaging handpiece for the clinical assessment of lesion activity via dehydration: preclinical assessment. In *Lasers in Dentistry XXVI* (Vol. 11217, p. 112170I). International Society for Optics and Photonics.

Chapter VII

Used with permission from Society of Photo-optical Instrumentation Engineers:

Chang NY, Zhu Y, Curtis D, Le O, Yang V, Fried WA, Simon JC, Banan P, Darling CY, Fried D. (2020) SWIR, thermal and CP-OCT imaging probes for the in vivo assessment of the activity of root caries lesions. In *Lasers in Dentistry XXVI* (Vol. 11217, p. 1121708). International Society for Optics and Photonics.

Used with permission from SAGE Journals:

Yang V, Zhu Y, Curtis D, Le O, Chang N., Fried WA, Simon JC, Banan P, Darling CL, & Fried D. (2020) Thermal Imaging of Root Caries In Vivo. *Journal of dental research*, 99(13), 1502–1508. <https://doi.org/10.1177/0022034520951157>

ABSTRACT

Infrared Methods for Lesion Activity Assessment

Nai-Yuan Nicholas Chang

Dental caries is one of the most prevalent chronic diseases affecting populations worldwide. With the prevalence of tooth-matched restorative options, the occurrences of recurrent and secondary caries have dramatically increased due to leakage in the interfaces between restorative materials and tooth structure, allowing fluid and bacterial acid infiltration. It is not sufficient to simply detect carious lesions; methods are needed to assess the activity of the lesion and determine if chemical or surgical intervention is necessary. Previous studies have demonstrated the potential of non-ionizing optical imaging technologies for the early detection and diagnosis of lesion severity and depth. The purpose of my project is to quantify the structural differences between active carious and arrested lesions using optical imaging methods. The goal is to provide imaging methods to better assess lesion activity to avoid unnecessary surgical intervention and to allow safe routine monitoring of dental caries without radiation exposure.

All carious lesions have a surface layer due to the occurrence of some redeposition of mineral during lesion formation. For arrested lesions, the surface layer has a much higher mineral content due to additional mineral deposition during remineralization, which leads to decreased permeability of fluids including water and plaque generated acids. The higher mineral content can approach that of sound tissues and can produce a zone that appears more transparent to visible, near-IR and SWIR light, called a transparent surface zone. Previous *in vitro* and *in vivo* studies on enamel and root surfaces have shown that the thickness of this transparent surface zone can be measured nondestructively using optical coherence tomography (OCT). Other studies also have demonstrated that short-wave infrared (SWIR) reflectance and thermal imaging coupled with dehydration can be used to measure changes in the permeability of lesions in enamel and dentin. However, it has not been established how thick the surface zone should be to inhibit the penetration of these fluids.

In these studies, SWIR reflectance and thermal imaging during dehydration with forced air were used to measure changes in the permeability of lesion structure. SWIR imaging at 1400-2300 nm wavelengths coincides with higher water absorption and exploits the increased contrast caused by loss of water from porous lesion areas. Thermal imaging at 6-10 μm wavelengths is sensitive to changes in temperature on tooth surfaces produced by water evaporation from porous lesion areas during dehydration. SWIR reflectance and thermal imaging were used to image simulated enamel and dentin lesions, primary coronal lesions on extracted teeth, and secondary lesions on extracted teeth. The lesions were also assessed by optical coherence tomography (OCT) and correlated with dehydration rates to determine lesion activity. Micro-computed tomography (MicroCT) was used to further confirm lesion severity and structure.

The results from these studies suggest that the relationship between surface layer thickness and lesion permeability is highly non-linear, but significantly negatively correlated. A small increase in the surface layer thickness may lead to a significant decrease in permeability. Increasing transparent surface layer thickness led to decreased permeability of lesions, potentially indicating an arrest in activity at thicknesses exceeding 70 μm . Permeability measurements performed best on smooth surface lesions. Based on these results, custom handheld probes employing SWIR, thermal, and OCT imaging were fabricated for small feasibility studies for *in vivo* assessment of lesion activity in patients. Infrared imaging may significantly improve caries diagnosis and management. These technologies are suitable to produce portable handheld instruments to detect and monitor decay without ionizing-radiation and to increase dental outreach globally.

TABLE OF CONTENTS

CHAPTER I: INTRODUCTION	1
1.1 Clinical Significance	2
1.2 Transparent Surface Layer and Lesion Permeability and Activity	4
1.3 Permeability Measurement and Secondary Lesion Activity	6
1.4 Permeability Measurement Probes for Clinical Lesion Activity Assessment	7
1.5 Overall Objective and Hypotheses	8
1.6 Figures and Figure Legends	9
CHAPTER II: LESION DEHYDRATION RATE CHANGES WITH THE SURFACE LAYER THICKNESS DURING ENAMEL REMINERALIZATION	16
2.1 Summary	17
2.2 Introduction	17
2.3 Materials and Methods	19
2.3.1 Sample Block Preparation	19
2.3.2 Demineralization and Remineralization	20
2.3.3 SWIR Dehydration Measurements	20
2.3.4 Thermal Dehydration Measurements	21
2.3.5 Polarization-Sensitive Optical Coherence Tomography (PS-OCT).....	22
2.3.6 Data Analysis.....	23
2.4 Results and Discussion	23
2.4.1 SWIR Dehydration Measurements	23
2.4.2 SWIR Dehydration Measurements	23
2.4.3 PS-OCT Measurements	24
2.5 Conclusions	25
2.6 Figures and Figure Legends	26

CHAPTER III: USE OF SWIR DEHYDRATION AND OCT TO ASSESS THE COMPLETE ARREST OF SIMULATED INCIPIENT CARIES LESIONS	32
3.1 Summary	33
3.2 Introduction	33
3.3 Materials and Methods	35
3.3.1 Sample Preparation.....	35
3.3.2 Visible/Color Images.....	36
3.3.3 Optical Coherence Tomography	36
3.3.4 SWIR Dehydration Measurements	37
3.4 Results and Discussion.....	38
3.5 Conclusions.....	39
3.6 Figures and Figure Legends	40
CHAPTER IV: THE RELATIONSHIP OF DEHYDRATION RATE AND TRANSPARENT SURFACE LAYER THICKNESS FOR CORONAL LESIONS ON EXTRACTED TEETH.....	44
4.1 Summary	45
4.2 Introduction	45
4.3 Materials and Methods	47
4.3.1 Extracted Tooth Samples	47
4.3.2 Short-Wave Infrared (SWIR) Dehydration Measurements	47
4.3.3 Optical Coherence Tomography (OCT).....	48
4.4 Results and Discussions.....	49
4.4.1 SWIR Dehydration Measurements	49
4.4.2 OCT Measurements	49
4.5 Conclusions.....	50
4.6 Figures and Figure Legends	51

CHAPTER V: <i>EX VIVO</i> ASSESSMENT OF SECONDARY ENAMEL LESION ACTIVITY BY SWIR AND THERMAL DEHYDRATION, OPTICAL COHERENCE TOMOGRAPHY, AND MICROCT	55
5.1 Summary	56
5.2 Introduction	56
5.3 Materials and Methods	59
5.3.1 Sample Preparation.....	59
5.3.2 Visible Imaging	60
5.3.3 SWIR Reflectance Dehydration Measurements.....	60
5.3.4 Thermal Dehydration Measurements	61
5.3.5 Optical Coherence Tomography	62
5.3.6 MicroCT Analysis & Evaluation	63
5.3.7 Data and Statistical Analysis	63
5.4 Results	63
5.4.1 SWIR Dehydration Measurements.....	63
5.4.2 Thermal Dehydration Measurements	64
5.4.3 OCT Imaging	65
5.4.4 MicroCT Imaging	65
5.4.5 Correlation of Thermal and SWIR Imaging with OCT and MicroCT Measurements.....	65
5.5 Discussion	67
5.6 Conclusions.....	71
5.7 Figures and Figure Legends	73
CHAPTER VI: <i>EX VIVO</i> EVALUATION OF SWIR AND THERMAL IMAGING PROBES FOR THE ASSESSMENT OF THE ACTIVITY OF CORONAL AND ROOT CARIES LESIONS	86

6.1 Summary	87
6.2 Introduction	87
6.3 Materials and Methods	91
6.3.1 Sample Preparation.....	91
6.3.2 Design and Fabrication of SWIR and Thermal Dehydration Imaging Probes	91
6.3.3 SWIR Dehydration Measurements.....	92
6.3.4 Thermal Dehydration Measurements	93
6.3.5 Analysis of SWIR Intensity-Time Curves.....	93
6.3.6 Analysis of Thermal Emission Curves.....	93
6.3.7 Optical Coherence Tomography (OCT).....	95
6.3.8 Data Analyses	95
6.4 Results and Discussion	95
6.4.1 Lesion Activity Assessment by SWIR Dehydration Probe.....	95
6.4.2 Lesion Activity Assessment by Thermal Dehydration Probe	96
6.5 Conclusions	96
6.6 Figures and Figure Legends	98
 CHAPTER VII: SWIR, THERMAL, AND CP-OCT IMAGING PROBES FOR THE <i>IN VIVO</i>	
ASSESSMENT OF THE ACTIVITY OF ROOT CARIES LESIONS	
7.1 Summary	107
7.2 Introduction	107
7.3 Materials and Methods	110
7.3.1 Participant Recruitment and Procedures.....	110
7.3.2 SWIR Reflectance (1450-1750 nm) Dehydration Handpiece	111
7.3.3 Thermal Imaging Dehydration Handpiece.....	112
7.4 Results and Discussion	114
7.5 Conclusions	117

7.6 Figures and Figure Legends	119
CHAPTER VIII: SUMMARY AND FUTURE PERSPECTIVE.....	127
8.1 Summary.....	128
8.2.1 <i>In Vitro</i> Lesion Activity Assessments.....	129
8.2.2 <i>Ex Vivo</i> Lesion Activity Assessments	130
8.2.3 <i>In Vivo</i> Lesion Activity Assessments	131
8.2 Future Perspective.....	132
REFERENCES	134

LIST OF FIGURES

CHAPTER I: INTRODUCTION

Figure 1.1 Optical relationship between SWIR spectrum and attenuation in enamel	9
Figure 1.2 The intensity change (ΔI) in reflectance at 1450 nm in bovine enamel during air-drying after demineralization and remineralization	10
Figure 1.3 The time-temperature change (ΔQ) in thermal imaging of bovine dentin during air-drying after demineralization and remineralization	11
Figure 1.4 PS-OCT b-scan images of a bovine enamel block with various remineralization duration	12
Figure 1.5 SWIR images of a posterior tooth with occlusal composite restoration	13
Figure 1.6 <i>In vivo</i> SWIR imaging of two posterior teeth with composite restoration and secondary lesions	14
Figure 1.7 Schematics of handheld probes for <i>in vivo</i> SWIR reflectance and thermal dehydration permeability measurement.....	15

CHAPTER II: LESION DEHYDRATION RATE CHANGES WITH THE SURFACE LAYER THICKNESS DURING ENAMEL REMINERALIZATION

Figure 2.1 Workflow of the experimental setup.....	26
Figure 2.2 Average dehydration curves from 1500-1700 nm.....	27
Figure 2.3 Average thermal dehydration curves	28
Figure 2.4 Sample PS-OCT B-scan of an enamel block.....	29
Figure 2.5 Correlation plot for enamel lesion permeability and TSL	30
Figure 2.6 Correlation plot for dentin lesion permeability and TSL	31

CHAPTER III: USE OF SWIR DEHYDRATION AND OCT TO ASSESS THE COMPLETE ARREST OF SIMULATED INCIPIENT CARIES LESIONS

Figure 3.1 OCT b-scans of a sample taken after 6, 12, 18, and 32 days.....	40
--	----

Figure 3.2 Plots of integrated reflectivity and lesion depth over remineralization duration	42
Figure 3.3 Plots of ΔR , TSL, and ΔI and I_{AUC} at 1950 nm throughout remineralization	43
CHAPTER IV: THE RELATIONSHIP OF DEHYDRATION RATE AND TRANSPARENT SURFACE LAYER THICKNESS FOR CORONAL LESIONS ON EXTRACTED TEETH	
Figure 4.1 Workflow of the experimental setup	51
Figure 4.2 Average permeability curves from 1695-nm LP	52
Figure 4.3 Sample OCT B-scans of active and arrested lesions	53
Figure 4.4 Correlation between SWIR permeability and OCT measurements	54
CHAPTER V: EX VIVO ASSESSMENT OF SECONDARY ENAMEL LESION ACTIVITY BY SWIR AND THERMAL DEHYDRATION, OPTICAL COHERENCE TOMOGRAPHY, AND MICROCT	
Figure 5.1 Workflow schematic	73
Figure 5.2 Permeability measurement setup	74
Figure 5.3 SWIR dehydration analysis results for one of the sample lesions	75
Figure 5.4 Thermal dehydration analysis results for the same sample lesion shown in Fig. 5.3	78
Figure 5.5 OCT scan of the same sample depicted in Fig. 5.3	79
Figure 5.6 MicroCT scan of the same sample depicted in Fig. 5.3	80
Figure 5.7 Correlation Plot: TSL vs. SWIR Permeability	81
Figure 5.8 Correlation Plot: TSL vs. Thermal Permeability	82
Figure 5.9 Correlation Plot: TSL vs. SL	83
Figure 5.10 Smooth Surface Lesion Correlation Plots: TSL vs. SWIR Permeability	84
Figure 5.11 Smooth Surface Lesion Correlation Plots: TSL vs. Thermal Permeability	85

CHAPTER VI: EX VIVO EVALUATION OF SWIR AND THERMAL IMAGING PROBES FOR THE ASSESSMENT OF THE ACTIVITY OF CORONAL AND ROOT CARIES

LESIONS

Figure 6.1 3D Printed SWIR Imaging Probe 98

Figure 6.2 3D Printed Thermal Imaging Prototype..... 99

Figure 6.3 Thermal images over time 100

Figure 6.4 Thermal imaging processing steps 101

Figure 6.5 Sample thermal dehydration curve plot 102

Figure 6.6 SWIR reflectance images throughout dehydration 103

Figure 6.7 Mean SWIR dehydration curves 104

Figure 6.8 OGR between active and arrested lesions 105

CHAPTER VII: SWIR, THERMAL, AND CP-OCT IMAGING PROBES FOR THE IN VIVO

ASSESSMENT OF THE ACTIVITY OF ROOT CARIES LESIONS

Figure 7.1 Imaging Probes Used 119

Figure 7.2 Two CP-OCT b-scans of root caries lesions 120

Figure 7.3 Two thermal and visible images of root caries lesions..... 121

Figure 7.4 Visible, thermal, and CP-OCT images of a shallow active root lesion 123

Figure 7.5 Visible, thermal, and CP-OCT images of a large root lesion with both active
and arrested areas..... 125

Figure 7.6 Comparisons of ΔQ for different lesion zones..... 126

LIST OF TABLES

CHAPTER III. USE OF SWIR DEHYDRATION AND OCT TO ASSESS THE COMPLETE ARREST OF SIMULATED INCIPIENT CARIES LESIONS

Table 3.1 SWIR permeability and OCT measurements throughout remineralization..... 41

CHAPTER I

INTRODUCTION

1.1 Clinical Significance

The nature of dental caries or decay has changed markedly due to the introduction of fluoride to the drinking water, the use of fluoride dentifrices and rinses, and improved dental hygiene. Despite these advances, dental caries remains one of the leading cause of tooth loss in the U.S. (Chauncey et al., 1989; Kaste et al., 1996; Winn et al., 1996) The caries problem has changed with the majority of newly discovered carious lesions being highly localized to the occlusal pits and fissures (Class 1 lesions) of the posterior dentition and the proximal contact sites between teeth (Class 2 lesions) where they are more difficult to detect. Now, with our increasing longevity and the higher carbohydrate content of the modern diet, the incidence of periodontitis and root lesions has increased, making periodontal diseases the leading cause of tooth loss in adults (Eke et al., 2018). New diagnostic tools are needed for the detection and characterization of caries lesions in the early stages and throughout development (Cate & Amerongen, 1996; Featherstone, 1996; Hume, 1996; National Institutes of Health (U.S.), 2001). If carious lesions are detected early enough, it is likely that they can be arrested or reversed by non-surgical means through clinical treatments such as anti-bacterial therapy, fluoride therapy, dietary changes, or by low intensity laser irradiation (Featherstone, 1999; National Institutes of Health (U.S.), 2001); or by patient education and modifying lifestyle factors. Therefore, it is critical to detect the decay in its early stage of development at which point non-invasive preventive measures can be taken to effectively halt further decay.

Conventional methods of caries and lesion activity assessments rely on periapical and bitewing x-rays, and visual and tactile assessments by clinicians, which can greatly differ in diagnoses from clinician to clinician (Fejerskov & Kidd, 2003; Pitts, 2009). We do not fully understand the risk of low-level exposure to ionizing radiation. Even greatly reduced levels of radiation exposure may still pose a significant risk especially for children and pregnant women. Another major limitation of radiographs is its limited use for detecting early occlusal caries lesions due to the overlapping features of the coronal tooth structure anatomy. Lesions are not typically

visible on radiographs until decalcification has exceeded 30% (White & Pharoah, 2014; J. Yang & Dutra, 2005). Therefore, improvements in radiographic sensitivity are unlikely to enable detection of early lesions.

The clinical studies conducted in our lab have demonstrated that short-wave infrared (SWIR) imaging provides a promising alternative for radiography for the routine screening and monitoring of caries lesions on the proximal and occlusal surfaces where almost all lesions are found (Staninec et al., 2010, 2011). It has also been demonstrated that SWIR reflectance measurements at wavelengths coincident with higher water absorption can be used to detect very early demineralization on tooth surfaces at earlier stages than existing methods such as quantitative light fluorescence (QLF) (Wu & Fried, 2009).

Accurate assessment of lesion activity, depth, and severity is important to determine whether intervention is necessary. Effective employment of new optical diagnostic technologies that can exploit the changes in the light scattering of the lesion have great potential for diagnosing the present state of the lesions. Hence, new imaging methodologies are needed to determine whether lesions are active and expanding, partially arrested and undergoing remineralization, or fully arrested and remineralized. Optical Coherence Tomography (OCT) using SWIR light is capable of this task since it provides a measure of the reflectivity from each layer of the lesion and is able to detect the formation of a zone of increased mineral density and reduced light scattering due to remineralization (Jones et al., 2006; Jones & Fried, 2006; Manesh et al., 2009b). Moreover, it has been demonstrated that SWIR reflectance and thermal measurements during lesion dehydration can be used to assess lesions activity (R. C. Lee et al., 2015; R. C. Lee, Darling, Staninec, et al., 2016; R. C. Lee, Staninec, et al., 2016). The permeability to water represents the level of activity of the lesion sites, and thus can be monitored by recording the changes in temperature and reflectivity during dehydration.

Many lesions have been arrested or do not require intervention. However, it is difficult to identify active lesions with current diagnostic methods. Therefore, the development of new

methods, such as SWIR reflectance and thermal dehydration imaging, will help improve the accuracy of lesion activity assessment. Moreover, SWIR and thermal imaging allows more frequent and safer monitoring of lesions, since ionizing radiation is not required. Development of this novel imaging technology will allow the detection and monitoring of early carious lesions, enabling conservative non-surgical intervention and the preservation of healthy tissue structure, and increase patient education and public awareness to dental health.

1.2 Transparent Surface Layer and Lesion Permeability and Activity

Previous studies have demonstrated that the optical changes due to the loss of water from porous lesions can be exploited to assess lesion severity with QLF, thermal, and SWIR imaging (Kaneko et al., 1999; Usenik et al., 2014; Zakian et al., 2010). Since arrested lesions are less permeable to water due to the highly mineralized surface layer (Dean, 2015; R. C. Lee, Darling, & Fried, 2016a; Neville et al., 2015), we hypothesize that changes in the rate of water loss can be related to changes in lesion structure and porosity. SWIR reflectance measurements at wavelengths greater than 1400 nm can yield very high contrast images of demineralization on tooth coronal surfaces including the occlusal pits and fissures. These images are free of interference from stains at wavelengths beyond 1200 nm and manifest large changes in contrast related to changes in lesion structure. A plot of the relationship between SWIR spectrum and attenuation coefficient is shown in **Figure 1.1** (D. Fried et al., 1995; Hale & Query, 1973; Jones & Fried, 2002).

When lesions become arrested by mineral deposition in the outer layers of the lesion, the diffusion of fluids into the lesion is inhibited. Hence, the rate of water diffusion out of the lesion reflects the degree of lesion activity. Artificial and natural lesions on the occlusal and root surfaces manifest a significant and marked decrease in the rate of dehydration if the lesion has a remineralized surface layer indicative of an arrested lesion (R. C. Lee et al., 2015; R. C. Lee, Darling, & Fried, 2016b). We have been investigating optical methods for assessing water diffusion rates from lesions since the porosity of the outer layers of active lesions is significantly

greater than for arrested lesions. This can be indirectly measured via SWIR reflectance and thermal methods (R. C. Lee et al., 2015). Water in the pores at the surface of the lesion absorbs the incident SWIR light and reduces surface scattering, causing reduced lesion contrast. Loss of that water during dehydration causes marked increase in reflectivity and lesion contrast (**Fig. 1.2**).

During lesion dehydration, the vaporization of water from the lesion pores causes a drop in surface temperature in the lesion area, which can be measured with a thermal imaging camera (**Fig. 1.3**). Thermal imaging at wavelengths from 8000 to 13000 nm had the highest diagnostic performance on artificial dentinal lesions and natural root caries lesions (R. C. Lee, Darling, & Fried, 2016b). Unlike SWIR dehydration measurements where a SWIR light source is also needed to illuminate the tooth, thermal imaging does not require an additional light source. However, SWIR reflectance imaging showed better performance than thermal imaging for monitoring the dehydration of enamel lesions but did not perform well on dentin surfaces due to the higher light scattering of sound dentin.

Polarization-sensitive (PS)-OCT has the unique ability to nondestructively measure the thickness of the transparent surface zone formed on the outer surface of root caries lesions after remineralization (Baumgartner et al., 1999; Chen et al., 2005; D. Fried et al., 2002; Hee et al., 1992). In PS-OCT, light incident on the tooth is completely polarized in one polarization state, and the reflected light is collected in one or both orthogonal polarizations, the original polarization called the parallel (\parallel), or co-polarization, image and the perpendicular (\perp), or cross-polarization, image. In the cross-polarization image (CP-OCT), the reflectivity can be directly integrated over the lesion depth without excessive interference from the strong surface reflection at tooth surfaces and there is increased contrast between sound and demineralized tissues. We have demonstrated the ability of PS-OCT to monitor remineralization and the formation of a distinct transparent surface zone on the lesion through several studies utilizing various models of remineralization (Jones et al., 2006; Jones & Fried, 2006; Kang et al., 2012). **Figure 1.4** shows PS-OCT co-polarization (\parallel) and cross polarization (\perp) images of a bovine enamel sample with 6

windows showing sound, lesion, and lesion areas that have been exposed for 4, 8, and 12 days to a remineralization solution.

1.3 Permeability Measurement and Secondary Lesion Activity

In recent years, the prevalence of using shade-matched and radiopaque dental restorative materials for replacing decayed tooth structure after cavity preparation has led to a marked increase in the formation of secondary caries lesions due to several clinical placement factors. Maladaptation of bonding materials to tooth structure permits the microleakage of fluids and bacterial acid, resulting in the demineralization of tooth structure extending beneath the restoration. Moreover, clinicians spend more time replacing restorations than placing new ones and most restorations fail due to secondary caries. As much as 75% of dental restorations are replaced and 25% repaired (Gordan et al., 2012).

SWIR imaging can be used to aid in the detection and visualization of composites that are closely color-matched to the tooth structure (**Fig. 1.5**) (W. A. Fried et al., 2017). Wavelengths longer than 1200 nm avoid interference from stain and exploit the greater transparency of sound enamel and dental composites to provide increased contrast with demineralized tissues (**Fig. 1.6**). Temperature changes on tooth surfaces during air drying have been exploited to assess lesion activity via thermal imaging. Previous studies utilizing thermal dehydration imaging for assessing the activity of lesions on coronal and root surfaces both *in vivo* and *in vitro* have shown considerable promise (Kaneko et al., 1999; R. C. Lee et al., 2015; R. C. Lee, Darling, Staninec, et al., 2016; R. C. Lee, Staninec, et al., 2016; Zakian et al., 2010). In addition, since water tends to pool in gaps and crevices, we postulate that thermal imaging may be able to highlight gaps between restorative materials and tooth structure where there is increased microleakage. Such areas should experience larger temperature drops due to greater water retention in such gaps. In a recent thermal imaging study of root caries lesions, pockets in the gingiva were much cooler than the surrounding tooth structure due to water pooling in such areas (V. Yang et al., 2020).

Therefore, both SWIR and thermal dehydration imaging methods have significant clinical potential for the nondestructive assessment of the activity of secondary caries lesions. Improving caries diagnosis should reduce the unnecessary replacement of composite restorations.

1.4 Permeability Measurement Probes for Clinical Lesion Activity Assessment

Recent advances in IR imaging technologies are providing miniature detectors and imaging components, which allow us to fabricate compact and customizable SWIR reflectance and thermal imaging handpieces designed for *in vivo* dehydration measurements. The handpieces utilize SWIR reflectance to image enamel structures and thermal measurements to image dentin and root structures. The handheld devices were tested on simulated and natural lesions on extracted teeth.

Marked changes occurred in the intensity difference measured using SWIR reflectance at 1450 nm before and after dehydration indicating that we are able to detect significant differences in intensity change after different periods of remineralization. Similar measurements on natural lesions showed a significant and marked decrease in the rate of dehydration if the lesion had a transparent surface layer visible with PS-OCT. For SWIR reflectance, the change in intensity after dehydration was significantly higher ($p < 0.05$) for lesions without a surface zone than for lesions with a transparent surface layer detectable with OCT (R. C. Lee et al., 2015; R. C. Lee, Darling, Staninec, et al., 2016; R. C. Lee, Staninec, et al., 2016).

Studies were also performed on dentin and root surfaces; however, thermal imaging performed much better than SWIR reflectance imaging due to the much higher reflectivity of sound dentin. Using the Autodesk Fusion 360 CAD software and Formlabs 3D printers, compact handheld IR probes were designed and built for *in vivo* dehydration measurements (**Fig. 1.7**). In addition, *in vitro* studies were carried out to evaluate the probes and their ability to monitor lesion activity. Current and future *in vivo* studies will provide further evidence for the potential use of such imaging methodologies in routine clinical examinations.

1.5 Overall Objective and Hypotheses

The overall objective of my dissertation research is to develop methods for the clinical assessment of the structure and activity of caries lesions. Specific *in vitro* and *ex vivo* hypotheses were investigated: First, I tested the hypothesis that the thickness of the highly mineralized transparent surface zone formed during remineralization correlates with the lesion permeability and activity. The results should help establish the correlation between transparent surface layer thickness and lesion permeability to water measured using SWIR reflectance and thermal imaging. The results will determine the minimum transparent surface layer thickness needed to arrest lesions and cause significant changes in the lesion permeability. Second, I tested the hypothesis that thermal and SWIR reflectance dehydration methods can be used to measure the activity of secondary carious lesions around composite restorations. The results will help demonstrate that thermal and SWIR reflectance measurements can be used to nondestructively assess the activity of simulated and natural secondary caries lesions. Third, I tested the hypothesis that compact thermal and SWIR reflectance probes for lesion activity assessment can be fabricated that are suitable for *in vivo* use. The results demonstrate that these hand-held IR probes for measuring lesion activity are suitably compact for clinical use and can perform as well as the benchtop systems. The goal of this work will help determine the structural changes needed to arrest active lesions and provide methods for assessing the activity of lesions in a single examination to avoid unnecessary treatment and cavity preparations.

1.6 Figures and Figure Legends

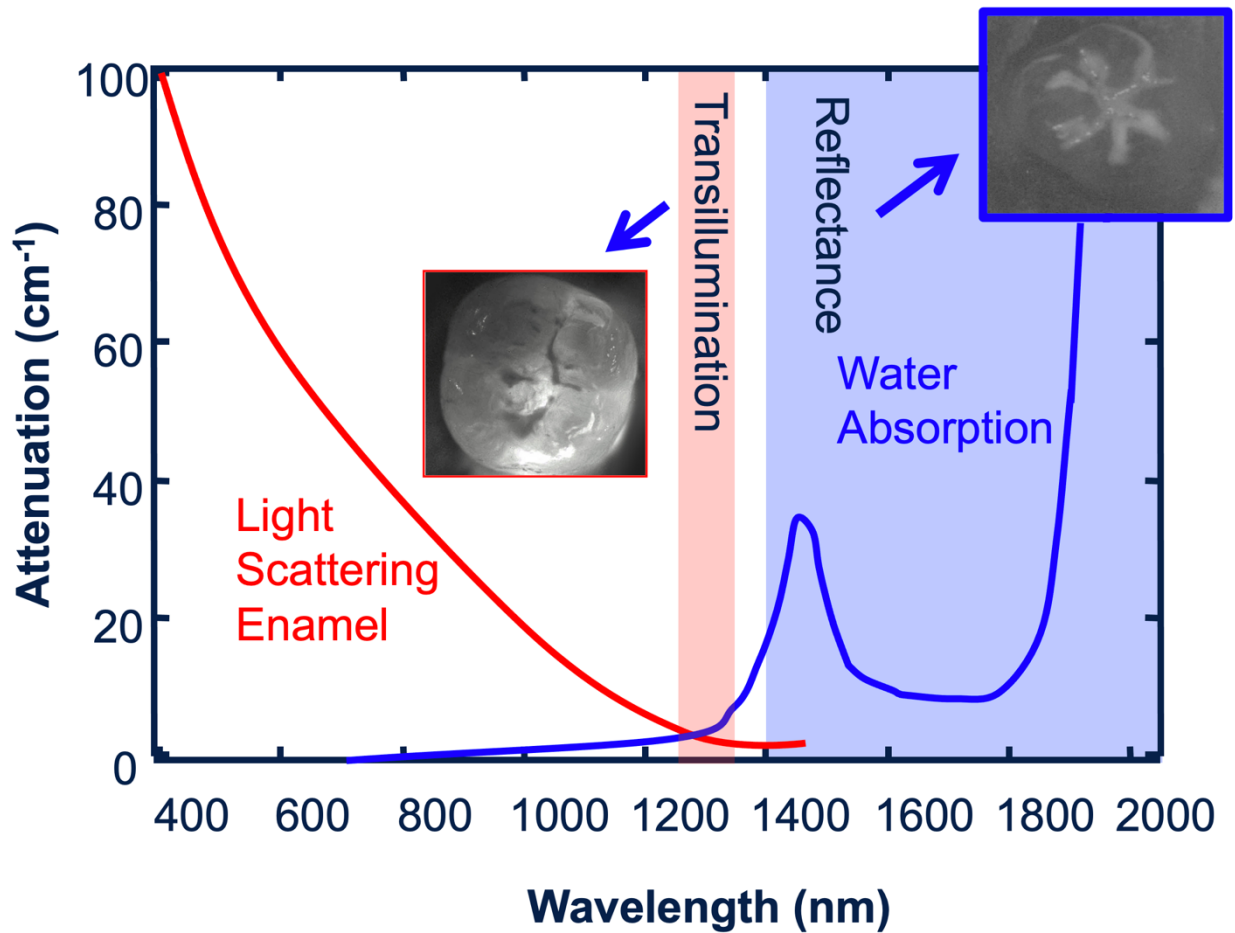


Figure 1.1 Optical relationship between SWIR spectrum and attenuation in enamel
Enamel appears transparent in SWIR spectrum due to low enamel attenuation. Coinciding with high water absorption band, SWIR allows for increased contrast when imaging lesion structures (D. Fried et al., 1995; Hale & Query, 1973; Jones & Fried, 2002).

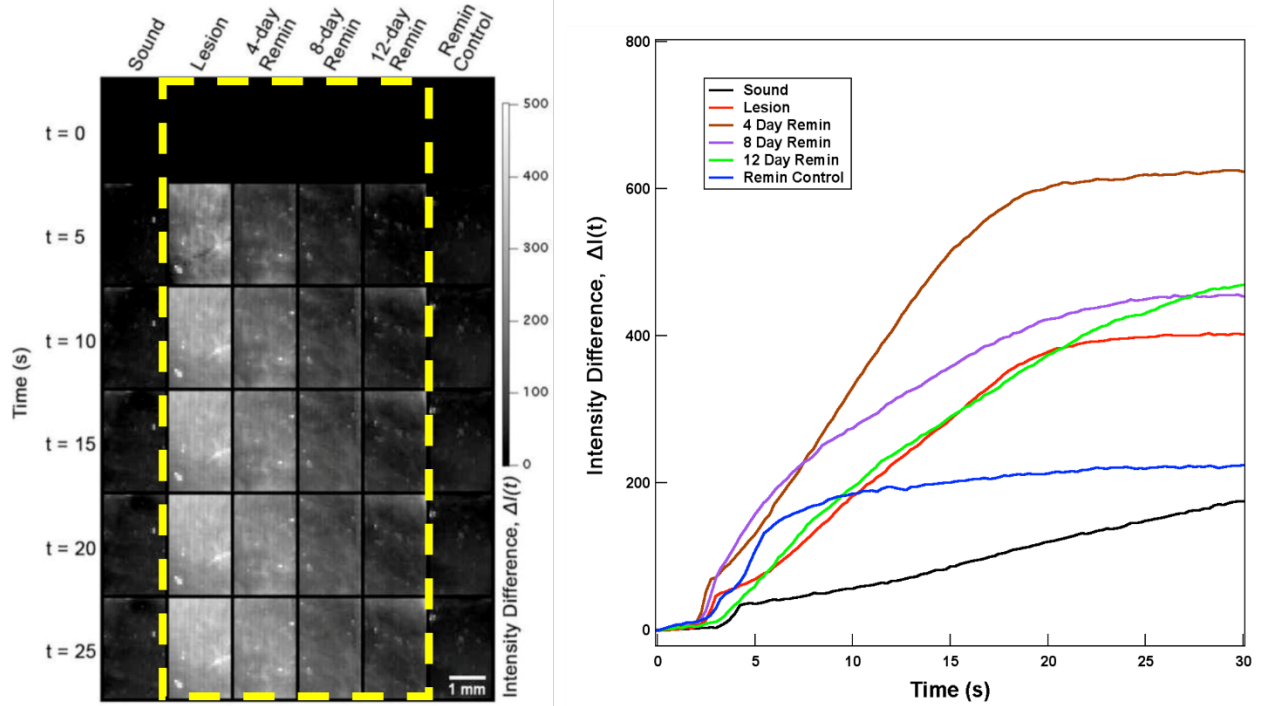


Figure 1.2 The intensity change (ΔI) in reflectance at 1450 nm in bovine enamel during air-drying after demineralization and remineralization

Left: Images of the 6 sample windows of demineralization and various remineralization duration at different drying times. *Right:* SWIR reflectance dehydration time-intensity curves for each window (R. C. Lee et al., 2015).

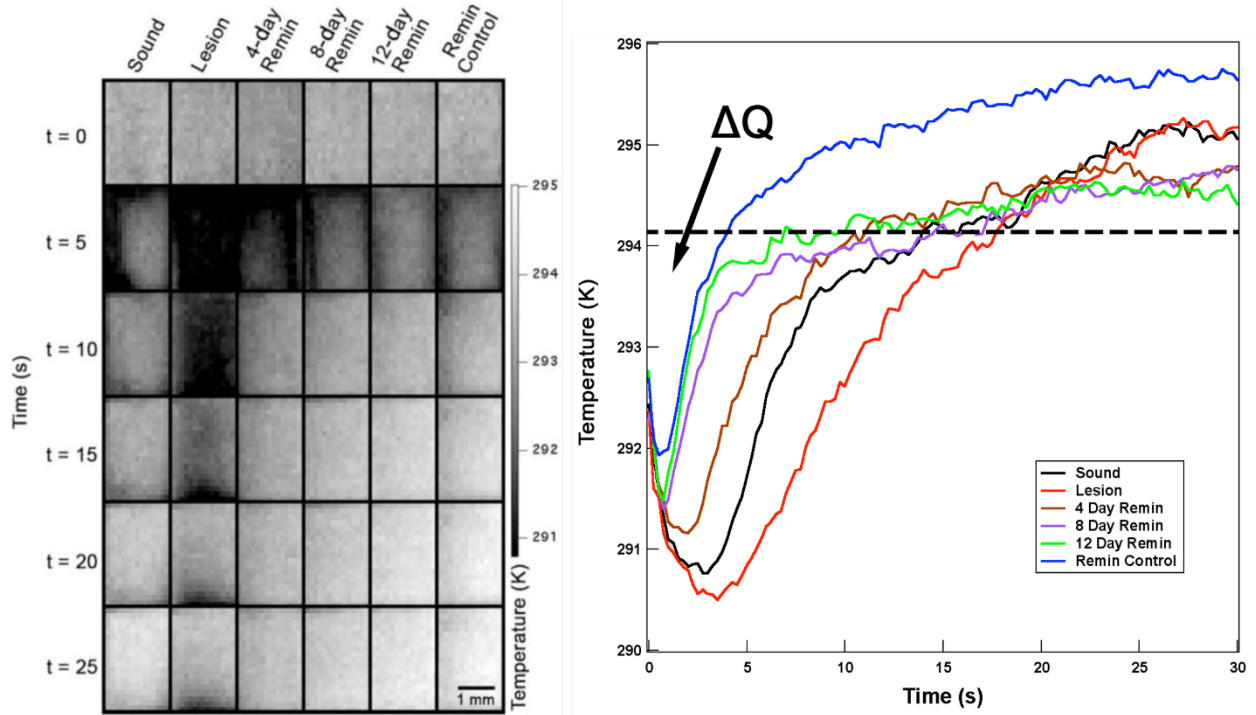


Figure 1.3 The time-temperature change (ΔQ) in thermal imaging of bovine dentin during air-drying after demineralization and remineralization

Left: Images of the 6 sample windows of demineralization and various remineralization duration at different drying times. *Right:* Thermal time-temperature dehydration curves for each window (R. C. Lee et al., 2015).

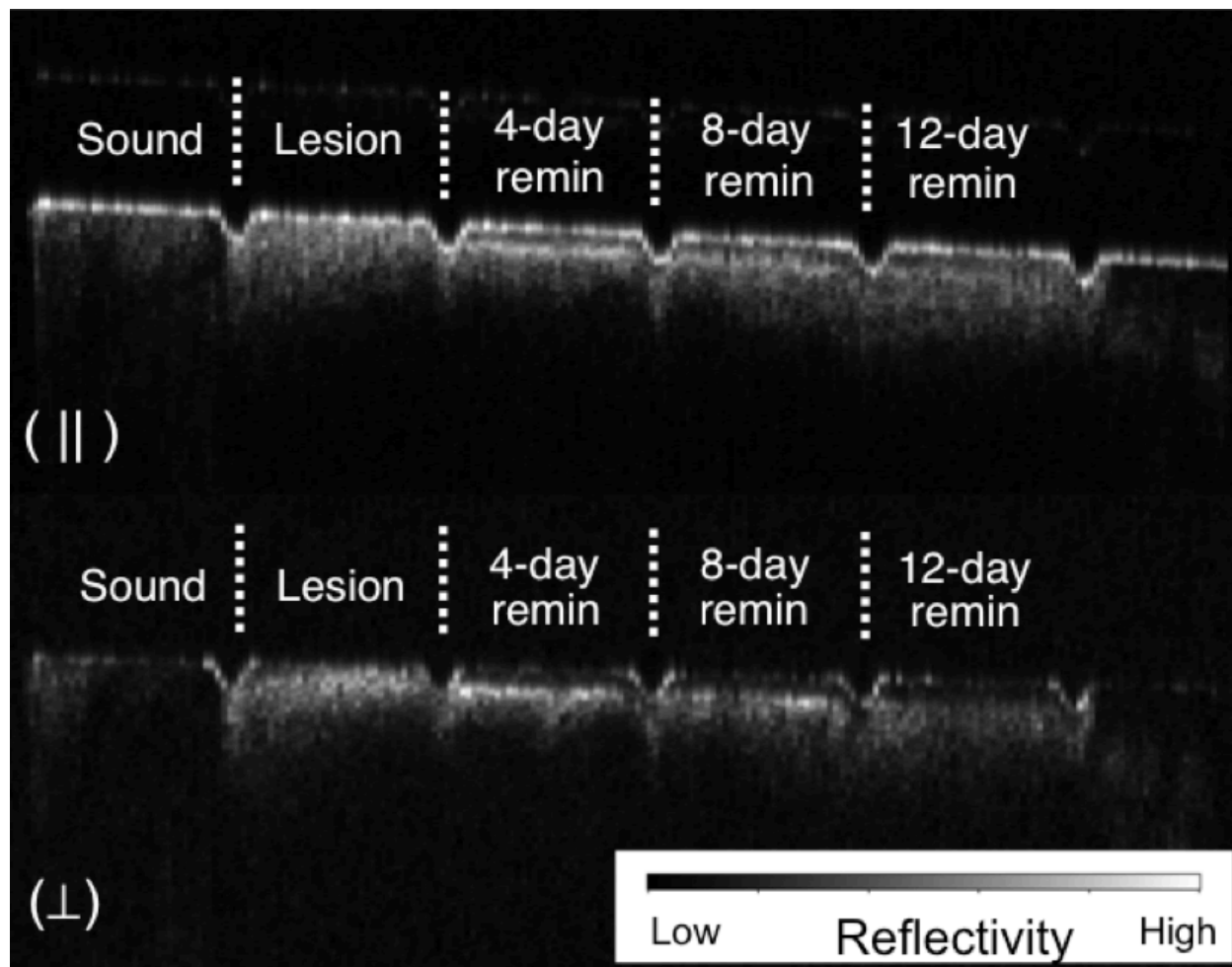


Figure 1.4 PS-OCT b-scan images of a bovine enamel block with various remineralization duration

Image shows the sound (protected) regions located on the extreme left and right side of the sample, the lesion area (0-days exposed to remineralization solution) and the areas exposed for increasing periods of time to the remineralization solution, 4, 8, and 12-days. The (||) image represents the light reflected in the original polarization while the (\perp) image is the orthogonal polarization or cross polarization image which was used for analysis in these studies. The incisions are $\sim 100\text{-}\mu\text{m}$ deep and separated by 1.4-mm (Kang et al., 2012).

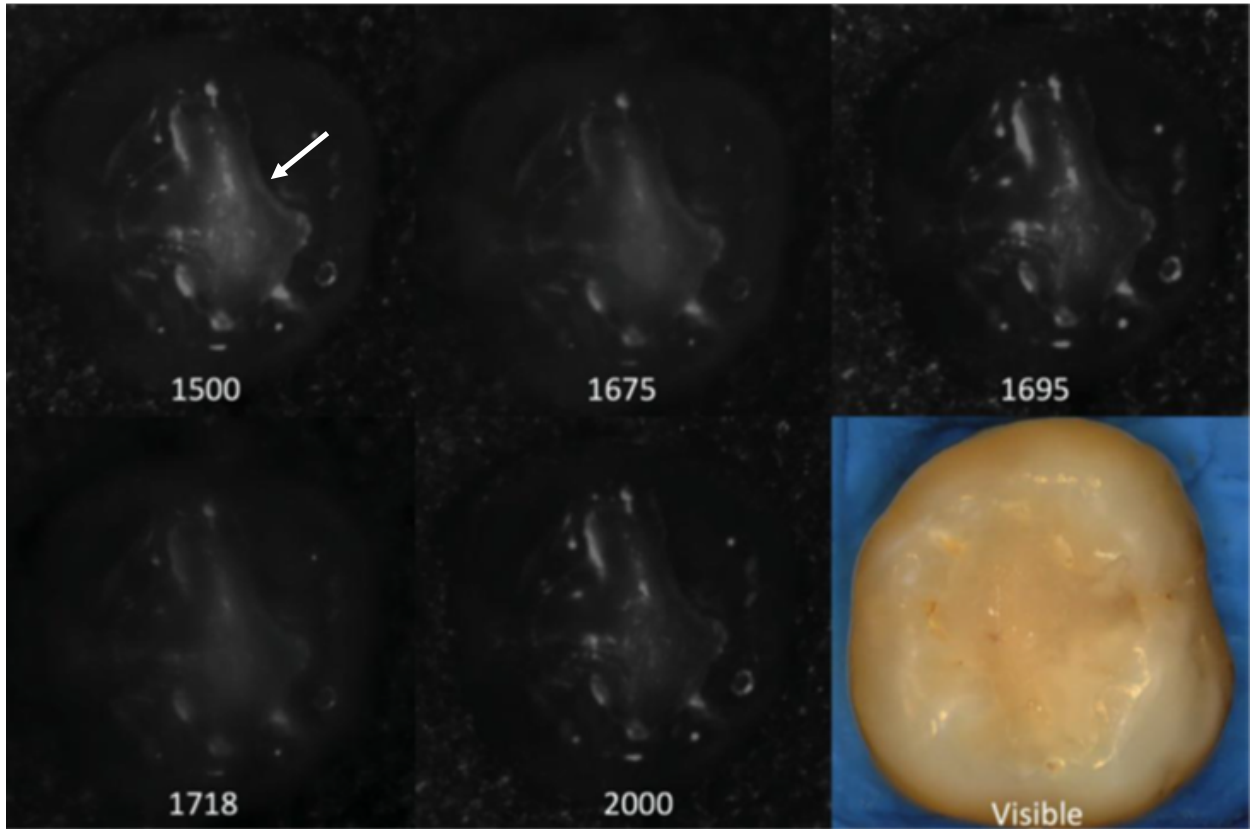


Figure 1.5 SWIR images of a posterior tooth with occlusal composite restoration
Occlusal reflectance images are shown for the 1500-nm, 1675-nm, 1695-nm, 1718-nm, and 2000-nm filters with the extended range InGaAs camera (900-2350-nm) as well as for visible light. Composite restoration is indicated by the white arrow (W. A. Fried et al., 2017).

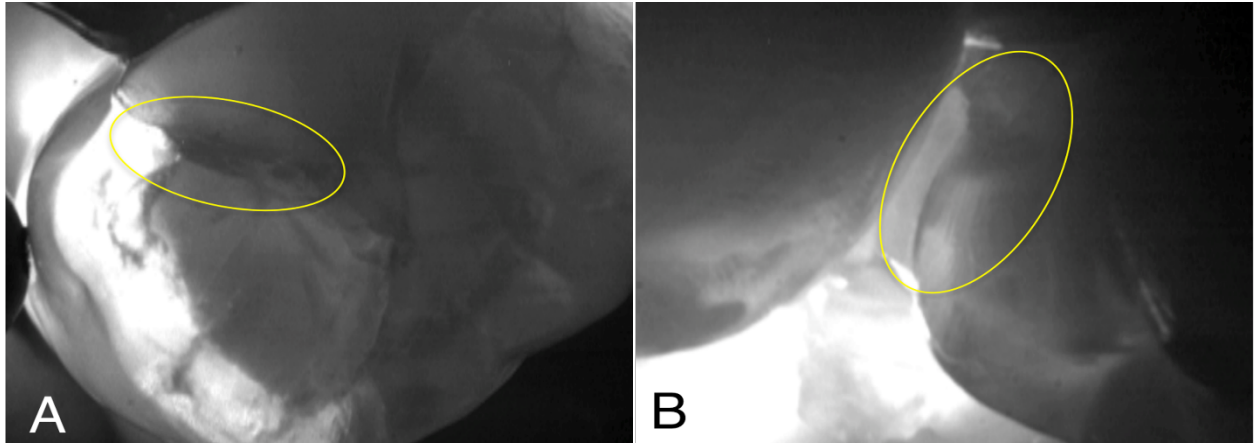


Figure 1.6 *In vivo* SWIR imaging of two posterior teeth with composite restoration and secondary lesions

A: Occlusal secondary lesion. B: Approximal secondary lesion. Lesions are encircled by the yellow circles (Simon et al., 2016).

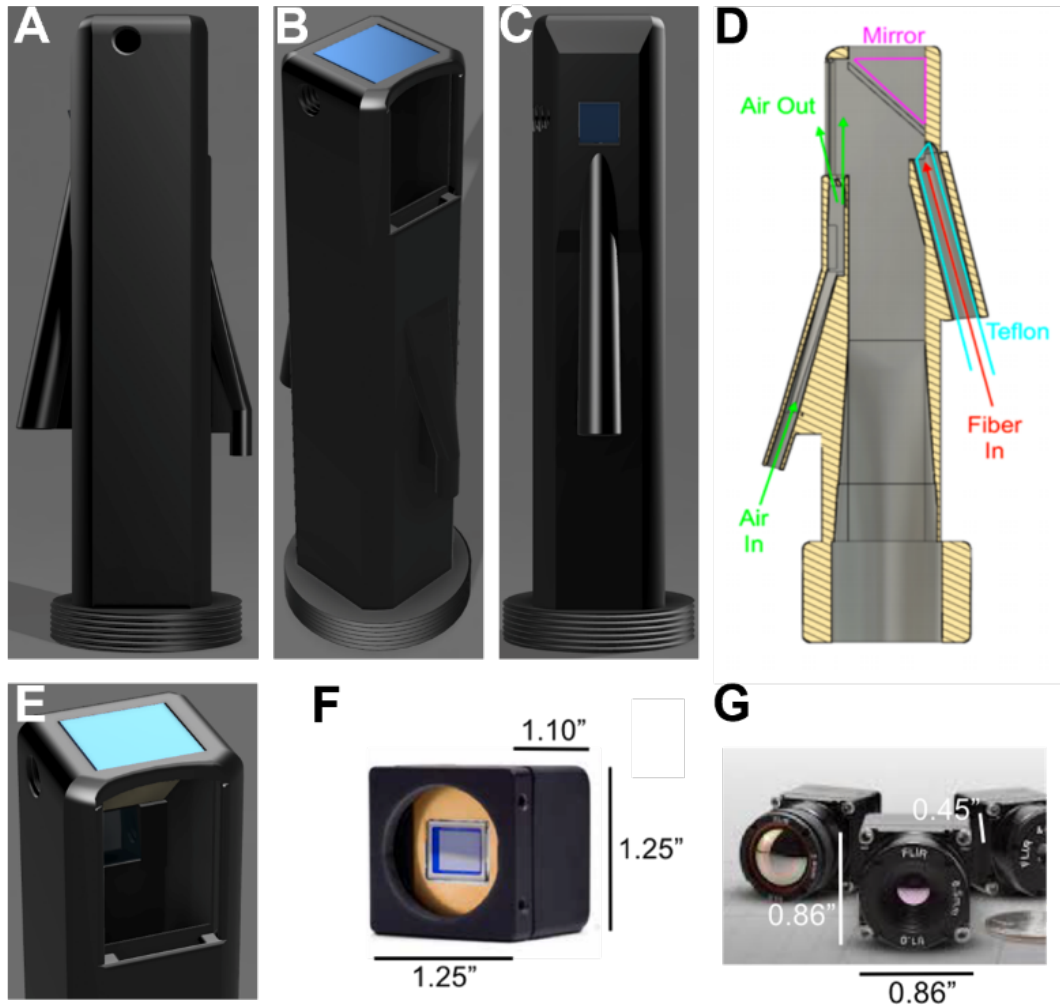


Figure 1.7 Schematics of handheld probes for *in vivo* SWIR reflectance and thermal dehydration permeability measurement

Probes can be attached to existing small SWIR sensor and thermal camera. A-C: 3D CAD rendering of handheld probe at different views. D: Diagram of the components of the handheld probe; fiber for SWIR light source, which will not be used for thermal imaging. E: Close-up view at the imaging window where light deflectors and air vents for dehydration can be seen. F: 640 x 512 element Micro-SWIR camera the 640CSX from Sensors Unlimited. G: 640 x 512 element FLIR Boson microbolometer thermal camera.

CHAPTER II

LESION DEHYDRATION RATE CHANGES WITH THE SURFACE LAYER THICKNESS DURING ENAMEL REMINERALIZATION

2.1 Summary

A transparent highly mineralized outer surface zone is formed on caries lesions during remineralization that reduces the permeability to water and plaque generated acids. However, it has not been established how thick the surface zone should be to inhibit the penetration of these fluids. Shortwave-infrared (SWIR) reflectance coupled with dehydration can be used to measure changes in the fluid permeability of lesions in enamel and dentin. Based on our previous studies, we postulate that there is a strong correlation between the transparent surface layer thickness, to a certain limit, and the rate of dehydration. In this study, the rates of dehydration for simulated lesions in enamel with varying remineralization durations were measured. Reflectance imaging at SWIR wavelengths from 1400-2300 nm, which coincides with higher water absorption and manifests the greatest sensitivity to contrast changes during dehydration measurements, was used to image simulated enamel lesions. The results suggest that the relationship between surface zone thickness and lesion permeability is highly non-linear, and that a small increase in the surface layer thickness may lead to a significant decrease in permeability

2.2 Introduction

The majority of newly discovered carious lesions are highly localized to the occlusal pits and fissures of the posterior dentition and the proximal contact sites between teeth, where they are more difficult to detect. Clinicians mostly rely on palpation and visual inspection to discern whether dental decay is active or arrested (Fejerskov & Kidd, 2003). If the lesion appears dark, smooth, and hard, they would likely decide that the lesion is arrested (Pitts, 2009). However, this method is subjective and unreliable (Fejerskov & Kidd, 2003; Pitts, 2009). Many lesions have been arrested or do not require intervention. Even so, it is difficult to identify active lesions with current diagnostic methods. Accurate assessment of lesion activity (rate of change), depth, and severity is important to determine whether intervention is necessary. Effective employment of new optical diagnostic technologies that can exploit the changes in the light scattering of the lesion have great

potential for diagnosing the present state of the lesions. Therefore, the development of new methods, such as SWIR reflectance dehydration imaging, are needed for the clinical assessment of lesion activity and to avoid unnecessary cavity preparations.

When lesions become arrested by mineral deposition, or remineralization, in the outer layers of the lesion, the diffusion of fluids into the lesion is inhibited. Hence, the rate of water diffusion out of the lesion reflects the degree of lesion activity. Previous studies have demonstrated that the optical changes due to the loss of water from porous lesions can be exploited to assess lesion severity and activity with QLF, thermal, and SWIR imaging (Kaneko et al., 1999; R. C. Lee et al., 2015; R. C. Lee, Darling, Staninec, et al., 2016; R. C. Lee, Staninec, et al., 2016; Ribeiro et al., 2014; Usenik et al., 2014; Zakian et al., 2010). Since arrested lesions and developmental defects (fluorosis) are less permeable to water due to the highly mineralized surface layer, changes in the rate of water loss can be related to changes in lesion structure and porosity. We have investigated optical methods for assessing water diffusion rates from lesions since the porosity of the outer layers of active lesions is significantly greater than arrested lesions. This can be indirectly measured via SWIR reflectance methods (Chung et al., 2011; W. A. Fried et al., 2013; Simon et al., 2014). Normal enamel is transparent in SWIR wavelengths, whereas early demineralization causes increased SWIR reflectance due to scattering. Water in the pores at the surface of the lesion absorbs the incident SWIR light, particularly at wavelengths such as 1450 nm, reducing surface scattering and lesion contrast. Loss of that water during dehydration produces a marked increase in reflectivity and lesion contrast.

During lesion dehydration, the vaporization of water from the lesion pores causes a decrease in surface temperature in the lesion area, which can be measured with a thermal imaging camera. Thermal imaging at wavelengths from 8000 to 13000 nm had the highest diagnostic performance on artificial dentinal lesions and natural root caries lesions (R. C. Lee, Darling, & Fried, 2016b). Based on our previous work, SWIR reflectance imaging showed better performance than thermal imaging for monitoring the dehydration of enamel lesions but did not

perform well on dentin surfaces due to the higher light scattering of sound dentin. Here, we employ both SWIR and thermal reflectance methods to measure the surface dehydration rates of the simulated enamel and dentin lesions, respectively, after exposure to demineralization and subsequent remineralization.

New technologies are also needed to determine whether lesions are active and expanding, partially arrested and undergoing remineralization, or fully arrested and remineralized. Polarization Sensitive-Optical Coherence Tomography (PS-OCT) using SWIR light is capable of this task since it provides a measure of the reflectivity from each layer of the lesion and is able to detect the formation of a zone of increased mineral density and reduced light scattering due to remineralization. Arrested lesions exhibit a well-defined surface zone of reduced reflectivity that can be clearly resolved in OCT images (Jones et al., 2006; Jones & Fried, 2006; Kang et al., 2012).

The purpose of this study is to develop a method to assess lesion activity. We hypothesize that the thickness of the highly mineralized transparent surface zone formed during remineralization correlates with the lesion permeability and activity in enamel. Here, we correlate the results from SWIR reflectance and thermal dehydration measurements and PS-OCT measurements and found that minor changes in surface layer thickness may lead to major changes in fluid permeability in remineralized enamel and dentin lesions. The results here will be confirmed by histology using polarized light microscopy (PLM) and transverse microradiography (TMR).

2.3 Materials and Methods

2.3.1 Sample Block Preparation

Enamel blocks (n = 20) and dentin blocks (n = 20), approximately 10-12 mm in length with a width of 2 mm and a thickness of 2 mm, were prepared from extracted bovine incisors acquired from a

slaughterhouse. Enamel and dentin blocks were ground to a 9 μm finish. Figure 1 shows the workflow of the study design employed.

2.3.2 Demineralization and Remineralization

A thin layer of acid-resistant varnish in the form of nail polish, Revlon 270 (New York, NY), was applied to all sides except the non-control top surfaces of the enamel blocks before exposure to the demineralization solution. Samples were immersed in 40 mL aliquots of the demineralization solution for 24 hours. The demineralization solution, which was maintained at 37°C and pH 4.8, was composed of 2.0 mmol/L calcium, 2.0 mmol/L phosphate, and 75 mmol/L acetate. This dissolution model is a "surface softened" dissolution model designed to produce subsurface dissolution while maintaining an intact surface, and it simulates highly active early lesions of approximately 100-200 μm thick on the surface. A demineralized surface is then covered with the same acid-resistant varnish, where the rest of the samples were exposed to an acidic remineralization regimen for varying duration (**Figure 2.1**). The acidic remineralization model has been successful in increasing mineralization of the lesion body (Yamazaki et al., 2007; Yamazaki & Margolis, 2008). The acidic remineralization solution was composed of 4.1 mmol/L calcium, 15 mmol/L phosphate, 50 mmol/L lactic acid, 20 mmol/L HEPES buffer, and 2 ppm F⁻ maintained at 37°C and a pH of 4.8 (Yamazaki & Margolis, 2008). After each time point of remineralization, beginning at 0 hour of remineralization, SWIR reflectance dehydration and PS-OCT measurements were recorded.

2.3.3 SWIR Dehydration Measurements

Each sample was placed in a mount connected to a high-speed XY-scanning motion controller system (Newport, Irvine, CA) ESP301 controller and 850G-HS stages, coupled with an air nozzle and a light source as described in (R. C. Lee et al., 2015). Each sample was immersed in the water bath for 30 seconds while being vigorously shaken to enhance water diffusion. After the

sample was removed from the water bath, an image was captured as an initial reference image and the air spray was activated. The air pressure was set to 15 psi and the computer-controlled air nozzle was positioned 5 cm away from the sample. Each measurement consisted of capturing a sequence of images at 4 frames per second for 60 seconds. The dehydration setup was completely automated using LabVIEW software (National Instruments, Austin, TX).

A Xeva-2.35-320 SWIR T2SL camera (Xenics, Leuven, Belgium) with response up to wavelength of 2.35 μm was used to acquire all the images during the dehydration process. Light from a 150 W fiber-optic illuminator FOI-1 (E Licht Company, Denver, CO) was directed at the sample at an incident angle of approximately 60° to reduce specular reflection and the source to sample distance was fixed at 5 cm. A FEL LP series long-pass filter at 1500 nm (Thorlabs, Newton, NJ) was used. SWIR reflectance images were processed and automatically analyzed using a dedicated program constructed with LabVIEW software. A region of interest (ROI) encompassing the whole sample was used and measurement was recorded for each time point. The intensity difference between the final and initial images, $\Delta I_{(t=60)}$, was calculated using $I_{60} - I_0$, where I_{60} is the mean intensity at $t = 60$ seconds and I_0 is the mean intensity prior to turning on the air nozzle.

2.3.4 Thermal Dehydration Measurements

An infrared (IR) thermography camera, Model A65 from FLIR Systems (Wilsonville, OR) sensitive from 7.5-13 μm with a resolution of 640 x 512 pixels, a thermal sensitivity of 50 mK, and a lens with a 13-mm focal length was used to record temperature changes during the dehydration process. Unlike SWIR dehydration measurements where a NIR light source is also needed to illuminate the tooth, thermal imaging does not require an additional light source. The ambient room temperature, flowing air temperature and water bath temperature were approximately 21°C (294.15 K) and were consistent throughout the experiment. The object emissivity was set to 0.92, and the atmospheric temperature was set to 294.15 K (Lin et al., 2009). While humidity values

were not recorded, every sample was measured under the same conditions, where the relative humidity was set at a default value of 50%. Previous studies have shown the area enclosed by the time-temperature curve, ΔQ , can be used as a quantitative measurement of porosity and can be used to discriminate between sound and demineralized enamel *in vitro* (Kaneko et al., 1999; R. C. Lee, Darling, & Fried, 2016b; Zakian et al., 2010). Thermal images were processed and analyzed using a dedicated program written in LabVIEW. Calibration was carried out via matching the measurements from the initial reference image to the ambient temperature. ΔQ was calculated and averaged among the samples.

2.3.5 Polarization-Sensitive Optical Coherence Tomography (PS-OCT)

An all-fiber-based optical coherence domain reflectometry (OCDR) system with polarization maintaining (PM) optical fiber, high-speed piezoelectric fiber-stretchers, and two balanced InGaAs receivers from Optiphase, Inc., Van Nuys, CA was used. This two-channel system was integrated with a broadband superluminescent diode (SLD) Denselight (Jessup, MD) and a high-speed XY-scanning system, ESP-300 controller and 850G-HS stages from Newport (Irvine, CA) for *in vitro* optical coherence tomography. This system is based on a polarization-sensitive Michelson white light interferometer. The high power (15 mW) polarized SLD source operated at a center wavelength of 1317 nm with a spectral bandwidth full-width-at-half-maximum (FWHM) of 84 nm. The sample arm was coupled to an AR-coated fiber-collimator to produce a collimated beam with a 6-mm diameter. The beam was focused onto the sample surface using a 20-mm focal length AR-coated planoconvex lens. This configuration provided lateral resolution of approximately 20- μm and an axial resolution of 10 μm in air with a signal to noise ratio of greater than 40–50 dB. The PS-OCT system is completely controlled using LabVIEW software. The system is described in greater detail in previous work (Hume, 1996)(Kaneko et al., 1999; R. C. Lee, Darling, Staninec, et al., 2016). Acquired scans are compiled into b-scan files. Image

processing was carried out using Igor Pro, data analysis software from Wavemetrics Inc. (Lake Oswego, OR).

We have developed automated methods for determining the lesion depth (LD), the integrated reflectivity over the lesions depth (ΔR), and the thickness of the transparent surface layer (TSL) (Chan et al., 2015). ΔR is calculated from the cross-polarization image and it is analogous to the integrated mineral loss with depth. The average LD, ΔR , and TSL values were calculated across all windows.

2.3.6 Data Analysis

Prism 7 (GraphPad Software Inc., La Jolla, CA) was used for regression.

2.4 Results and Discussion

2.4.1 SWIR Dehydration Measurements

SWIR reflectance dehydration measurements for the samples are shown in **Figure 2.2**. ΔI changes as the duration of remineralization increases and it was highly variable. The dehydration curves exhibited more variation in shape initially, but as remineralization duration increased, the sigmoidal characteristic of the curve stabilized. At 192 hours (8 days) of remineralization, permeability still did not return to baseline (thick black curve), suggesting that further remineralization might be necessary to fully remineralize using this model.

2.4.2 SWIR Dehydration Measurements

Thermal dehydration measurements for the samples are shown in **Figure 2.3**. ΔQ measured at each remineralization timepoint was normalized to ΔQ measured for sound control. ΔQ changes generally decreased as the duration of remineralization increased and it was also highly variable. The dehydration curves exhibited a sharper dip initially followed by drastic increase as dehydration continued for measurements at shorter remineralization duration. As remineralization

duration increased, the growth of the curve stabilized. At 192 hours (8 days) of remineralization, permeability not only returned to baseline (thick light green curve), the rate of change in temperature became fractions of that of sound control, suggesting that remineralization might have achieved dentin lesion arrest.

2.4.3 PS-OCT Measurements

Sample enamel PS-OCT B-scans are shown in **Figure 2.4**. As expected, the demineralized zone showed higher ΔR compared to the control zone. As remineralization duration increases, the difference in ΔR between the demineralized zone and the remineralized zone increases. Even though at 192 hours of remineralization the remineralized zone did not fully remineralize, the formation of a thin transparent surface zone was visibly apparent with PS-OCT.

Figure 2.5 shows the correlation between SWIR reflectance dehydration measurement and the thickness of the transparent surface layer measured by PS-OCT by samples. The plot presented a general negative trend of decreasing permeability, or decreasing ΔI , as the thickness of the transparent surface layer increases. The correlation was statistically significant ($r = -0.65$, $p < 0.05$) and negative. However, the variability of permeability was greater when the transparent surface layer was thinner compared to when the transparent layer was thicker. An explanation for this might be the inherent variation of the enamel structures such as enamel rod orientation, and the rate and location at which minerals are deposited. The remineralization model we have employed here may not penetrate the entire depth of the demineralized zone, as shown in **Figure 2.4**.

Figure 2.6 shows the correlation between thermal reflectance dehydration measurement and the thickness of the transparent surface layer measured by PS-OCT by samples. The plot presented a general negative trend of decreasing permeability, or decreasing ΔQ , as the thickness of the transparent surface layer increases. However, in this study, the correlation was not statistically significant ($r = -0.13$, $p > 0.05$) even though the relationship appears negative. The

variability of permeability was also greater when the transparent surface layer was thinner compared to when the transparent layer was thicker. An explanation for this might be that not all dentin lesions remineralized at the same rate, and that the dentinal tubules might be occluded even though mineral content was low, which may still lead to decrease in permeability.

2.5 Conclusions

In all, the results suggest that the permeability decreased with increasing transparent surface layer thickness. Furthermore, small increases in transparent surface layer thickness of <20 μm lead to large permeability changes for enamel lesions. The correlation between SWIR permeability and transparent surface layer thickness appears statistically significant and negative. The correlation between thermal permeability and TSL thickness appears negative but was not statistically significant. Future studies will be performed to determine the validity of permeability measurements as a method to assess lesion activity.

2.6 Figures and Figure Legends

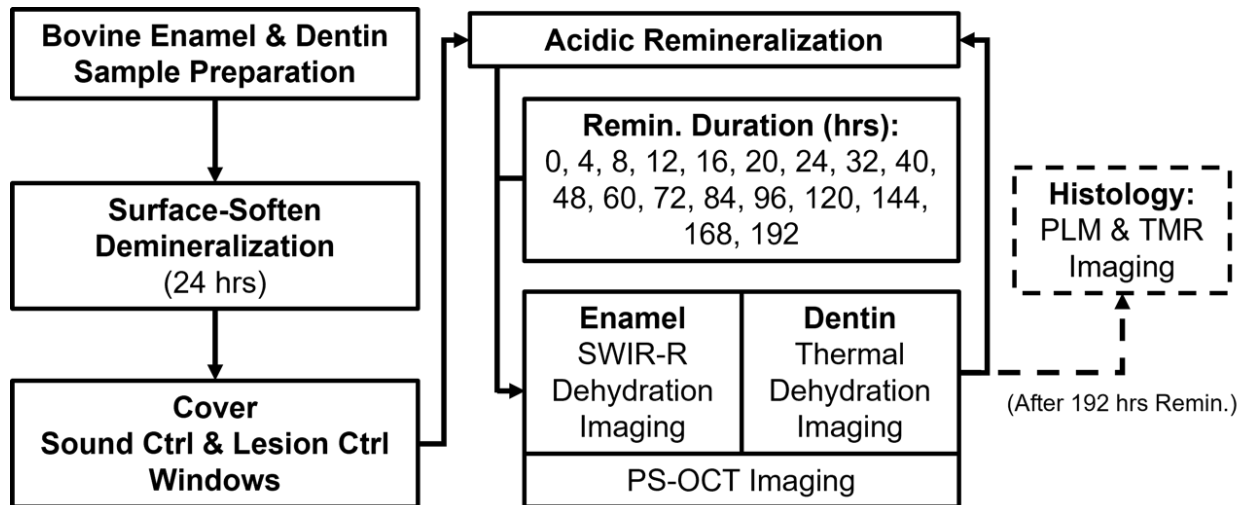


Figure 2.1 Workflow of the experimental setup

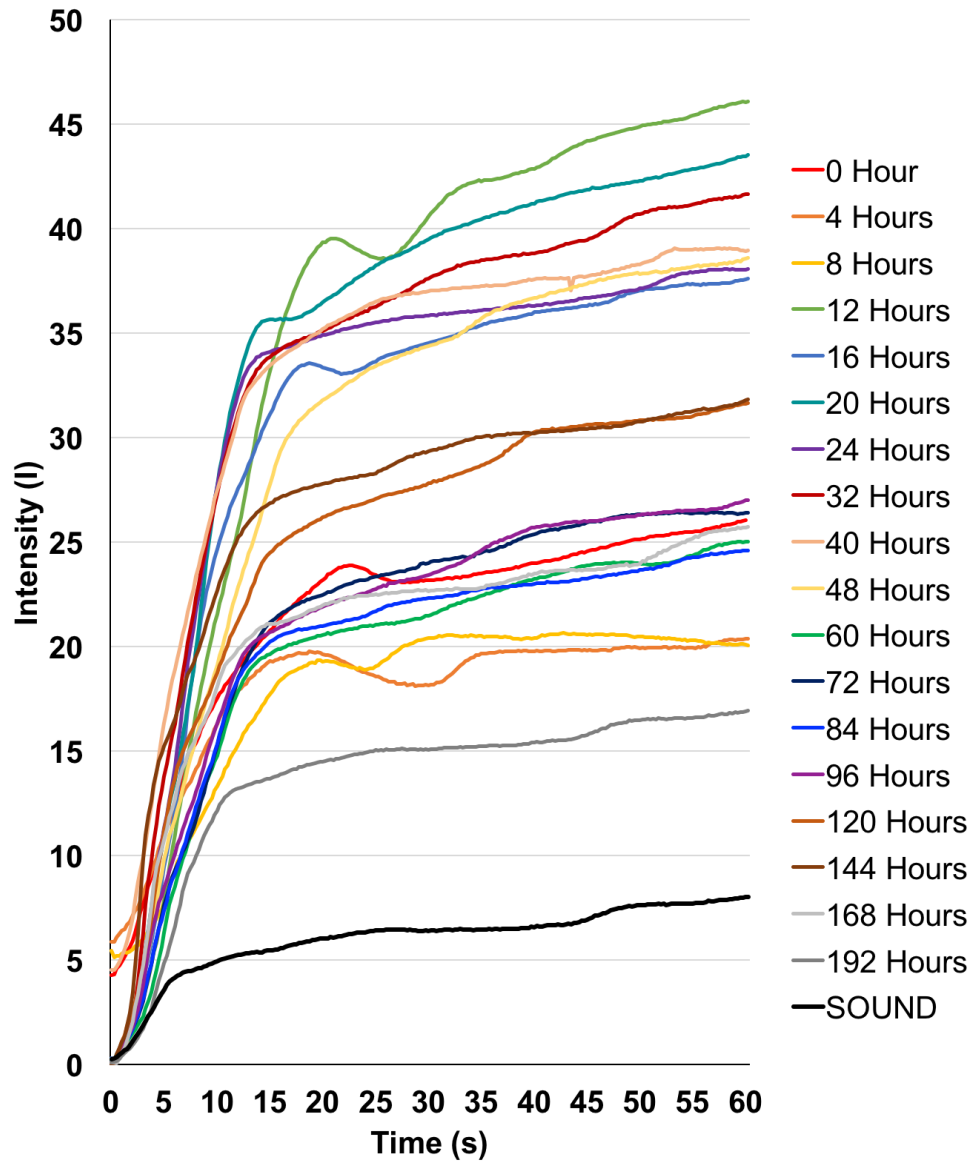


Figure 2.2 Average dehydration curves from 1500-1700 nm

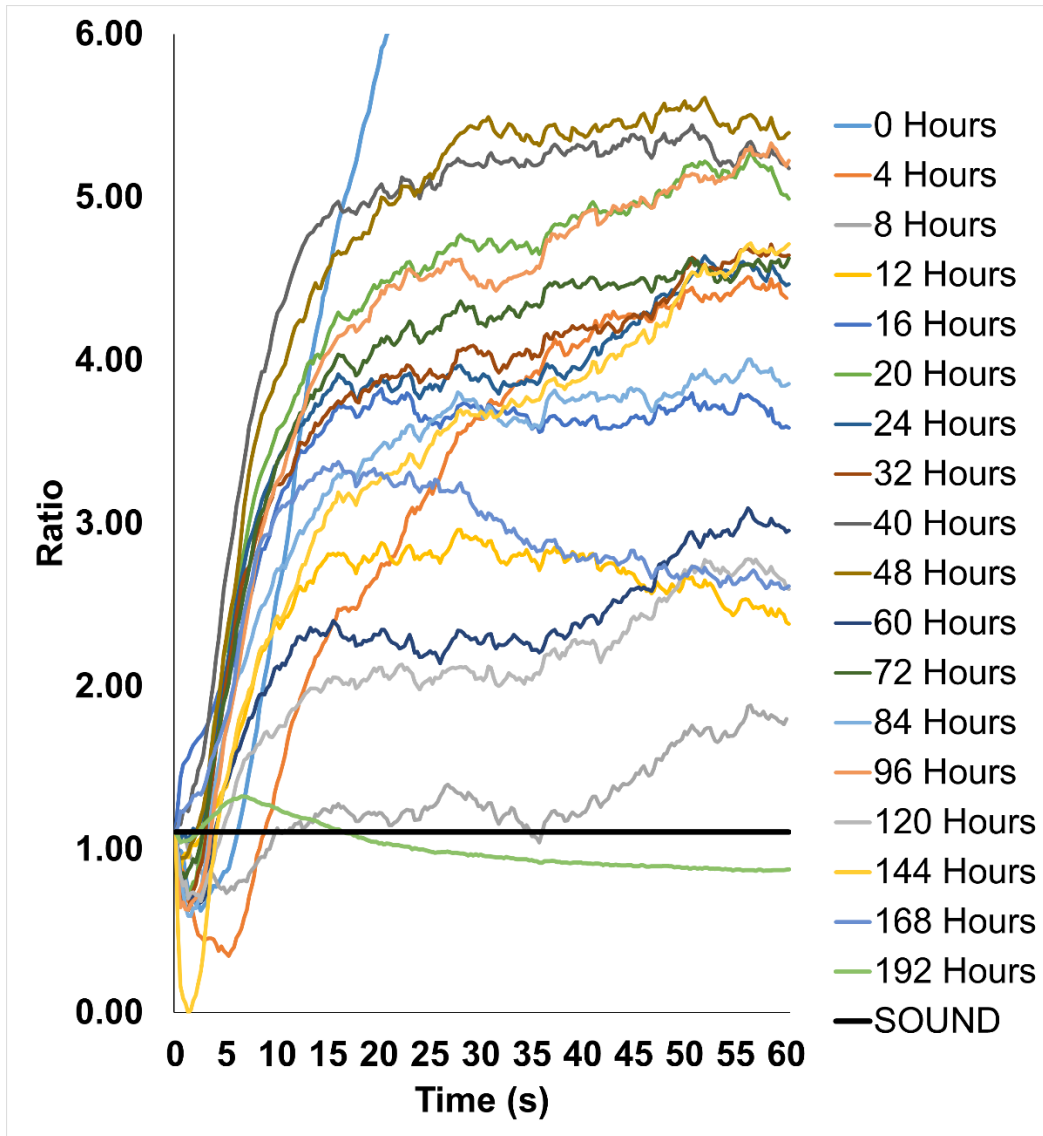


Figure 2.3 Average thermal dehydration curves

Dehydration curves from each remineralization timepoint was averaged and normalized to the rate of sound control. After demineralization, there are considerable increase in ΔQ , but decreased as remineralization duration increased. By 192 hours after remineralization, the lesion dehydration rate has stabilized (thick light green line).

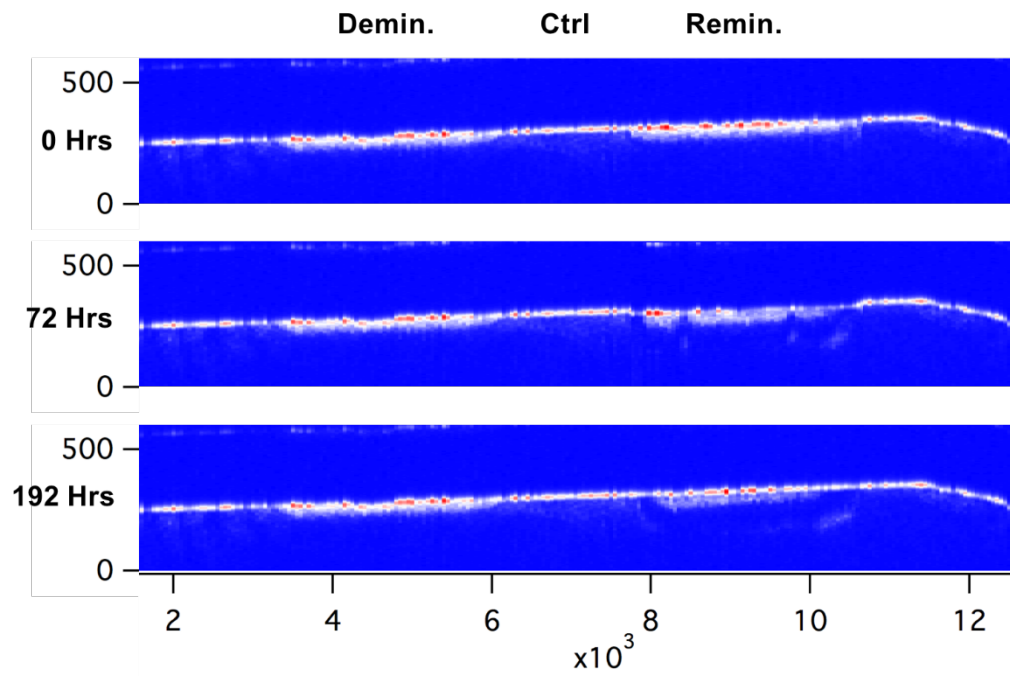


Figure 2.4 Sample PS-OCT B-scan of an enamel block

Images were taken at 0, 72, and 192 hours of remineralization followed by 24hrs of demineralization. Dimensions measured in microns (μm). Note the growth of the transparent surface layer in the remineralized zone.

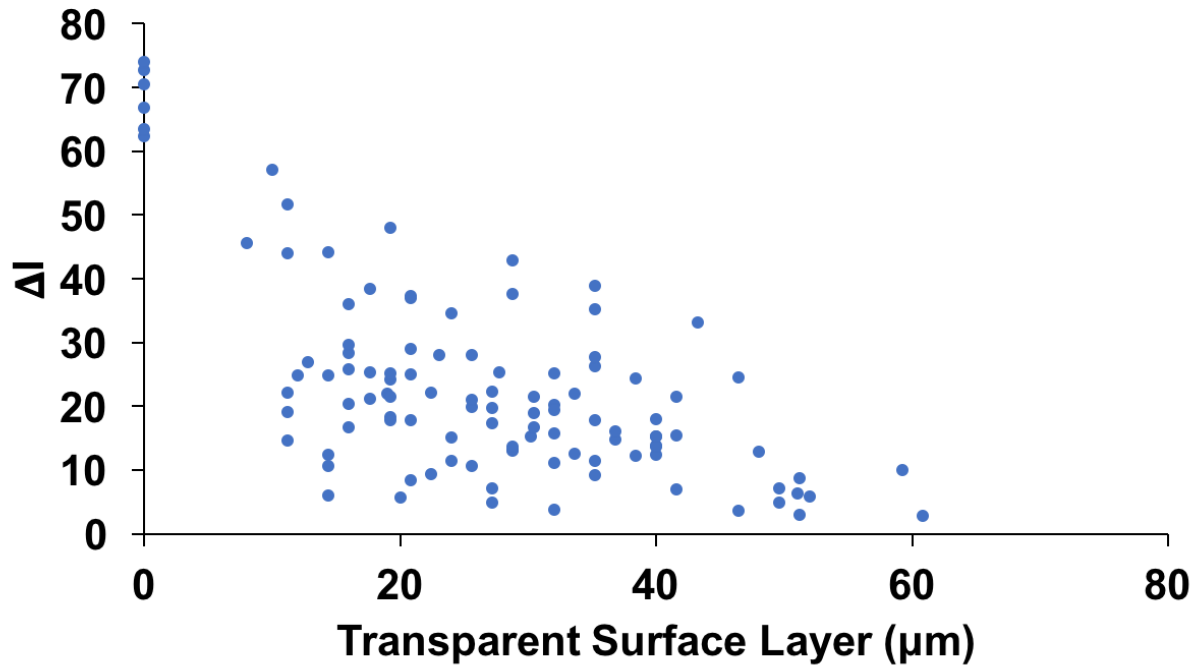


Figure 2.5 Correlation plot for enamel lesion permeability and TSL

Plot between SWIR reflectance permeability measurement and the thickness of the transparent surface layer measured by PS-OCT. The correlation was statistically significant ($r = -0.65$, $p < 0.05$). Each data point represents paired SWIR dehydration and PS-OCT measurements (if lesion TSL was present) for a sample regardless of remineralization timepoint.

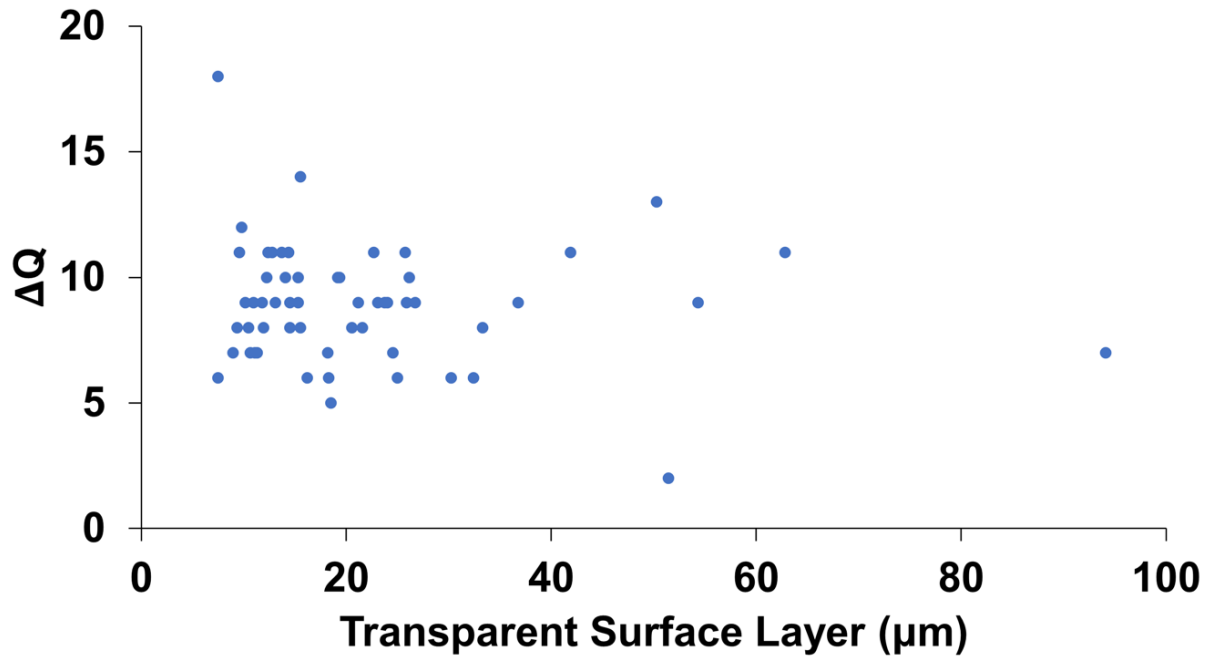


Figure 2.6 Correlation plot for dentin lesion permeability and TSL

Plot between thermal permeability measurement and the thickness of the transparent surface layer measured by PS-OCT. The correlation was not statistically significant ($r = -0.13$, $p > 0.05$), but the relationship does appear negative. Each data point represents paired thermal dehydration and PS-OCT measurements (if lesion TSL was present) for a sample regardless of remineralization timepoint.

CHAPTER III

USE OF SWIR DEHYDRATION AND OCT TO ASSESS THE COMPLETE ARREST OF SIMULATED INCIPIENT CARIES LESIONS

3.1 Summary

Previous studies have shown that optical coherence tomography (OCT) can be used to show the formation of a transparent surface zone on caries lesions indicative of remineralization. Studies have also shown that monitoring changes in the diffuse reflectivity of caries lesions during drying with air can be used to assess lesion activity and that the largest changes occur at SWIR wavelengths coincident with high water absorption at 1450 and 1950 nm. The purpose of this study was to determine when remineralization has occurred by monitoring changes in SWIR reflectance measurements and OCT images of simulated lesions over an extended period during exposure to a remineralization solution. Eight bovine enamel surfaces each with two treatment windows were exposed to a pH cycling regimen to produce simulated lesions 50-100 μm deep. OCT at 1310 nm was used to image the samples at each time point. An extended range tungsten halogen lamp with a 1450 nm band pass filter and a broadband amplified spontaneous emission source centered near the peak of the water-absorption band at 1950 nm were used as light sources. An extended range InGaAs camera (1000–2340 nm) was used to acquire reflected light images as the samples were dried with air. After 32 days of exposure to the remineralization solution, there were no further changes to the samples suggesting they had been completely arrested.

3.2 Introduction

Caries lesions can be arrested by the preferential deposition of mineral at the lesion surface that inhibits diffusion of fluids into the body of the porous lesion (Cate & Arends, 1977; ten Cate & Featherstone, 1991). Since arrested lesions do not need further treatment, the assessment of lesion activity is essential for appropriate clinical management. When lesions become arrested by mineral deposition or remineralization in the outer layers of the lesion, the diffusion of fluids into the lesion is inhibited. Hence, the rate of water diffusion out of the lesion reflects the degree of lesion activity. Previous studies have demonstrated that the optical changes due to the loss of

water from porous lesions can be exploited to assess lesion severity and activity with fluorescence, thermal, and SWIR imaging (Ando et al., 2017; Kaneko et al., 1999; R. C. Lee et al., 2015; R. C. Lee, Darling, Staninec, et al., 2016; R. C. Lee, Staninec, et al., 2016; Usenik et al., 2014; Zakian et al., 2010). Since arrested lesions are less permeable to water due to the highly mineralized surface layer, changes in the rate of water loss can be related to changes in lesion structure and porosity. We have investigated optical methods for assessing water diffusion rates from lesions since the porosity of the outer layers of active lesions is significantly greater than arrested lesions. This can be indirectly measured via SWIR reflectance methods (Chung et al., 2011; W. A. Fried et al., 2013; Simon et al., 2014). Normal enamel is transparent at SWIR wavelengths, whereas early demineralization causes increased SWIR reflectance due to scattering by pores formed in the enamel. Water in the pores at the surface of the lesion absorbs the incident SWIR light, particularly at wavelengths of 1450 and 1950 nm that are coincident with water absorption bands, reducing surface scattering and lesion contrast. Loss of that water during dehydration produces a marked increase in reflectivity and lesion contrast. *In vivo* studies have been published utilizing the fluorescence loss of white spot lesions on coronal surfaces (Ando et al., 2017) and thermal imaging to assess root caries during dehydration (V. Yang et al., 2020).

Recent studies at wavelengths beyond 1700 nm show that the contrast of demineralization on tooth surfaces continues to increase with increasing wavelength due to decreasing scattering in sound enamel and increasing water absorption (Chan & Fried, 2018; W. A. Fried et al., 2021; Ng et al., 2019). Contrast is particularly high near the strong water absorption band at 1950 nm. Last year we showed that 1950 nm is ideal for SWIR reflectance dehydration measurements (J. Tressel et al., 2021; J. T. Tressel et al., 2021).

Previous studies have shown that OCT and polarization sensitive OCT are able to show the formation of the zone of increased mineral density that forms after remineralization both *in vivo* and *in vitro* (Jones et al., 2006; Kang et al., 2012; Manesh et al., 2009a). We have demonstrated in several studies that the lesion severity can be represented by the integrated

reflectivity with depth in OCT images (Chong et al., 2007; D. Fried et al., 2002; Jones et al., 2006; Jones & Fried, 2006; C. Lee et al., 2009; Manesh et al., 2009a; Ngaotheppitak et al., 2005). The integrated reflectivity, ΔR , obtained from OCT is a measurement analogous to the integrated mineral loss, ΔZ , obtained from transverse microradiography (Arends et al., 1997). OCT measurements can be used to describe the lesion severity using measurements of the lesion depth, ΔR and the transparent surface layer thickness (TSL). SWIR and OCT measurements have shown that the relationship between the surface zone thickness and lesion permeability is highly non-linear. A small increase in the surface layer thickness can lead to a marked decrease in permeability (N.-Y. N. Chang et al., 2018). The purpose of this study was to monitor simulated lesions on bovine enamel during remineralization using SWIR dehydration measurements at 1450 and 1950 nm and OCT imaging at 1310 nm and establish when remineralization is complete.

3.3 Materials and Methods

3.3.1 Sample Preparation

Enamel blocks ($n = 8$), approximately 10-12 mm in length with a width of 2 mm and a thickness of 2 mm, were prepared from extracted bovine incisors acquired from a slaughterhouse. Five windows were produced by making small incisions between each window using a CO₂ laser. The 1st, 3rd and 5th windows of the blocks were covered with a thin layer of acid-resistant varnish in the form of nail polish. The varnish was also applied to all sides except the non-control top surfaces of the enamel blocks before exposure to the demineralization solution. A pH cycling model was used for 6 days to create lesions on two exposed windows on each block. The central window was covered with acid resistant varnish. pH cycling involved exposing the samples to the demineralizing solution which was maintained at 37°C and pH 4.3, composed of 2.0 mmol/L calcium, 2.0 mmol/L phosphate, and 75 mmol/L acetate, for 6 h each day of the treatment followed by immersion overnight for 17 hours in a remineralizing solution of 1.5 mmol/L calcium, 0.9 mmol/L phosphate, 150 mmol/L KCl, 20 mmol/L HEPES buffer maintained at pH 7.0 and 37 °C. For

remineralization, from day 6 to day 32 the samples were immersed in the same remineralization solution described above with 2 ppm fluoride added to enhance remineralization. The demineralization solution was changed every 3 days and the remineralization solution every 12 days.

3.3.2 Visible/Color Images

A USB microscope, Model 5MP Edge AM7915MZT, AnMO Electronics Corp. (New Taipei City, Taiwan) equipped with a visible polarizer was used to acquire visible images of all samples. The digital microscope captures 5-megapixel (2952 x 1944) color images. Eight white LED lights contained in the camera illuminate the sample and a single polarization element is utilized to reduce glare.

3.3.3 Optical Coherence Tomography

An IVS-2000-HR-C OCT system from Santec (Komaki, Aichi, Japan) was used for this study. This system utilizes a swept laser source and a handpiece with a microelectromechanical (MEMS) scanning mirror and the imaging optics. It can acquire complete tomographic images of a volume of 5 x 5 x 5 mm in approximately 3 seconds. The body of the handpiece is 7 x 18 cm with an imaging tip that is 4 cm long and 1.5 cm across. This system operates at a wavelength of 1312 nm with a bandwidth of 173 nm with a measured resolution in air of 8.8 μm (3 dB). Measured lesion depths were divided by 1.6, the refractive index of enamel. The lateral resolution is 30 μm ($1/e^2$) with a measured imaging depth of 5 mm in air. Image analysis and lesion structural measurements were carried out using Dragonfly from ORS (Montreal, Canada). The lesion depth and the integrated reflectivity over the lesion depth (ΔR) and transparent surface layer thickness (TSL) were also calculated using an automated analysis program written in MATLAB from MathWorks (Natick, MA) (N.-Y. N. Chang et al., 2018).

3.3.4 SWIR Dehydration Measurements

Samples were stored in a moist environment to preserve internal hydration and the samples were immersed in a water bath before mounting and performing measurements. A computer-controlled air nozzle with a 1 mm aperture and an air pressure set to 25 psi was positioned 5 cm away at a 20° angle.

After each sample was removed from the water bath, an image was captured as an initial reference image and the pressurized air nozzle was activated to dehydrate the sample. Each measurement consisted of capturing a sequence of images at 25 frames per second for 60 seconds. For each measurement, the air nozzle and the light source were centered on the region of interest (ROI) that encompasses the entire sample. The dehydration setup was completely automated using LabVIEW software (National Instruments, Austin, TX).

A Xenics (Leuven, Belgium) Model Xeva-2.35-320 extended range InGaAs camera sensitive from 900-2350 nm (320 x 240 pixel) was used to acquire the SWIR images. The camera was equipped with a Navitar (f = 35 mm) SWIR optimized (f/1.4) lens and a 60 mm achromat lens was positioned 40 mm from the 35 mm lens. A high extinction polarizer was used to acquire cross polarization images. The quantum efficiency peaks at 1500 nm near 65% and drops off rapidly to 30% after 1700 nm and drops off again to below 20% after 2000 nm. A Model SLS202 extended wavelength tungsten-halogen light source from Thorlabs (Newton, NJ) with a 1460 nm (85) bandpass filter, collimating optics and a high extinction polarizer was used. A polarized, broadband amplified spontaneous emission (ASE) light source Model AP-ASE-2000 from AdValue Photonics (Tucson, AZ) with a center wavelength of 1959 nm and a bandwidth of ~100 nm (-3 dB), 230 nm (-30 dB) and an output power of 11 mW was used for the 1950 nm light source. The light sources were placed at 20° angles to the camera but positioned on the same side. Images were processed and automatically analyzed using a dedicated program constructed with LabVIEW software. ΔI was measured by subtracting the intensity at time 0 from the intensity after

60 seconds of drying, $I_{60} - I_0$. I_{AUC} was calculated by integrating the area under the intensity versus time curves.

3.4 Results and Discussion

OCT b-scan images of one of the samples at 6, 12, 18 and 32 days is shown in **Figure 3.1**. The intensity of the reflectivity is shown in grayscale with high reflectivity in white and weak reflectivity in black. At 6 days the left and right windows show the two lesions that are formed with the reflectivity of the sound window shown in the center. The left and central windows were covered in acid resistant varnish from day 6 to day 32 and they were not exposed to the remineralization solution. The right window was exposed to the remineralization solution and changes are clearly visible. At day 32 a clear transparent zone at the top of the lesion is visible due to mineral deposition near the surface. The lesion depth and the integrated reflectivity over the lesion depth were monitored for 32 days and the values are plotted in **Figure 3.2**. Both values increased from day 0 to 6 as the lesion was formed. There was a slight decrease from day 6 to day 32 for the integrated reflectivity due to remineralization. The lesion depth did not decrease significantly over time. This has been observed before in remineralization experiments since the mineral is deposited from the outside surface first until it blocks all the pores near the lesion surface and arrests the lesion. The mean \pm standard deviation (SD) of all the parameters measured using OCT and SWIR dehydration are tabulated in **Table 3.1**.

The means \pm standard errors of the mean (SEM) are plotted in **Figure 3.3** for the period of remineralization from day 6 to day 32 for four of the lesion parameters that showed significant change: the integrated reflectivity ΔR ; the change in SWIR intensity after drying for 60 seconds; ΔI , the area under the intensity vs drying time curve; I_{AUC} and the transparent surface layer thickness, TSL. ΔR , ΔI , and I_{AUC} all show a significant decrease ($p < 0.05$) over time, while the TSL shows a significant increase over time. Linear regression indicated that changes in the parameters correlated with time, ΔR ($r^2 = 0.50$), ΔI ($r^2 = 0.64$), I_{AUC} ($r^2 = 0.55$) and TSL ($r^2 = 0.14$).

Both SWIR wavelengths 1460 and 1950 nm used for dehydration measurements showed significant decreases in ΔI and I_{AUC} over the remineralization period. It is difficult to determine at what time there were no further changes in the measurements. The TSL surface appeared to form in the first 5-15 days and there was no further change after that time. The greatest changes in ΔI and I_{AUC} occurred in the first 18 days and the greatest changes in ΔR was in the first 12 days. The approach of calculating I_{AUC} appeared to provide similar results to calculating ΔI . It is interesting to compare these results with one of our previous studies in which the dependence of the lesion dehydration rate with the lesion transparent surface layer thickness was measured (N.-Y. N. Chang et al., 2018). In that study ΔI was measured for transparent surface layer thicknesses that varied from 10-60 μm . In that study even the existence of a thin TSL caused a large drop in ΔI . Changes in the SWIR measurements were greater than the changes in ΔR suggesting that SWIR dehydration measurements are more sensitive to lesion remineralization.

3.5 Conclusions

SWIR permeability measurements and OCT imaging of simulated lesions subjected to different days of remineralization were compared. The greatest changes to permeability were seen after 18 days of remineralization, and the greatest changes to integrated reflectivity occurred after 12 days. No further changes to the simulated enamel lesions were seen by SWIR permeability measurement and OCT imaging after 32 days of exposure to the remineralization solution. Changes in OCT ΔR were less than the changes seen by SWIR measurements, suggesting that SWIR permeability measurements are more sensitive to lesion remineralization.

3.6 Figures and Figure Legends



Figure 3.1 OCT b-scans of a sample taken after 6, 12, 18, and 32 days.

Post-remineralization OCT images at various days. *Top:* Day 6 scan shows the sound window in the center and the two lesion windows on each side. The left lesion window and the central sound window were covered with acid-resistant varnish during remineralization (Day 6 to 32).

Table 3.1 SWIR permeability and OCT measurements throughout remineralization
Mean \pm SD for each day of exposure to the remineralization solution.

<u>Days</u>	<u>SWIR 1460 nm</u>		<u>SWIR 1950 nm</u>		<u>OCT</u>		
	<u>ΔI (au)</u>	<u>I_{AUC} (au)$\times 10^4$</u>	<u>ΔI (au)</u>	<u>I_{AUC} (au)$\times 10^4$</u>	<u>LD (μm)</u>	<u>ΔR (au)</u>	<u>TSL (μm)</u>
6	234 \pm 38	42.1 \pm 8.4	338 \pm 135	57.8 \pm 25	131 \pm 15	893 \pm 149	0 \pm 0
9	217 \pm 60	33.8 \pm 9.7	327 \pm 145	50.4 \pm 23	125 \pm 10	779 \pm 134	7 \pm 10
12	180 \pm 50	23.5 \pm 10	275 \pm 124	30.4 \pm 21	115 \pm 18	668 \pm 79	4 \pm 9
15	205 \pm 54	26.0 \pm 8.4	363 \pm 113	45.1 \pm 6.4	122 \pm 7	712 \pm 66	16 \pm 11
18	115 \pm 37	15.7 \pm 6.1	244 \pm 103	31.0 \pm 18	118 \pm 9	762 \pm 109	10 \pm 11
22	114 \pm 28	15.5 \pm 4.3	251 \pm 81	33.6 \pm 13	124 \pm 15	683 \pm 81	10 \pm 14
26	101 \pm 32	15.2 \pm 6.2	249 \pm 96	35.0 \pm 13	120 \pm 11	671 \pm 68	6 \pm 12
32	103 \pm 34	14.8 \pm 4.3	210 \pm 117	28.9 \pm 19	111 \pm 14	673 \pm 98	9 \pm 13

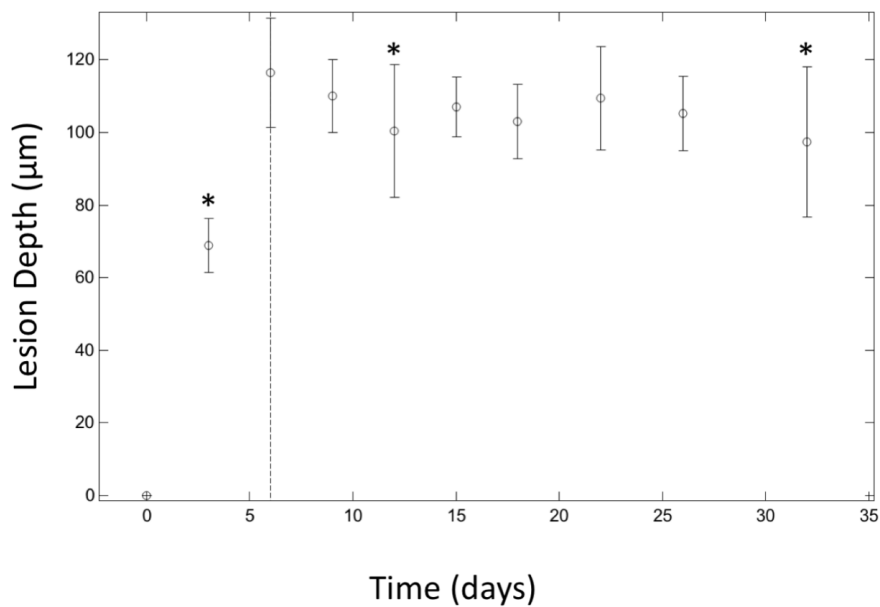
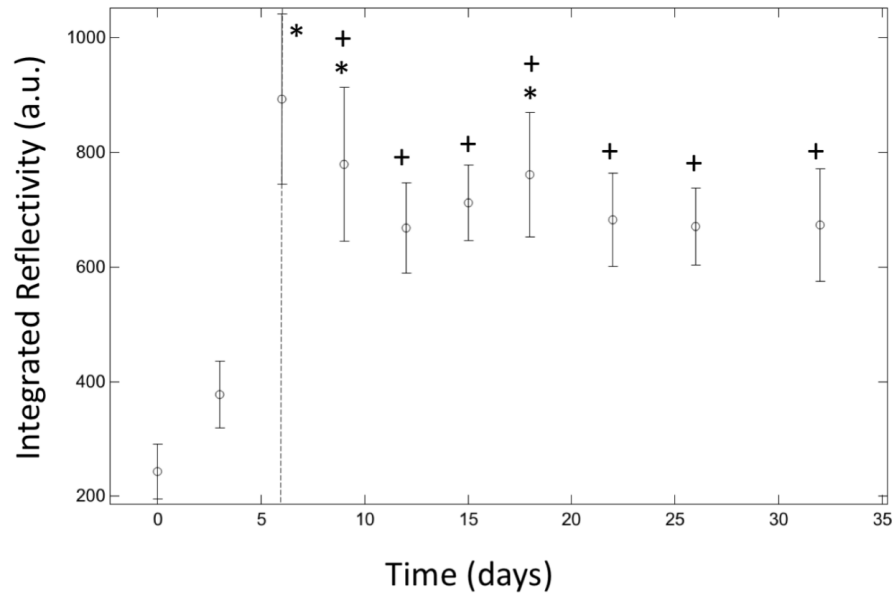


Figure 3.2 Plots of integrated reflectivity and lesion depth over remineralization duration
 Plot for remineralization Days 0 through 32. Demineralization occurred from Day 0 to 6 and remineralization was from Day 6 to 32. Time points with the same symbol are statistically similar ($p > 0.05$) via comparison with repeated measures ANOVA.

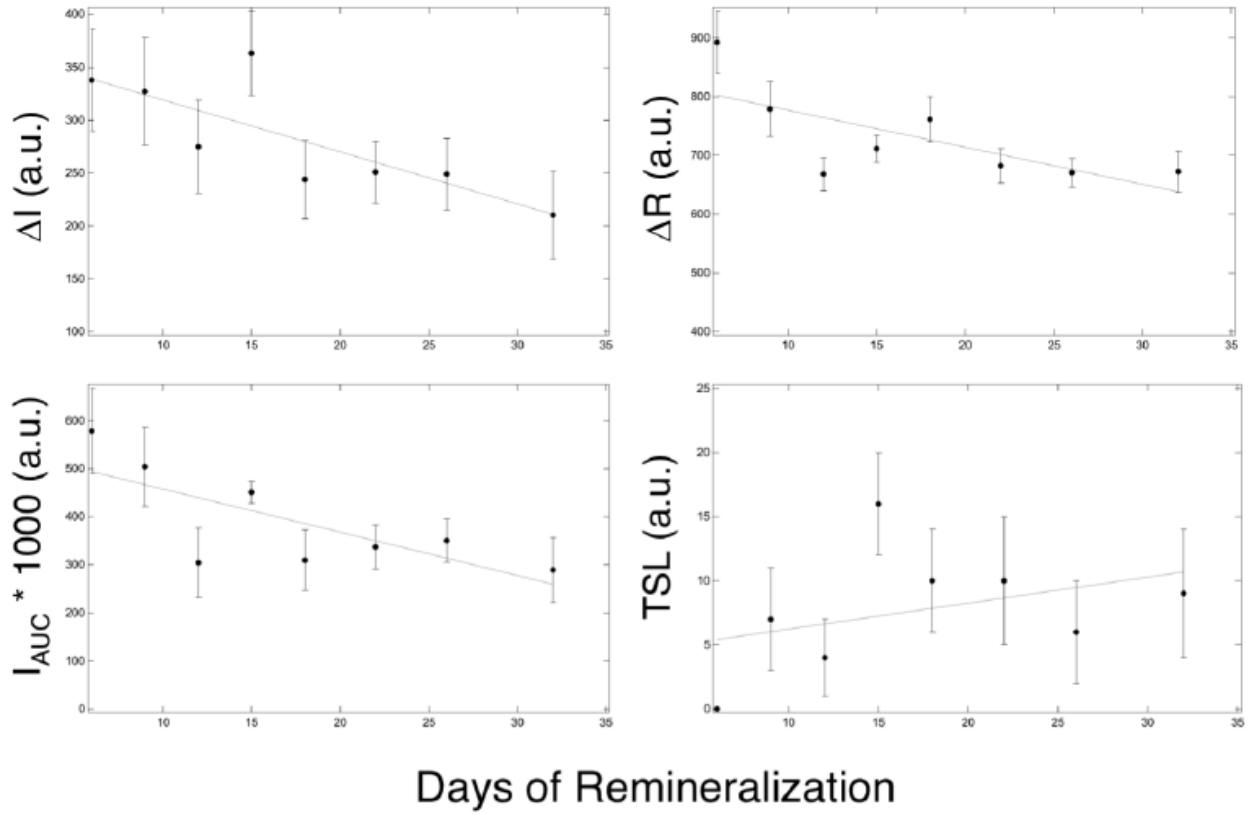


Figure 3.3 Plots of ΔR , TSL, and ΔI and I_{AUC} at 1950 nm throughout remineralization
 The mean \pm SD plotted from remineralization Day 6 to 32. Best-fit linear regression lines are shown.

CHAPTER IV

THE RELATIONSHIP OF DEHYDRATION RATE AND TRANSPARENT SURFACE LAYER THICKNESS FOR CORONAL LESIONS ON EXTRACTED TEETH

4.1 Summary

Transparent remineralized surface zones found on natural caries lesions may reduce the permeability to water and plaque generated acids. SWIR reflectance imaging coupled with dehydration can be used to measure changes in the fluid permeability of lesions in enamel and dentin. Previous work demonstrated a negative association between the surface zone thickness and the rate of dehydration in simulated enamel lesions. In this study, the rates of dehydration and thickness of transparent surface layer of coronal lesions of extracted teeth were measured and correlated. Reflectance imaging at SWIR wavelengths from 1695-1750 nm, which coincides with higher water absorption and manifests the greatest sensitivity to contrast changes during dehydration measurements, was used to image these enamel lesions. The remineralized surface layer thickness was determined using optical coherence tomography (OCT). SWIR permeability measurements were correlated with transparent surface layer thickness by OCT imaging. The results indicate that a small increase in transparent surface layer thickness of $<50 \mu\text{m}$ lead to large permeability changes.

4.2 Introduction

The majority of newly discovered carious lesions are frequently localized to the occlusal pits and fissures of the posterior dentition and the proximal contact sites between teeth, where they are often more difficult to detect. Clinicians mostly rely on tactile and visual examination to determine whether dental decay is active or arrested (Fejerskov & Kidd, 2003). If the lesion appears smooth, hard, and dark, it is assumed that it is arrested (Pitts, 2009). However, this method is subjective and unreliable (Fejerskov & Kidd, 2003; Pitts, 2009). The challenge lies in that many lesions might be arrested or do not require intervention, and that active lesions are difficult to identify with current diagnostic methods. Accurate assessment of lesion activity, depth, and severity is important to determine whether intervention is necessary. Effective utilization of new optical diagnostic technologies taking advantages of the changes in the light scattering of the lesion have

great potential for diagnosing the present state of the lesions. Therefore, the development of new methods, such as SWIR reflectance dehydration imaging, are needed for the clinical assessment of lesion activity and to avoid unnecessary cavity preparations.

When lesions become arrested due to remineralization in the outer layers of the lesion, the diffusion of fluids into the lesion is inhibited. Hence, the rate of water diffusion out of the lesion reflects the degree of lesion activity. Previous studies have demonstrated that the optical changes due to the loss of water from porous lesions can be used to assess lesion severity and activity with QLF, thermal, and SWIR imaging (Ando et al., 2017; Kaneko et al., 1999; R. C. Lee, Darling, Staninec, et al., 2016; R. C. Lee et al., 2015; R. C. Lee, Staninec, et al., 2016; Usenik et al., 2014; Zakian et al., 2010). Conversely, arrested lesions and developmental defects (fluorosis) often possess a highly mineralized surface layer, where the rate of water loss is less due to related changes in lesion structure and porosity. We have investigated the use of SWIR reflectance methods to indirectly assess water diffusion rates from lesions since the porosity of the outer layers of active lesions is significantly greater than arrested lesions (Chung et al., 2011; W. A. Fried et al., 2013; Simon et al., 2014). Normal enamel is transparent in SWIR wavelengths, whereas early demineralization causes increased SWIR reflectance due to scattering. Water in the pores at the surface of the lesion absorbs the incident SWIR light, particularly at wavelengths such as 1450 nm and beyond, reducing surface scattering and lesion contrast. Loss of that water during dehydration produces a marked increase in reflectivity and lesion contrast.

New technologies are also needed to determine whether lesions are active and expanding, partially arrested and undergoing remineralization, or fully arrested and remineralized in clinical settings. Optical Coherence Tomography (OCT) may be capable of this task. Previous works have demonstrated that arrested lesions exhibit a well-defined surface zone of reduced reflectivity that can be clearly resolved in OCT images (Jones et al., 2006; Jones & Fried, 2006; Kang et al., 2012). OCT provides high speed and high-resolution measurements of the reflectivity from each

layer of the lesion and is able to detect the formation of a zone with increased mineral density and reduced light scattering due to remineralization.

The purpose of this study is to continue our previous work in developing a method to assess lesion activity by assessing lesion activity of lesions on extracted human premolar and molars (*ex vivo*) (N.-Y. N. Chang et al., 2018). We hypothesize that the thickness of the highly mineralized transparent surface zone formed during remineralization correlates with the lesion permeability and activity in human enamel. We correlated the results from SWIR reflectance dehydration measurements and OCT measurements and found that minor changes in surface layer thickness may lead to major changes in fluid permeability in remineralized enamel lesions.

4.3 Materials and Methods

4.3.1 Extracted Tooth Samples

Fifty extracted human premolar and molars with coronal lesions determined by a clinician were obtained. The teeth were sterilized with gamma radiation and stored in 0.1% thymol. **Figure 4.1** shows the workflow of the study design employed.

4.3.2 Short-Wave Infrared (SWIR) Dehydration Measurements

Each sample was placed in a mount connected to a high-speed XY-scanning motion controller system (Newport, Irvine, CA) ESP301 controller and 850G-HS stages, coupled with an air nozzle and a light source as previously described (R. C. Lee et al., 2015). Each sample was immersed in the water bath for 30 seconds while being shaken to enhance water diffusion. After the sample was removed from the water bath, an image was captured as an initial reference image and the air spray was activated. The air pressure was set to 30 psi and the computer-controlled air nozzle was positioned 5 cm away from the sample. Each measurement consisted of capturing a sequence of images at 4 frames per second for 60 seconds. The dehydration setup was completely automated using LabVIEW software (National Instruments, Austin, TX).

A Model SU320KTSX InGaAs focal plane array (Sensor-Unlimited, Princeton, NJ) with a spectral sensitivity range from 900 to 1750 nm, a resolution of 320 x 256 pixels, and an InfiniMite lens (Infinity, Boulder, CO) was used to acquire all the images during the dehydration process. Light from a 150 W fiber-optic illuminator FOI- 1 (E Licht Company, Denver, CO) was directed at the sample at an incident angle of approximately 30° from surface normal of the tooth occlusal surface to reduce specular reflection and the source to sample distance was fixed at 5 cm. A FEL LP series long-pass filter at 1695 nm (Thorlabs, Newton, NJ) was used. SWIR reflectance images were processed and automatically analyzed using a dedicated program constructed with LabVIEW software. A region of interest (ROI) encompassing the whole sample was used. The intensity difference between the final and initial images, $\Delta I_{(t=60)}$, was calculated using $I_{60} - I_0$, where I_{60} is the mean intensity at $t = 60$ seconds and I_0 is the mean intensity prior to turning on the air nozzle. Prism 7 (GraphPad Software Inc., La Jolla, CA) was used for regression analysis.

4.3.3 Optical Coherence Tomography (OCT)

A prototype polarization diversity-detection OCT system (Axsun Technologies, Billerica, MA) with an integrated dental handpiece capable of acquiring high speed 3D scans of the occlusal surface of an entire tooth (8(X) x 8(Y) x 7(Z) mm) was used for this study. The system utilized an Axsun Technologies swept source engine operating at a 100 kHz scan rate and a MEMS scanner for 3D scans. The Axsun engine, fiber interferometer and polarization diversity setup, and MEMS controller were packaged in a console 250 by 300 by 150 mm. The host computer used was an Intel NUC miniPC based on a dual-core i3-7100U 2.4GHz processor with 8GB RAM. B-scan images were acquired at over 100 fps with 66 μ m transverse and 7 μ m depth resolution. Zuluaga et al. provided more detail regarding this system (Zuluaga et al., 2019).

4.4 Results and Discussions

4.4.1 SWIR Dehydration Measurements

SWIR reflectance dehydration measurements for the samples are shown in **Figure 4.2**. Results were analyzed by clinical decisions (clinically active or clinically arrested, denoted as ΔI_{Active} and $\Delta I_{\text{Arrested}}$, respectively) and by the thickness of TSL (denoted as $\Delta I_{\text{TSL}<50}$, $\Delta I_{\text{TSL}<75}$, $\Delta I_{\text{TSL}<120}$). In general, the dehydration curves exhibited a sharp positive slope within 10 seconds of dehydration with the exception of samples having TSL thickness of $< 50 \mu\text{m}$, which exhibited slower increase but higher final intensity values. Quantitatively, in the clinical decision analysis, $\Delta I_{\text{Active}} = 19.76 \pm 2.40$ (mean \pm SD), which is marginally higher than $\Delta I_{\text{Arrested}} = 19.37 \pm 1.43$, or effectively no difference ($t = 0.51$; $p > 0.05$). When the dehydration rate (ΔI) was analyzed based on the thickness of TSL, the result is $\Delta I_{\text{TSL}<50} = 26.88 \pm 10.48$, $\Delta I_{\text{TSL}<75} = 18.12 \pm 7.76$, $\Delta I_{\text{TSL}<120} = 15.13 \pm 4.29$ with significant differences amongst groups (1-way ANOVA: $F = 8.49$; $p < 0.05$), with the exception of TSL $<75 \mu\text{m}$ and TSL $<120 \mu\text{m}$ groups (Tukey's MCT mean diff. = 2.96, $p > 0.05$). These results suggest a negative correlation between dehydration rate and transparent surface layer thickness.

4.4.2 OCT Measurements

Sample OCT B-scans are shown in **Figure 4.3**. As expected, samples with active lesions determined by dehydration rate measurement showed higher reflectivity on the lesion surface with no visible formation of a surface zone. Samples with arrested lesions have a visible transparent surface zone of varying thickness. **Figure 4.4** shows the correlation between SWIR reflectance dehydration measurement and TSL thickness measured by OCT. The plot shows a negative trend of decreasing permeability, or decreasing ΔI , as the thickness of the transparent surface layer increases. However, the variability of permeability was greater when the transparent surface layer was thinner compared to when the transparent layer was thicker. An explanation for

this might be the inherent variation of the enamel structures such as enamel rod orientation, the rate and location at which minerals are deposited, and the remineralization environment prior to extraction. In all, the results suggest that the permeability decreased with increasing transparent surface layer thickness. Furthermore, small increases in transparent surface layer thickness of <math><50\ \mu\text{m}</math> lead to large permeability changes. The teeth will be sectioned and examined with polarized light microscopy (PLM) or examined intact with μCT to confirm the presence of a highly mineralized surface zone. Additional studies will be aimed to assess the feasibility for integrating SWIR-R dehydration and OCT as a diagnostic tool to aid clinician in determining lesion activity.

4.5 Conclusions

The highly mineralized transparent surface layer plays an integral role in identifying an arrested lesion. SWIR reflectance permeability measurement of surface lesions of extracted teeth appears to negatively correlate with the thickness of the transparent surface layer determined by OCT imaging. The results indicate that at thickness of $>50\ \mu\text{m}$, the permeability of the lesion does not result in a decreased intensity as much and is significantly lower than lesions with transparent surface layer thinner than $50\ \mu\text{m}$. Permeability seems to no longer change when transparent layer thickness is $>75\ \mu\text{m}$. This further provides evidence that SWIR reflectance permeability measurement may be an effective clinical method for assessing surface lesion activity.

4.6 Figures and Figure Legends

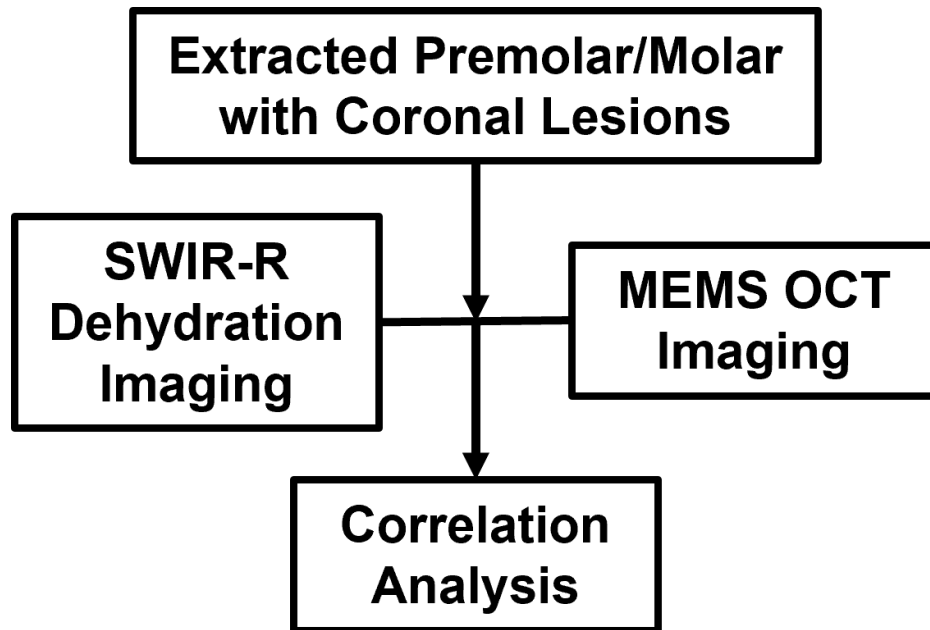


Figure 4.1 Workflow of the experimental setup

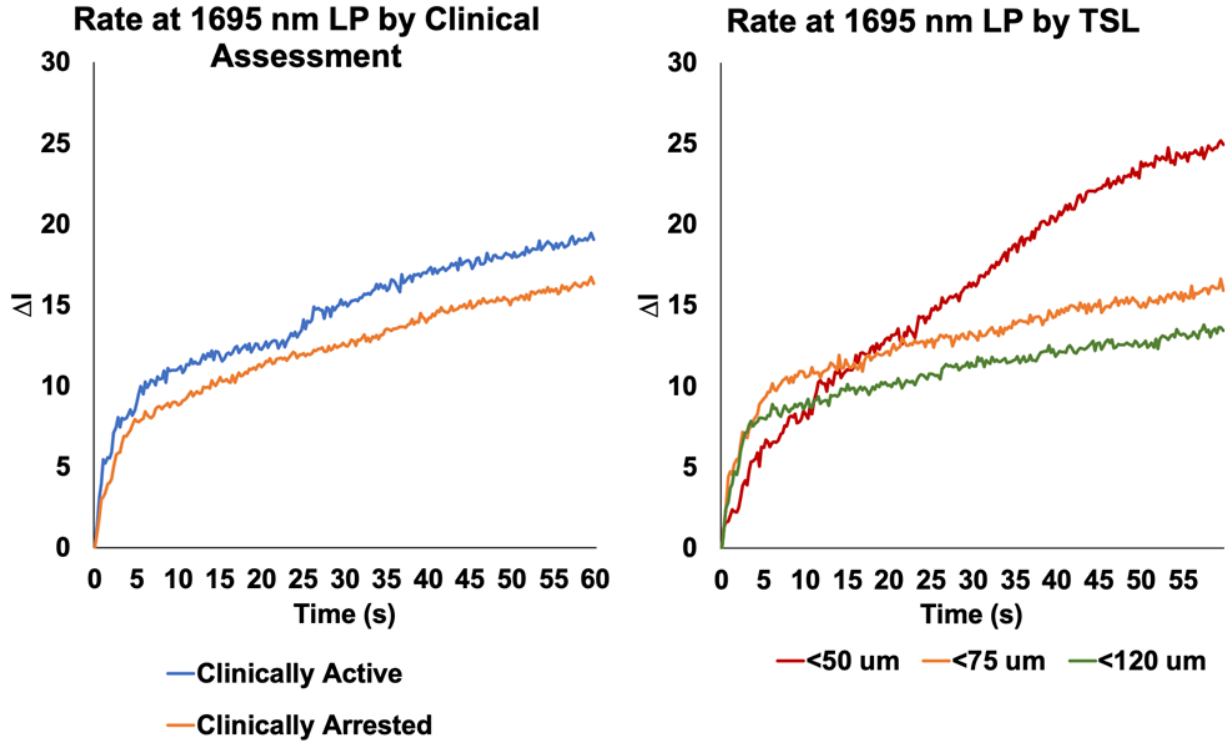


Figure 4.2 Average permeability curves from 1695-nm LP

Left: Permeability curves compared on the basis of clinical assessment ($\Delta I_{\text{Active}} = 19.76$, ($\Delta I_{\text{Arrested}} = 19.37$; $t = 0.51$; $p > 0.05$). *Right:* Permeability curves compared based on presence of a transparent surface layer (TSL) thickness of <50, <75, and <120 μm ($\Delta I_{\text{TSL}<50} = 26.88$, $\Delta I_{\text{TSL}<75} = 18.12$, $\Delta I_{\text{TSL}<120} = 15.13$; 1-ANOVA, $p < 0.05$).

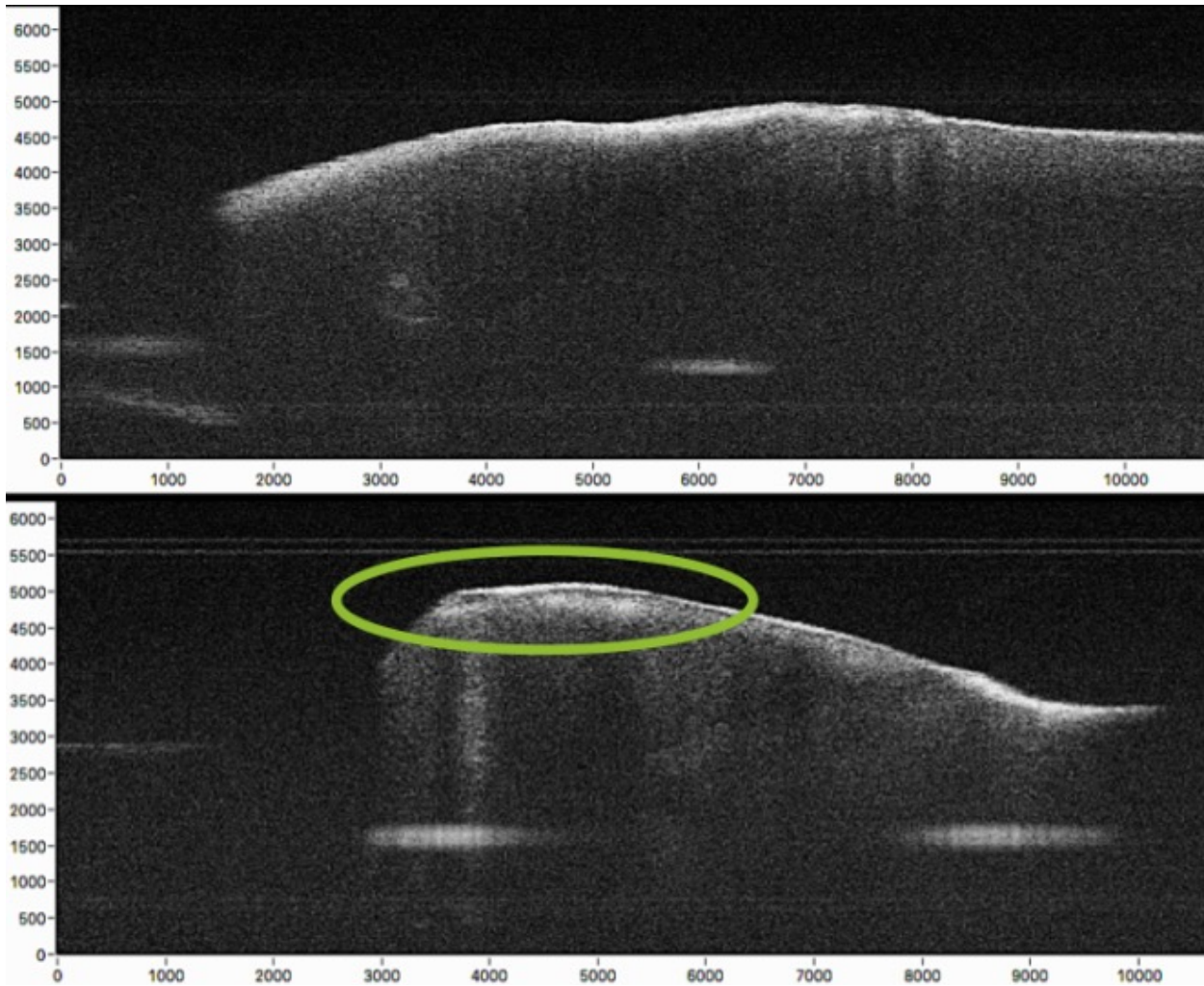


Figure 4.3 Sample OCT B-scans of active and arrested lesions

Top: A molar with an active lesion with no formation of transparent surface layer. *Bottom:* A molar with an arrested lesion with a clear formation of transparent surface layer (green oval). Dimensions measured in μm .

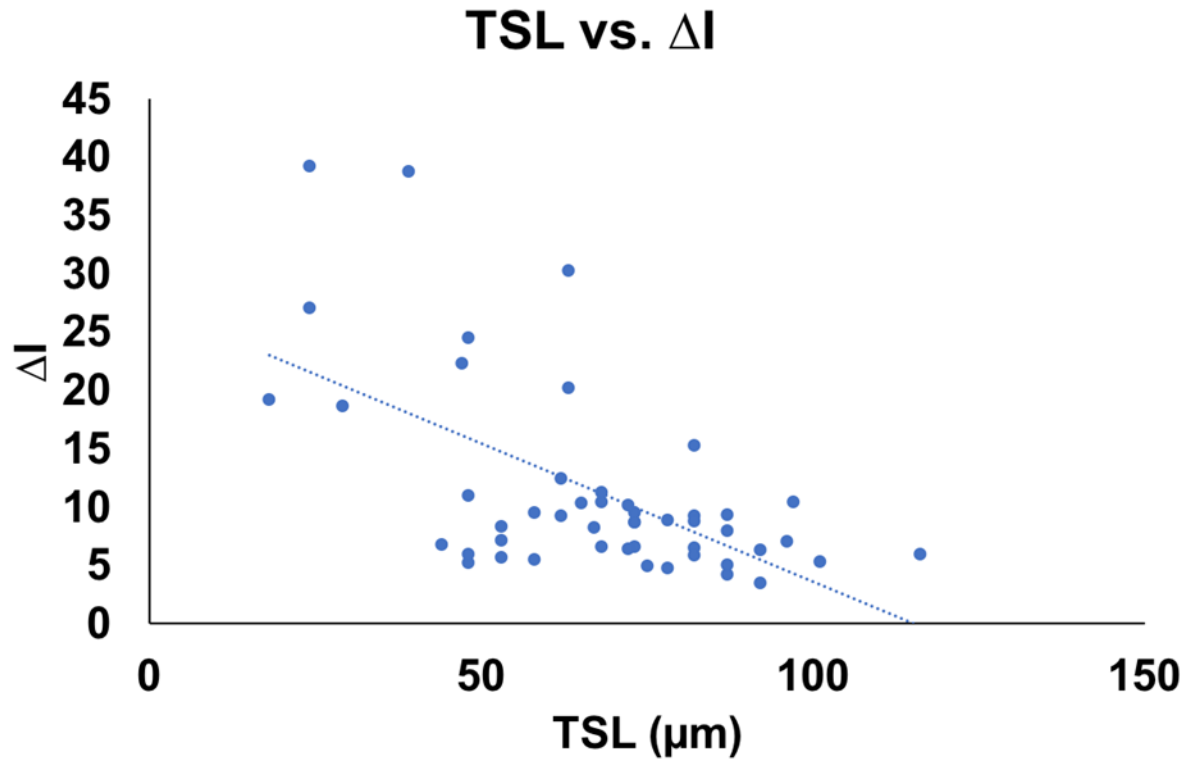


Figure 4.4 Correlation between SWIR permeability and OCT measurements

The relationship between SWIR reflectance permeability measurement and transparent surface layer thickness as measured by OCT appears to be significantly negative ($r = -0.49$, $p < 0.05$).

CHAPTER V

***EX VIVO* ASSESSMENT OF SECONDARY ENAMEL LESION ACTIVITY BY SWIR AND
THERMAL DEHYDRATION, OPTICAL COHERENCE TOMOGRAPHY, AND MICROCT**

5.1 Summary

Secondary caries occurs when leakage in the interfaces between restorative materials and tooth structure allow fluid and bacterial acid infiltration. Previous in vitro and in vivo studies on enamel and root surfaces using shortwave-infrared (SWIR) and thermal imaging during dehydration with forced air have been promising for assessing lesion activity. We hypothesize that these methods can be used to assess the permeability of and to monitor secondary lesions.

Sixty-three extracted human teeth with total of 109 suspected secondary lesions were assessed for permeability by both SWIR and thermal dehydration imaging. The presence and thickness of the remineralized transparent surface layer (TSL) of the lesions were measured by optical coherence tomography (OCT). Micro-computed tomography (MicroCT) was used to further confirm lesion severity and structure. OCT and MicroCT results were correlated with dehydration rates to determine lesion activity.

TSL thickness was significantly negatively correlated with both SWIR and thermal permeability measurements up to TSL=70 μm . At TSL >70 μm , there is no further increase in correlation. There is significant relationship between the TSL thickness and permeability measurements for smooth surface lesions, but not for occlusal and incisal lesions.

Increasing TSL thickness led to decreased permeability of lesions, potentially indicating lesion arrest at TSL ≥ 70 μm . SWIR performed better than thermal imaging for secondary lesion activity assessment, although both methods performed best on smooth surface lesions. These results further substantiated the usefulness of SWIR permeability measurements and OCT as promising methods for clinically assessing secondary lesion activity.

5.2 Introduction

In recent years, the prevalence of using shade-matched and radiopaque dental restorative materials for replacing decayed tooth structure after cavity preparation has led to a marked increase in the formation of secondary caries lesions, attributed by several clinical placement

factors. Dentists now spend more time repairing and/or replacing failed restorations than placing new ones. Maladaptation of bonding materials to tooth structure permits the microleakage of fluids and bacterial acid, resulting in the demineralization of tooth structure extending beneath the restoration. Clinicians are trained to rely on tactile sensation via the dental explorer and visual inspection to determine whether the decay is active or arrested (Fejerskov & Kidd, 2003). Such methods that rely on texture and color are highly subjective and unreliable (Pitts, 2009). Often tooth structure is heavily stained and stain is commonly mistaken for demineralization. A major advantage of SWIR imaging is that stains do not interfere at wavelengths longer than 1100 nm (Almaz et al., 2016; Ng et al., 2019; Zhu & Fried, 2022). Moreover, tooth-like, radiopaque restorative materials may mask secondary lesions, further complicating their detection and diagnosis with current methods. Accurate assessment of lesion activity, depth, and severity is important for clinicians to decide whether intervention is necessary.

A key indicator that lesions have become arrested due to remineralization is the formation of a highly mineralized transparent surface layer on the outer layers of the lesions (Chan et al., 2016; N.-Y. N. Chang et al., 2018, 2019; Jones et al., 2006; Jones & Fried, 2006; Kang et al., 2012; E. A. Kidd, 1983; E. A. M. Kidd & Fejerskov, 2004; Schüpbach et al., 1992). The presence of such a layer greatly inhibits the diffusion of fluids in and out of the lesion. Conversely, active lesions lack such a layer and possess a much higher permeability. Hence, the rate of water diffusion out of the lesion reflects the degree of lesion activity. Effective employment of new optical diagnostic technologies that can exploit changes in the light scattering of sound and carious tooth structure, and restorative materials have great potential for diagnosing the present state of secondary lesions (Simon et al., 2016).

Previous studies have demonstrated that the optical changes due to the loss of water from porous lesions can be used to assess lesion severity and activity with fluorescence, shortwave-infrared (SWIR) and thermal imaging (Ando et al., 2017; Kaneko et al., 1999; R. C. Lee, Darling, Staninec, et al., 2016; R. C. Lee et al., 2015; R. C. Lee, Staninec, et al., 2016; Usenik et al., 2014;

Zakian et al., 2010). We have investigated the use of SWIR reflectance methods to indirectly assess water diffusion rates from lesions since the porosity of the outer layers of active lesions is significantly greater than arrested lesions (Chung et al., 2011; W. A. Fried et al., 2013; R. C. Lee et al., 2015; Simon et al., 2014). Sound enamel appears transparent in SWIR wavelengths, whereas early demineralization increases SWIR scattering and reflectance. The incident SWIR light is absorbed by the water in the pores at the lesion surface, particularly at wavelengths such as 1460 and 1950 nm that coincide with water molecular absorption bands, thereby reducing surface scattering and lesion contrast. Extrinsic water loss during lesion dehydration therefore produces a marked increase in reflectivity and lesion contrast. Previous studies have shown great potential for SWIR reflectance imaging at 1950 nm for monitoring carious lesion activity with high sensitivity and efficacy due to the enhanced water absorption (J. T. Tressel et al., 2021).

Temperature changes on tooth surfaces during air drying have been exploited to assess lesion activity via thermal imaging. Previous studies utilizing thermal dehydration imaging for assessing the activity of lesions on coronal and root surfaces both *in vivo* and *in vitro* have shown considerable promise (Kaneko et al., 1999; R. C. Lee, Darling, Staninec, et al., 2016; R. C. Lee et al., 2015; R. C. Lee, Staninec, et al., 2016; Zakian et al., 2010). Measured temperature changes reflect the amount of water that diffuses from pores in the lesion to evaporate from the surface (R. C. Lee et al., 2015; V. Yang et al., 2020). In addition, since water tends to pool in gaps and crevices, we postulate that thermal imaging may be able to highlight gaps between restorative materials and tooth structure where there is increased microleakage. Such areas should experience larger temperature drops due to greater water retention in such gaps. In a recent thermal imaging study of root caries lesions, pockets in the gingiva were much cooler than the surrounding tooth structure due to water pooling in such areas (V. Yang et al., 2020). Therefore, both SWIR and thermal dehydration imaging methods have significant clinical potential for the nondestructive assessment of the activity of secondary caries lesions. Improving caries diagnosis should reduce the unnecessary replacement of composite restorations.

Several studies have demonstrated the utility of Optical Coherence Tomography (OCT) to acquire high resolution images of lesion structure and activity *in vivo* (N.-Y. N. Chang et al., 2019). When used at SWIR wavelengths, OCT is useful in determining whether lesions are active and expanding, partially arrested and undergoing remineralization, or fully arrested and remineralized (Jones et al., 2006; Jones & Fried, 2006; Kang et al., 2012; R. C. Lee et al., 2014; Mandurah et al., 2013). This imaging method resolves the reflectivity of each layer of sound and lesion structures, as well as restorative materials. OCT has also been particularly valuable for the measurement of gaps between restorative materials and tooth structure (Jones et al., 2004; Kang et al., 2012). Most importantly, OCT can detect the presence of a transparent zone of high mineral content at the lesion surface formed due to remineralization which serves as a key indicator that the lesion has become arrested. Such transparent surface zones have been clearly resolved in OCT images of lesions both *in vitro* and *in vivo* on coronal and root surfaces (N.-Y. N. Chang et al., 2018, 2019; V. Yang et al., 2020).

The purpose of this study is to develop methods to assess secondary lesion activity using SWIR and thermal imaging and OCT. We hypothesize that lesion characteristics such as lesion depth (LD), integrated reflectivity (ΔR), and thickness of the formation of the highly mineralized transparent surface layer (TSL) correlate with the lesion permeability and activity. In this study, we correlated the results from SWIR and thermal dehydration measurements to that of OCT measurements for each lesion to establish a relationship for further evaluation of lesion activity. We also acquired MicroCT images to provide confirmation of lesion structure and severity.

5.3 Materials and Methods

5.3.1 Sample Preparation

Sixty-three extracted human teeth collected from oral surgeons were assessed by clinicians for suspected secondary caries lesions. These teeth were sterilized with gamma radiation, mounted into black Delrin blocks using epoxy, and stored in a 0.1% thymol solution. Lesions on each tooth

were identified by surfaces per clinical standard, yielding a total sample size of n=109. **Figure 5.1** shows the workflow of the study design.

5.3.2 Visible Imaging

An USB-powered, Model 5MP Edge AM7915MZT digital microscope from AnMO Electronics Corp. (New Taipei City, Taiwan) equipped with eight white LED lights a visible polarizer to reduce glare was used to acquire 5 mega-pixel (2952 x 1944) color images of all sample surfaces.

5.3.3 SWIR Reflectance Dehydration Measurements

Samples were stored in a moist environment to preserve internal hydration. Each sample was immersed in a water bath and shaken to enhance water diffusion prior to measurement, then placed into a custom fabricated sample mount. A computer-controlled air nozzle with a 1 mm aperture was positioned 5 cm away from the sample surface at a 20° angle. After the sample was removed from the water bath, an image was captured as an initial reference image and the air spray was activated. Continuous pressurized air at 25 psi was delivered from the air nozzle to dehydrate the sample as images were captured for 60 seconds (**Figure 5.2A**). The SWIR dehydration setup was automated using LabVIEW software (National Instruments, Austin, TX).

A Xeva-2.35-320 extended range InGaAs SWIR T2SL camera (Xenics, Leuven, Belgium) sensitive from 900 to 2350 nm was used to acquire SWIR reflectance images during the dehydration. The camera was equipped with two lenses, a Navitar f=35-mm SWIR optimized (f/1.4) lens and a 60 mm achromat lens positioned 40 mm from the 35 mm lens. A high extinction polarizer was used to acquire cross polarization images from 1500-2350 nm. The quantum efficiency peaks at 1500 nm near 65% and drops off rapidly to 30% after 1700 nm and drops off again to below 20% after 2000 nm.

A polarized, broadband amplified spontaneous emission (ASE) light source Model AP-ASE-2000 from AdValue Photonics (Tucson, AZ) with a center wavelength of 1959 nm and a bandwidth of ~100 nm (-3 dB), 230 nm (-30 dB) and an output power of 11 mW was used as the 1950 nm light source. The light source was directed at the sample at an incident angle of approximately 20° to reduce specular reflection and the source to sample distance was also fixed at 5 cm. SWIR reflectance images were processed and automatically analyzed using a dedicated program constructed with LabVIEW and MATLAB (MathWorks, Natick, MA) software. A region of interest (ROI) encompassing the whole sample was used and measurement was recorded for each time point. The mean intensities, ΔI 's, were derived from the area under the time-intensity curve

$$\Delta I = \sum_{t=1}^{60} (I_t - I_{min})$$

for lesion areas (ΔI_L) and control areas (ΔI_C). The difference and the ratio between ΔI_L and ΔI_C within the same sample denoted as ΔI_{L-C} and $\Delta I_{L/C}$, respectively, were compared to determine which approach is most sensitive to changes in lesion activity.

5.3.4 Thermal Dehydration Measurements

A similar dehydration setup for SWIR dehydration was used for thermal dehydration (**Figure 5.2B**). A Model A65 infrared (IR) thermography camera from FLIR Systems (Wilsonville, OR) sensitive from 7.5 – 13 μm with a resolution of 640 \times 512 pixels, a thermal sensitivity of 50 mK, and a lens with a 13 mm focal length was used to record temperature changes during the dehydration process. The ambient room temperature, flowing air temperature and water bath temperature were approximately 21°C (294.15 K) and were consistent throughout the experiment. The object emissivity was set to 0.92, and the atmospheric temperature was set to 294.15 K (Lin et al., 2009).

While humidity values were not recorded, every sample was measured under the same conditions, where the relative humidity was set at a default value of 50%. Previous studies have shown the area enclosed by the time-temperature curve represents the amount of heat absorbed or lost, ΔQ , that can be used as a quantitative measurement of porosity to discriminate between sound and demineralized tooth structure *in vitro* (Kaneko et al., 1999; R. C. Lee et al., 2015; Zakian et al., 2010). Thermal images were processed and analyzed using dedicated programs written in LabVIEW and MATLAB. ΔQ was calculated and recorded

$$\Delta Q = \sum_{t=1}^{60} (Temp_{max} - Temp_t)$$

for lesion areas (ΔQ_L) and control areas (ΔQ_C). The difference and the ratio between ΔQ_L and ΔQ_C within the same sample denoted as ΔQ_{L-C} and $\Delta Q_{L/C}$, respectively, were compared. Similar considerations as comparing ΔI 's warranted us to account for variations in temperature change throughout dehydration in comparing ΔQ 's.

5.3.5 Optical Coherence Tomography

An IVS-2000-HR-C OCT system from Santec (Komaki, Aichi, Japan) that utilizes a swept laser source and a handpiece with a microelectromechanical (MEMS) scanning mirror and imaging optics was used to acquire complete tomographic images of samples at a volume of 5 x 5 x 5 mm. The body of the handpiece is 7 x 18 cm with an imaging tip that is 4 cm long and 1.5 cm across. Images are captured in approximately 3 seconds at a wavelength of 1312 nm with a bandwidth of 173 nm with a measured resolution in air of 8.8 μm (3 dB). Measured lesion depths (LD) were divided by 1.6, the refractive index of enamel. The lateral resolution is 30 μm ($1/e^2$) with a measured imaging depth of 5 mm and depth resolution of 5 μm in air. Image analysis and lesion

structural measurements were carried out using Dragonfly from ORS (Montreal, Canada). The LD, the integrated reflectivity over the lesion depth (ΔR), and the presence of transparent surface layer (TSL) and its thickness, if any, were also calculated using built-in functions within Dragonfly software.

5.3.6 MicroCT Analysis & Evaluation

A Scanco Microcomputed X-ray tomography (MicroCT) 50 from Scanco USA (Wayne, PA) located at the UCSF Bone Imaging Core Facility was used to acquire 10 μm resolution images. Image analysis and lesion structural measurements (LD and surface layer (SL)) thickness were carried out also using Dragonfly. A built-in median filter at appropriate sigma for smoothing and a Sobel-operator for edge detection were used to determine the LD via multiple subsequent measurements using line profiles.

5.3.7 Data and Statistical Analysis

Microsoft Excel (Redmond, WA) and GraphPad Prism 9 (La Jolla, CA) were used for data aggregation, analysis, and graphical presentation. Pearson's correlation and the student t-test were used for comparing different measurements.

5.4 Results

5.4.1 SWIR Dehydration Measurements

An example of SWIR dehydration measurements for a lesion surface are shown in **Figure 5.3**. ΔI 's are represented by the areas enclosed by the time-intensity curves. The integrated heat map allowed the operator to designate the respective control and lesion ROIs. Across all the lesion surfaces, the dehydration curves typically exhibited an initial minimum as water absorbed most of the SWIR light. The sigmoidal increase represents the loss of water absorption and the increased reflectance of porous areas of demineralization. ΔI values for each lesion were further modified

by subtracting the respective control ΔI for each tooth from the lesion ΔI , represented as ΔI_{L-C} , and by dividing the respective lesion ΔI by control ΔI , or $\Delta I_{L/C}$. The ΔI_{L-C} amongst the lesions ranged from 1.83×10^4 to 3.16×10^6 ($6.49 \times 10^5 \pm 6.22 \times 10^4$ (mean \pm SEM)), where $\Delta I_{L/C}$ ranged from 1.10 to 40.3 (5.4 ± 0.6). The SWIR dehydration protocol and the collected ΔI 's were closely examined to avoid inclusion of any composite restorations, which exhibit high intensities on SWIR reflectance, in the lesion and the control ROIs.

5.4.2 Thermal Dehydration Measurements

Thermal dehydration measurements for the same lesion surface are shown in **Figure 5.4**. ΔQ values are represented by the difference between the areas enclosed by the time versus temperature dehydration curves. Across all the lesion surfaces, the dehydration curves typically exhibited an initial drop in temperature followed by a slow recovery to the ambient temperature. An overall average dehydration curve was not derived for every lesion as each lesion behaves differently. ΔQ values for each lesion were further modified by subtracting the respective control ΔQ for each tooth from the lesion ΔQ , represented as ΔQ_{L-C} , and by dividing the respective lesion ΔQ by control ΔQ , or $\Delta Q_{L/C}$. The ΔQ_{L-C} amongst the lesions ranged from 8 to 617 K·s (193.4 ± 13.4 K·s (mean \pm SEM)), where $\Delta Q_{L/C}$ ranged from 1.0 to 6.1 (1.7 ± 0.1). At the onset of dehydration for the sample in Fig. 4, the thermal image showed demarcation between composite material and tooth structure likely because the composite surface was rougher and retained more water after removing from water bath. Eventually, the thermal dehydration process was able to overcome the initial water retention and reveal the lesion area, specifically near the interface between the composite material and tooth structure. Although we observed that for a few samples the dehydration process was unable to overcome the non-lesion water retention, leading to higher ΔQ 's.

5.4.3 OCT Imaging

Sample OCT C- and B-scans for the same lesion surface are shown in **Figure 5.5**. Using previously developed processing workflow within the ORS Dragonfly environment, thresholding was performed as image segmentation to estimate the lesion depth (LD), and integrated reflectivity (ΔR) was calculated by averaging the intensity values across the ROI. If observed, the thickness of the transparent surface layer (TSL) was also measured. Estimated LDs ranged from 22 to 340 μm ($136 \pm 5 \mu\text{m}$ (mean \pm SEM)). ΔR ranged from 49 to 199 (153 ± 3) for all the lesions. As expected, ΔR was higher in the lesion area compared to the sound control area. There was a significant positive correlation between LD and ΔR ($r = 0.24$, $p < 0.05$). Of the 109 suspected lesions, 85 lesions had a detectable TSL above or within the lesion, with thicknesses varying from 16 to 100 μm ($53 \pm 2 \mu\text{m}$).

5.4.4 MicroCT Imaging

A MicroCT scan for the same sample shown in **Figure 5.5** is shown in **Figure 5.6**. Using a previously developed processing workflow within the ORS Dragonfly environment, a combination of a median filter for smoothing and a Sobel operator for edge detection were used to process the scans to obtain the lesion depth (LD). A surface layer (SL) for each lesion was also recorded. The LD ranged from 57 to 575 μm ($235 \pm 11 \mu\text{m}$ (mean \pm SEM)). The SL thickness ranged from 10 to 154 μm ($69 \pm 2 \mu\text{m}$).

5.4.5 Correlation of Thermal and SWIR Imaging with OCT and MicroCT Measurements

For OCT measurements, there was a significant positive correlation ($r = 0.24$, $p < 0.05$) between LD and ΔR , i.e., deeper lesions had a higher overall reflectivity. There was no significant correlation between the LD and either thermal (ΔQ) or SWIR (ΔI) measurements. The correlation between ΔR and ΔQ or ΔI appeared weakly positive; however, they were not statistically

significant. The exception was the correlation between ΔR and $\Delta Q_{L/C}$, where a significant positive relationship was observed ($r = 0.23$, $p < 0.05$). On the other hand, the TSL thickness was significantly negatively correlated with both dehydration methods, where the thicker the TSL, the lower the dehydration values (TSL and ΔI_{L-C} : $r = -0.75$, $p < 0.05$; TSL and ΔQ_{L-C} : $r = -0.54$, $p < 0.05$; TSL and $\Delta Q_{L/C}$: $r = -0.36$, $p < 0.05$) (**Figure 5.7 and Figure 5.8**). The exception was TSL and $\Delta I_{L/C}$, where the relationship was weakly negative but not statistically significant ($r = -0.21$, $p > 0.05$). In general, there was no significant correlation between SL as measured by MicroCT and ΔQ or ΔI . However, there was a significant positive correlation between TSL as measured by OCT and SL as measured by MicroCT ($r = 0.26$, $p < 0.05$) (**Figure 5.9**).

The influence of the TSL was further examined by investigating the influence of the TSL thickness on ΔQ or ΔI . We found that for TSL thicknesses $< 70 \mu\text{m}$, there is a significant negative correlation with most dehydration measurements (TSL and ΔI_{L-C} : $r = -0.75$, $p < 0.05$; TSL and ΔQ_{L-C} : $r = -0.52$, $p < 0.05$; TSL and $\Delta Q_{L/C}$: $r = -0.32$, $p < 0.05$) except for TSL and $\Delta I_{L/C}$ ($r = -0.145$, $p > 0.05$). However, for TSL's of $70 \mu\text{m}$ or more, there is no further increase in correlation. Unpaired t-tests further substantiated the significant difference between both dehydration values for lesions with TSL of $70 \mu\text{m}$ or less and those with TSL of $> 70 \mu\text{m}$ (ΔI_{L-C} : $t = 2.93$, $p < 0.05$; $\Delta I_{L/C}$: $t = 1.35$, $p < 0.05$; ΔQ_{L-C} : $t = 2.33$, $p < 0.05$).

We further analyzed the dehydration measurements and the respective OCT measurements based on lesion type: occlusal ($n = 11$), smooth surface (consists of buccal/facial, mesial, distal, lingual; $n = 69$), and incisal ($n = 5$). The correlation analysis showed that there is no significant relationship between the TSL thickness with ΔQ and ΔI for occlusal and incisal lesions. However, there were significant negative correlations of the TSL thickness with ΔQ and ΔI for smooth surface lesions (TSL and ΔI_{L-C} : $r = -0.78$, $p < 0.05$; TSL and ΔQ_{L-C} : $r = -0.54$, $p < 0.05$; TSL and $\Delta Q_{L/C}$: $r = -0.38$, $p < 0.05$) except for TSL and $\Delta I_{L/C}$ ($r = -0.22$, $p > 0.05$) (**Figure 5.10 and Figure 5.11**).

5.5 Discussion

Several studies have demonstrated the use of thermal and SWIR imaging coupled with dehydration methods to assess the permeability and the level of activity of simulated and natural lesions. This study employed similar imaging modalities to assess natural lesions surrounding composite restorations. Previous studies on SWIR reflectance and transillumination imaging of both *in vitro* and *in vivo* secondary caries revealed the capability for SWIR to differentiate between sound tooth structure, lesions, and composite restorations with high contrast (Logan et al., 2014; Simon et al., 2016). In this study, SWIR imaging at 1950 nm was advantageous for differentiating composite restorations and lesions from sound tooth structure. Despite the complex geometry and topography in a few lesions, SWIR reflectance dehydration was able to assess the permeability with relatively close correlation to OCT. Although, we did observe, too, that the type of restorative composite material used, and degree of surface roughness have led to a few hyperinflated intensities when no lesions were found in OCT or MicroCT images. Therefore, the accuracy of SWIR dehydration imaging is highly dependent on the user's ability to carefully designate the ROIs for comparisons between lesion ΔI 's and sound ΔI 's. Any inclusion of restorative areas in the ROIs may confound the dehydration value calculations leading to false positives (higher ΔI ; determining a lesion being active when it is arrested).

Previous studies have demonstrated the use of thermal imaging for assessing lesions activity *in vitro* and *in vivo*, but this is the first study to investigate it's use for imaging secondary caries lesions. An important characteristic of secondary decay is the presence of microleakage at the interfaces between restorative materials and tooth structures. Since areas of increased water pooling and retention yield larger drops in temperature after dehydration, we postulated that thermal imaging is likely to yield information regarding the magnitude of microleakage. Such water pooling has influenced thermal imaging of the pits and fissures of the occlusal surfaces (R. C.

Lee, Staninec, et al., 2016; Zakian et al., 2010). In our study, we similarly observed such behavior for occlusal surfaces, around cracks, and over certain restorative materials that appeared to retain more water, resulting in higher ΔQ values when OCT and/or MicroCT images indicated lesion arrest.

Thermal imaging principally detects changes in temperature due to water evaporation, but inherently does not help differentiate between composite materials and tooth structures due to similar values of thermal emissivity. Differences in the surface texture or composition of some composite materials do appear to increase water retention that enables differentiation from tooth structure. We observed that thermal imaging worked well when dehydration process was able to overcome the initial water retention and reveal the lesion area, specifically near the interface between the composite material and tooth structure. In a few samples where the dehydration process was unable to overcome the non-lesion water retention, false positives (higher ΔQ) was observed. Careful examination of the imaging series was required to ensure the correct designation of lesion and control ROIs to prevent errors in comparisons. Overall, SWIR dehydration seemed to outperform thermal dehydration in this study. ΔI seemed to be less affected than ΔQ by the complexities of occlusal anatomy and crevices of interfaces that tend to retain water and interfere with thermal dehydration. Thermal dehydration showed greater variability in the measurements compared to SWIR dehydration.

Previous studies have utilized different methods for the analysis of dehydration curves. For SWIR reflectance dehydration measurements, we have observed that while many lesions dehydration curves that exhibit sigmoidal growth, several lesions showed dehydration curves deviating from this fit. To be more inclusive with our analyses, instead of using the simpler derivation of $\Delta I = \Delta I_{t=0} - \Delta I_{t=60}$ (N.-Y. N. Chang et al., 2018, 2019), we chose to integrate the intensity over time. Employing two different ways of comparing dehydration values by calculating differences and ratios between that of the lesion and that of the control allows us to capture more

information presented by the complexities of lesion surfaces. While both differences (L-C) and ratios (L/C) of values between the lesion and the control areas within each sample correlated with TSL thickness, L-C values seemed to correlate more closely than L/C. L/C normalizes and potentially masks portions of the dehydration curve that attributed to the differences in permeability values between lesion and that of control areas; hence $\Delta I_{L/C}$ for all secondary lesions did not significantly correlate with TSL thickness, but ΔI_{L-C} did.

Even though the correlation analyses showed several comparisons of significant relationship between dehydration values and TSL thickness, dehydration values remain highly variable as evident by low Pearson's r values. A recent study from our group examined the initial intensity changes during SWIR dehydration measurements (J. T. Tressel et al., 2021). That study identified a larger initial delay in the rise in reflectivity during the first 5 seconds of dehydration for active lesions (overall growth rate, OGR) and provided an additional variable for differentiating certain lesions and their activities (R. C. Lee et al., 2015; R. C. Lee, Staninec, et al., 2016). Future studies are warranted to further elucidate the meanings of specific portions of dehydration curve to that of lesion structures and activities.

Lesion depth did not correlate with either type of dehydration measurement which was not surprising and has been observed previously (N.-Y. N. Chang et al., 2018, 2019; R. C. Lee, Staninec, et al., 2016). It is likely that the changes in temperature and reflectivity are limited to areas of the lesion that are near the lesion surface and deeper lesion areas have little influence on the dehydration dynamics. In addition, water loss for deeper lesions may require a longer duration for dehydration than was performed here. Alternatively, high subsurface reflectivity due to variable demineralization throughout the whole lesion might have obscured the true lesion depth, contributing to greater variation in the dehydration values for similar lesion depths.

Based on previous *in vitro* OCT studies using simulated lesions on flat surfaces, we expected ΔR to decrease with increasing TSL thickness due to remineralization (Kang et al., 2012;

Le et al., 2010; R. C. Lee et al., 2014). Here, the relationship was weakly negative but not statistically significant ($r = -0.02$, $p > 0.05$). It is likely that variation in the topography of the tooth influences remineralization. There is also larger variation of the lesion structure and orientation. Lesions with larger surface area with less demineralization may have similar ΔR 's compared to lesions with smaller surface area but greater demineralization. Another reason might be how SWIR light behaves differently with types of composite materials. Certain composites with opaque shades have titanium dioxide (TiO_2) added as an optical opacifier, which blocks the penetration of SWIR light and can interfere with imaging through composite. Coupled with surface roughness, these characteristics of structures surrounding secondary lesions might have obscured true lesion depth and ΔR if lesion is located beneath the composite material. Even so, previous work has demonstrated the ability for different OCT systems to adequately image simulated secondary lesions beneath different composite types *in vitro* (Jones et al., 2004; Stahl et al., 2010). Therefore, even though surface textures, composite material types, and OCT system types may affect OCT imaging of lesions, there are methods to circumvent such limitations and allow OCT to capture the status of secondary lesions nondestructively for clinical assessment of severity and activity.

Our results suggest that dehydration measurements performed differently amongst lesion types. Dehydration measurements seemed to correlate closer with TSL thickness for smooth surface lesions than non-smooth surface lesions (occlusal and incisal). Dehydration results appeared to correlate closely with the presence of a TSL measured using OCT. A previous study using simulated lesions indicated that a TSL thickness of $< 20 \mu\text{m}$ led to large permeability changes, and that thicknesses of $> 50 \mu\text{m}$ might have completely arrested *in vitro* lesions (N.-Y. N. Chang et al., 2018). Another *ex vivo* study also showed that coronal lesions with TSLs thicker than $75 \mu\text{m}$ led to significantly lower permeability, indicative of lesion arrest (N.-Y. N. Chang et al., 2019). In this study, we found similar comparisons, where lesions with TSLs $> 70 \mu\text{m}$ were significantly less permeable than lesions with thinner TSLs. Based on these results, we hypothesize that further increases in TSL will have limited influence on the lesion permeability.

This further provide evidence that dehydration measurements might be useful for decerning lesion activity.

Although the correlation between permeability measurements and TSL thickness by OCT was strong, the correlation between permeability and the surface layer thickness (SL) by MicroCT was not significant, even though the correlation between the TSL and SL thickness was significant. While almost all caries lesions possess some surface zone of increased mineral content, not all surface zones can be considered highly mineralized “transparent” surface zones that can be detected with OCT and have a mineral content close to sound enamel. In MicroCT, almost all the lesions had a surface layer of higher mineral content that was higher than the lesion body. OCT is highly sensitive to slight degrees of mineral loss, and we have previously confirmed that TSLs must contain mineral content near equivalent to sound enamel, making TSL thickness a better indicator of lesion activity compared to SL thickness (Chan et al., 2016; N.-Y. Chang et al., 2020; W. A. Fried et al., 2020; R. C. Lee, Darling, Staninec, et al., 2016; Zhu & Fried, 2022). A future study to correlate OCT TSL thickness and zone of similar mineral content in MicroCT SL may help further delineate the relationship between OCT and MicroCT for imaging carious lesions. Coupled with respective dehydration values, this will likely improve the diagnostic criteria for assessing whether lesions are active or arrested.

5.6 Conclusions

In this study, we employed modified permeability measurements previously developed to assess the activity of secondary caries lesions. The results suggest that the permeability increased significantly with increasing integrated reflectivity. Furthermore, small increases in integrated reflectivity led to large permeability changes. Increasing transparent surface layer thickness led to decreased permeability of lesions, potentially indicating an arrest in activity at thicknesses exceeding 70 μm . SWIR imaging performed better than thermal imaging for activity assessment for secondary caries lesions on tooth coronal surfaces. Thermal imaging performed well in

identifying crevices between composite material and tooth structure, but at times can be masked by the complex topography of the occlusal anatomy. SWIR imaging did not appear as susceptible to such interference, owing to the ability to differentiate composite materials, tooth structures, and lesions with high contrast. In all, permeability measurements performed best on smooth surface lesions. These results further substantiated the usefulness of SWIR permeability measurements and OCT as promising methods for assessing secondary lesion activity and severity.

5.7 Figures and Figure Legends

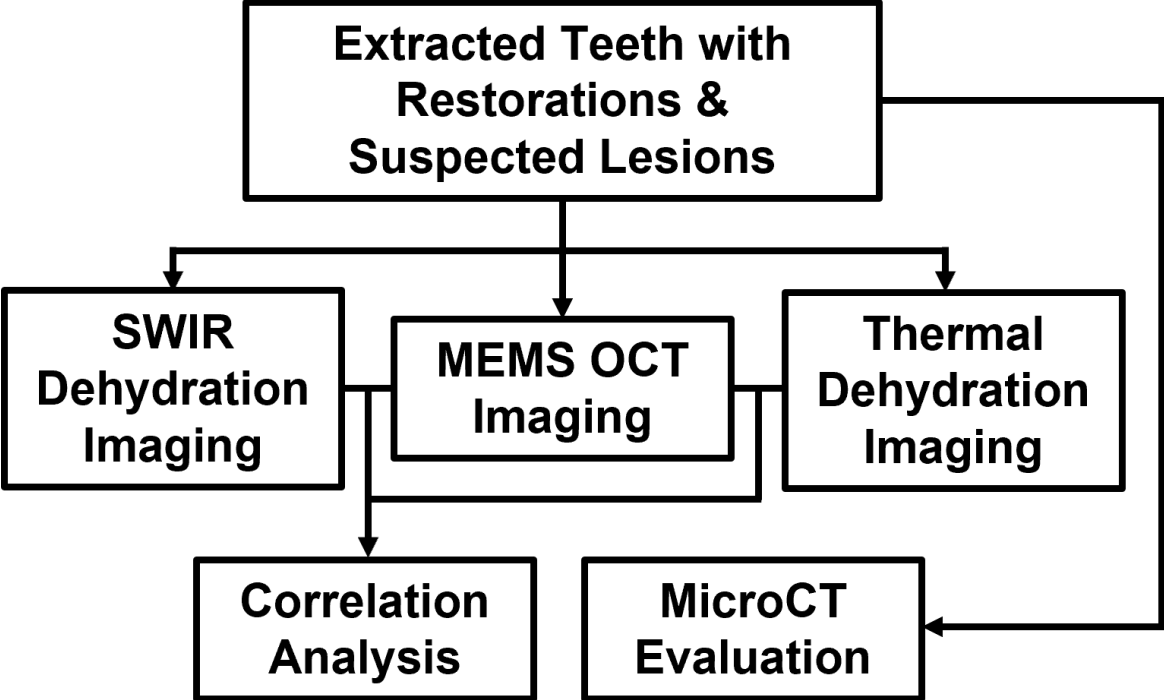


Figure 5.1 Workflow schematic

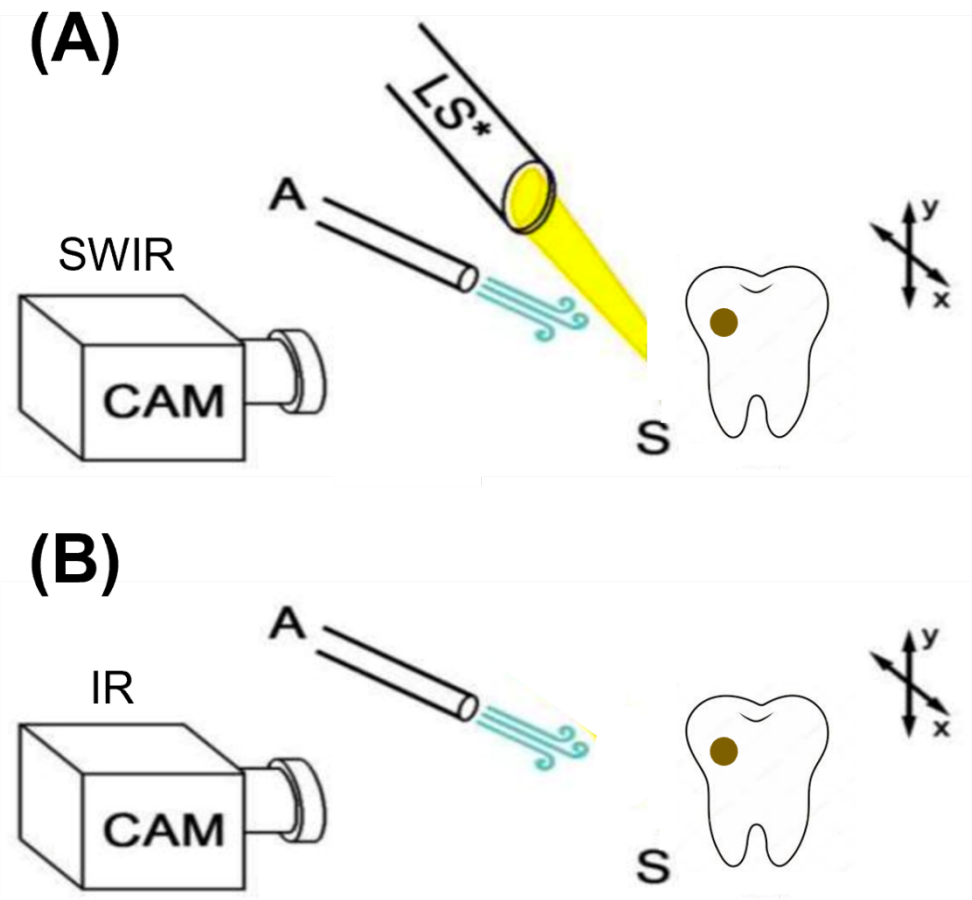
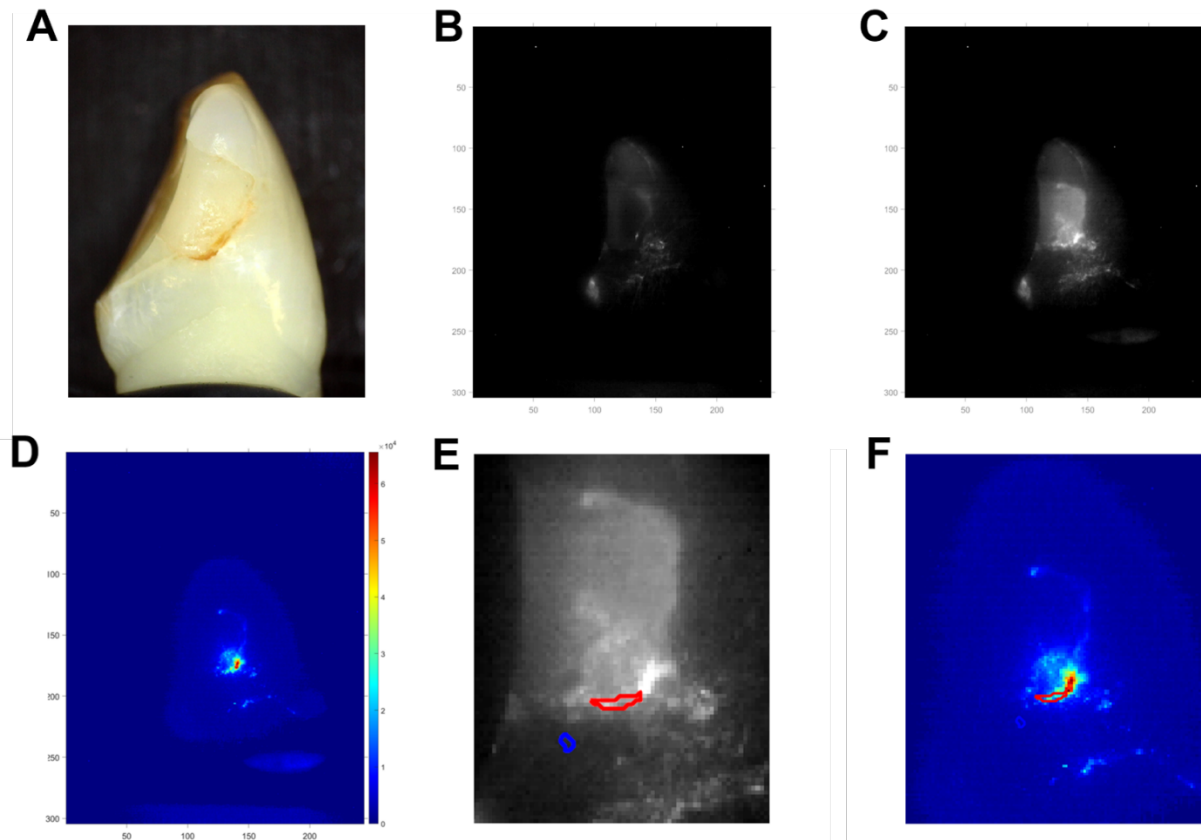


Figure 5.2 Permeability measurement setup

(A) SWIR dehydration setup. (B) Thermal dehydration setup. *LS* = light source at 1950 nm. *A* = air nozzle output at 25 psi. *F* = filter. *S* = *ex vivo* sample with suspected secondary lesion.



SWIR Dehydration Curves

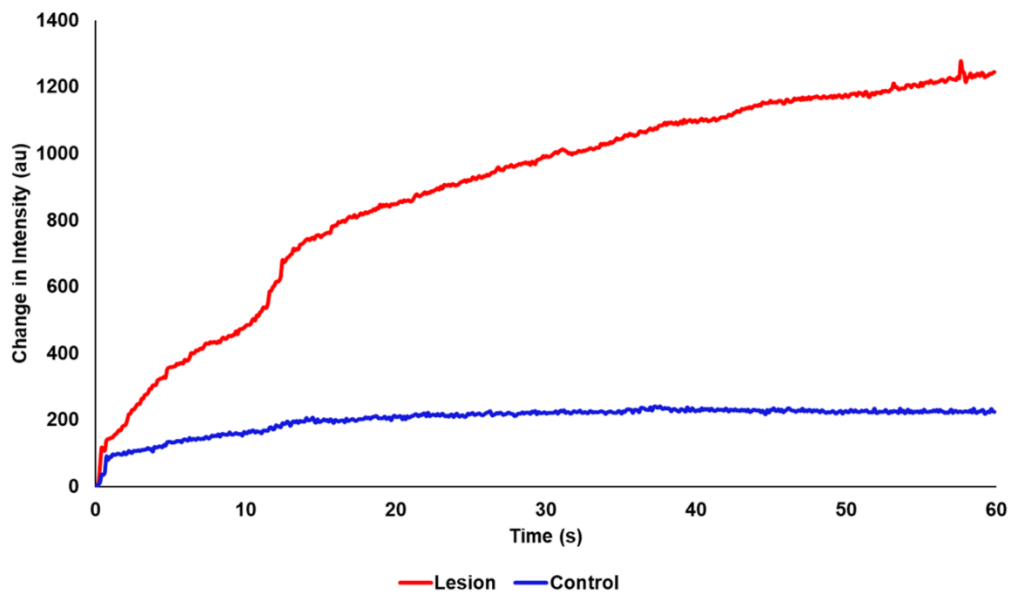
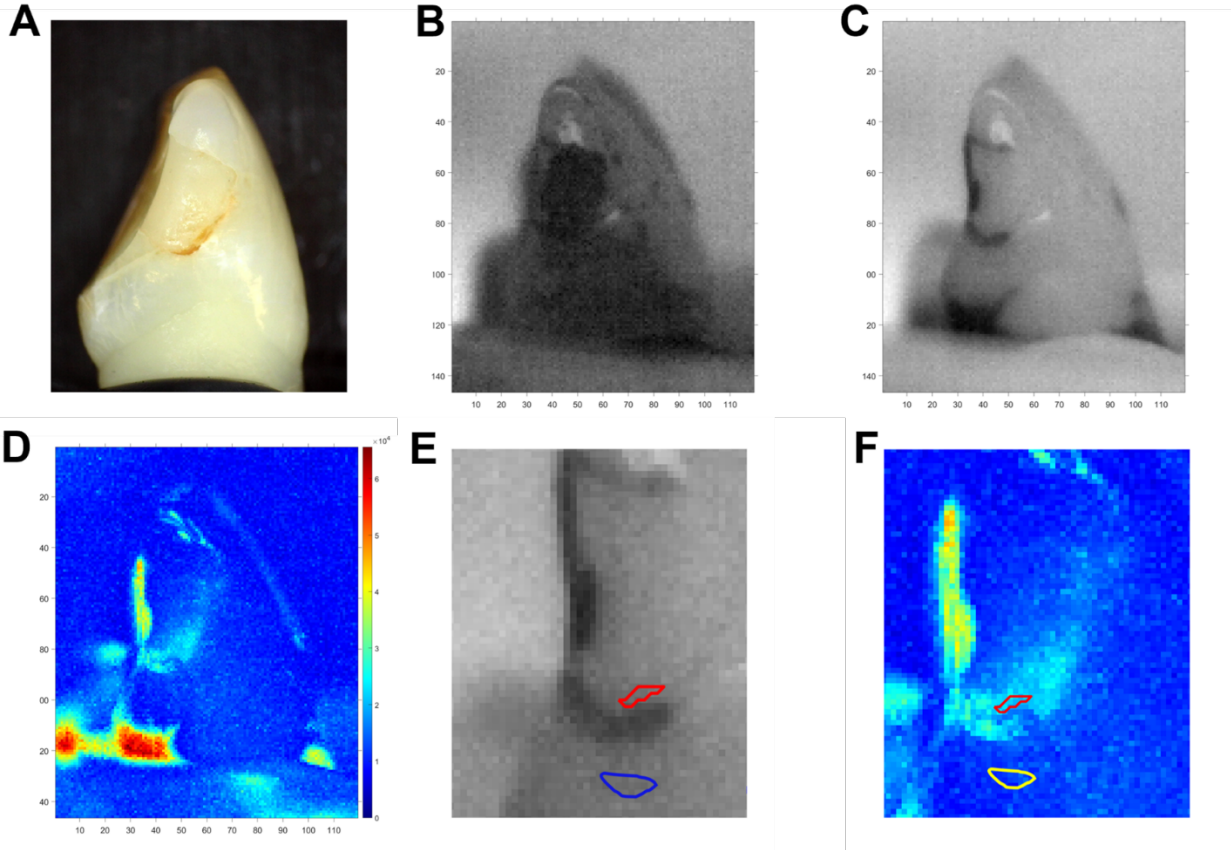


Figure 5.3 SWIR dehydration analysis results for one of the sample lesions

A) Visible image. B) SWIR image at onset of dehydration. C) SWIR image at the end of dehydration. D) Integrated SWIR reflectance intensity change presented as a heat map. E) SWIR image at the end of dehydration zoomed-in with ROIs (blue = control ROI, red = lesion ROI). F) Heat map zoomed-in with ROIs. *Bottom*: SWIR dehydration curves for control ROI (blue) and lesion ROI (red).



Thermal Dehydration Curves

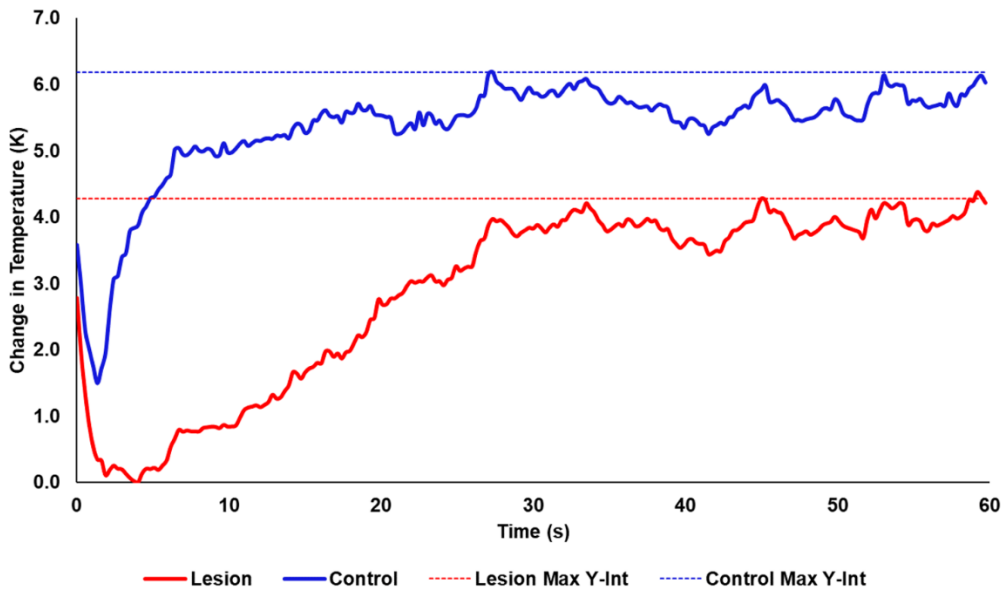


Figure 5.4 Thermal dehydration analysis results for the same sample lesion shown in Fig. 5.3

A) Visible image. B) Thermal image at onset of dehydration. C) Thermal image at the end of dehydration. D) Integrated thermal emissivity change presented as a heat map. E) Thermal image at the end of dehydration zoomed-in with ROIs (blue = control ROI, red = lesion ROI). F) Heat map zoomed-in with ROIs (yellow = lesion ROI). *Bottom*: Thermal dehydration curves for control ROI (blue) and lesion ROI (red).

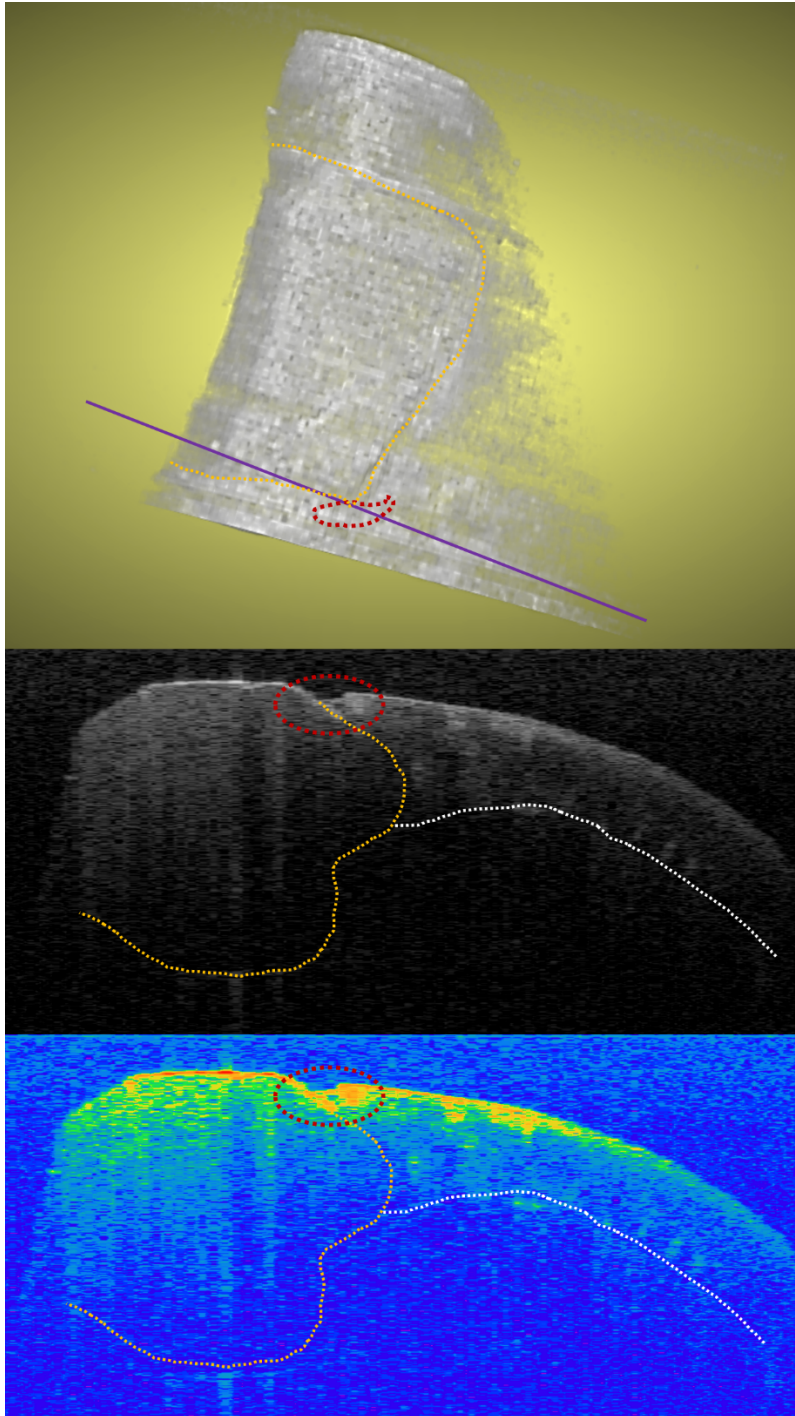


Figure 5.5 OCT scan of the same sample depicted in Fig. 5.3

Top: C-scan of the tooth surface with lesion. Orange-dotted area: composite restoration; red-dotted area: suspected secondary lesion area; purple line: location of 2D B-scan. *Middle:* 2D B-scan of secondary lesion. Orange-dotted line: interface between enamel and dentin; white-dotted line: dentoenamel junction (DEJ). *Bottom:* 2D B-scan of secondary lesion with threshold segmentation. Note the transparent surface layer enclosed by lesion.

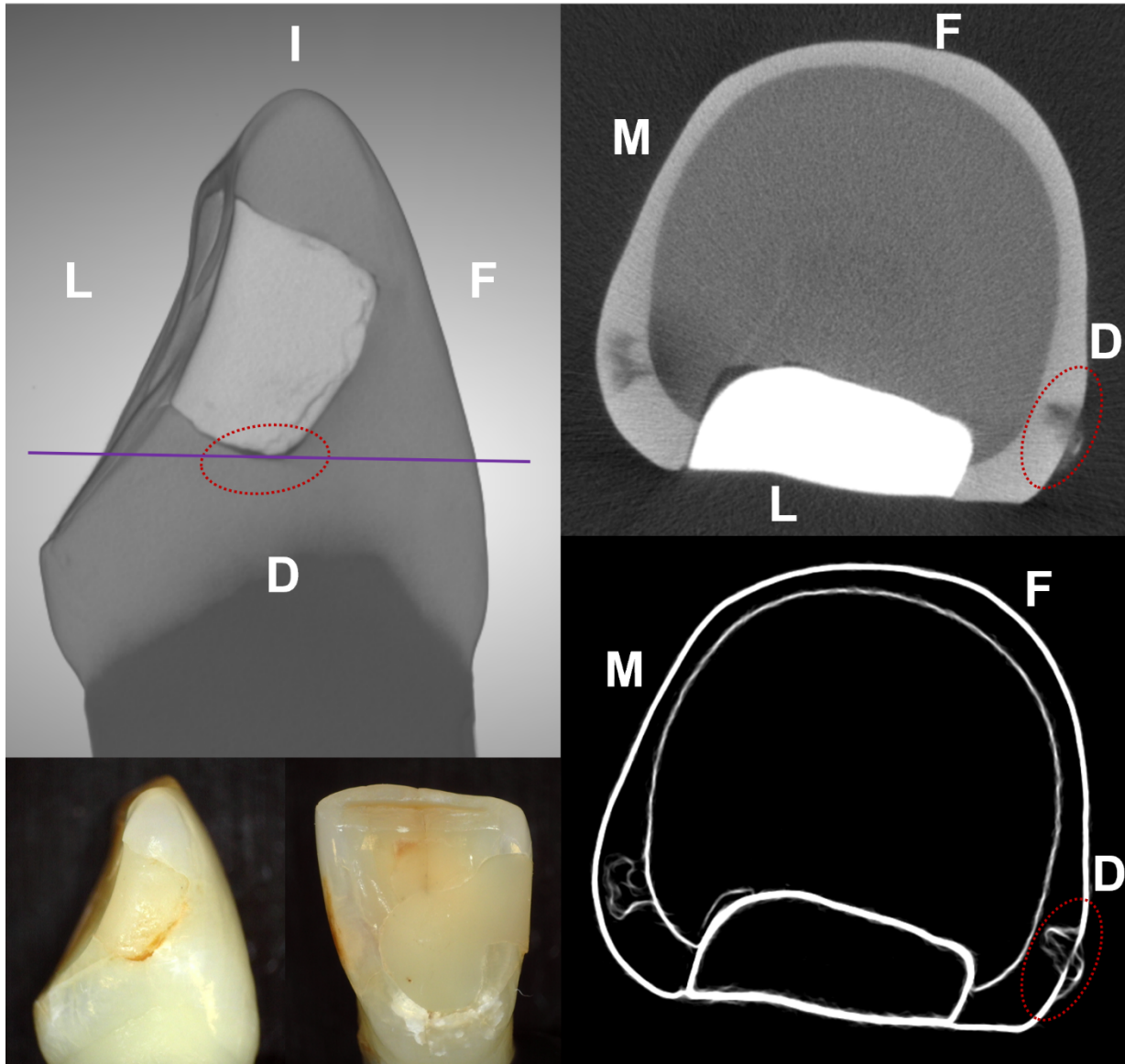


Figure 5.6 MicroCT scan of the same sample depicted in Fig. 5.3

Upper Left: 3D-scan of the tooth sample oriented to the suspected lesion surface. Purple horizontal line indicates the position of the transverse sectional view. *Lower Left:* Visible photos of the distal view (inset left) and the lingual view (inset right) of the same sample. Note that the composite restoration extends more apically beyond the level of the transverse section. *Upper right:* Transverse slice of the scan at the level of suspected lesion at the purple line position. *Lower Right:* Transverse slice of the scan at the level of lesion after median smoothing and Sobel-operator edge detection image filtering. Red-dotted oval depicts the suspected lesion area. Surfaces: D = distal, F = facial, I = incisal, L = lingual M = mesial.

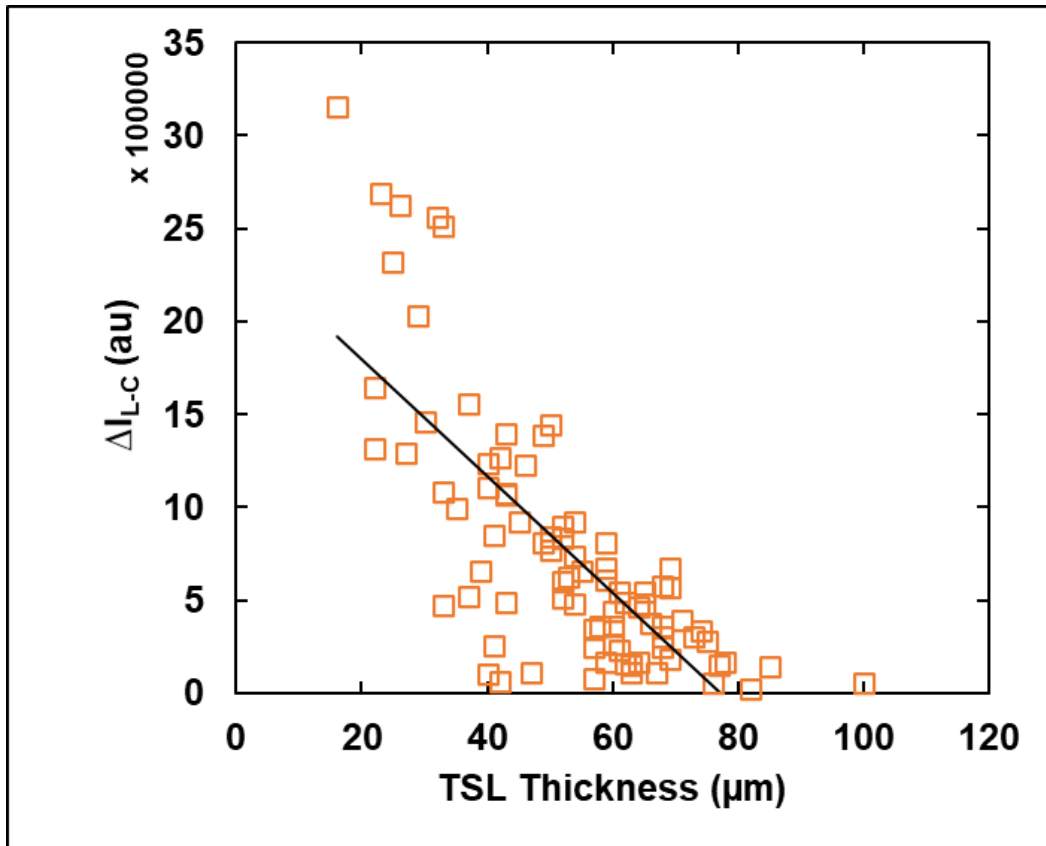


Figure 5.7 Correlation Plot: TSL vs. SWIR Permeability

Transparent surface layer thickness by OCT and SWIR dehydration measurement (ΔI_{L-C}) showed significantly negative correlation ($r = -0.75$, $p < 0.05$).

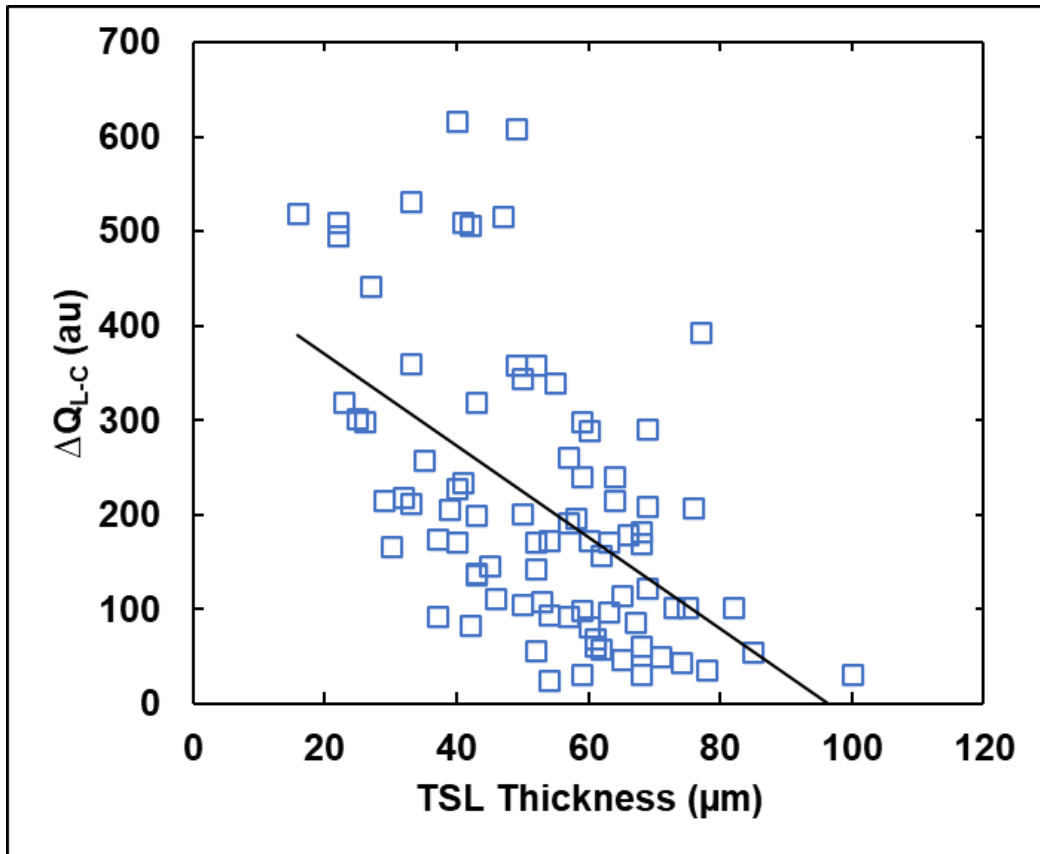


Figure 5.8 Correlation Plot: TSL vs. Thermal Permeability

Transparent surface layer thickness by OCT and thermal dehydration measurement (ΔQ_{L-c}) showed significantly negative correlation ($r = -0.54$, $p < 0.05$).

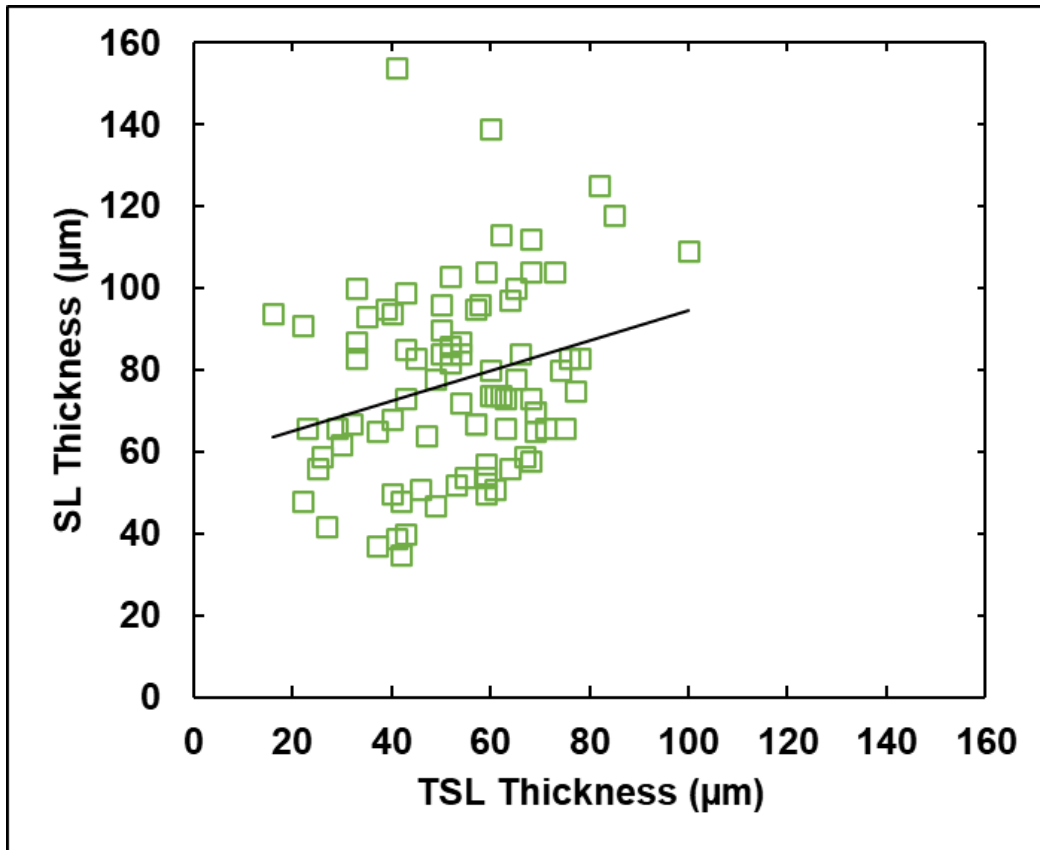


Figure 5.9 Correlation Plot: TSL vs. SL

Transparent surface layer thickness by OCT and surface layer by MicroCT showed significantly positive correlation ($r = 0.26$, $p < 0.05$).

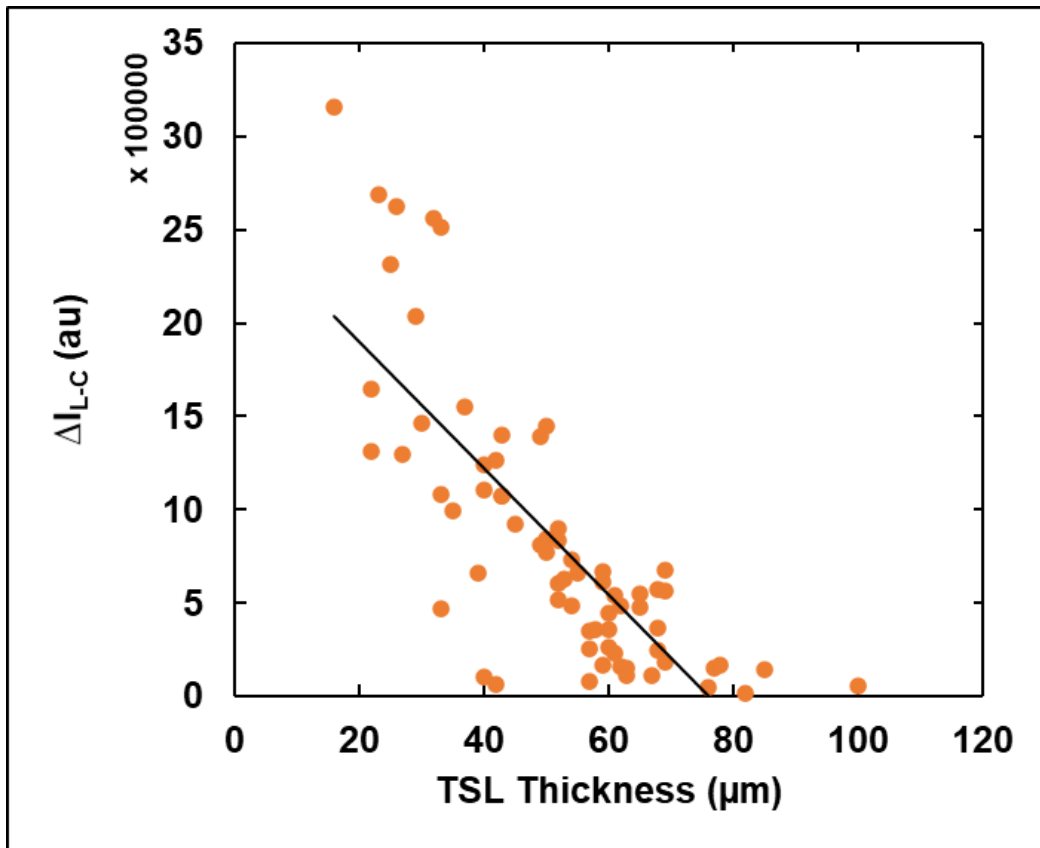


Figure 5.10 Smooth Surface Lesion Correlation Plots: TSL vs. SWIR Permeability

TSL by OCT and SWIR dehydration measurements (ΔI_{L-C}) showed significantly negative correlation ($r = -0.78$, $p < 0.05$) for smooth surface secondary lesions.

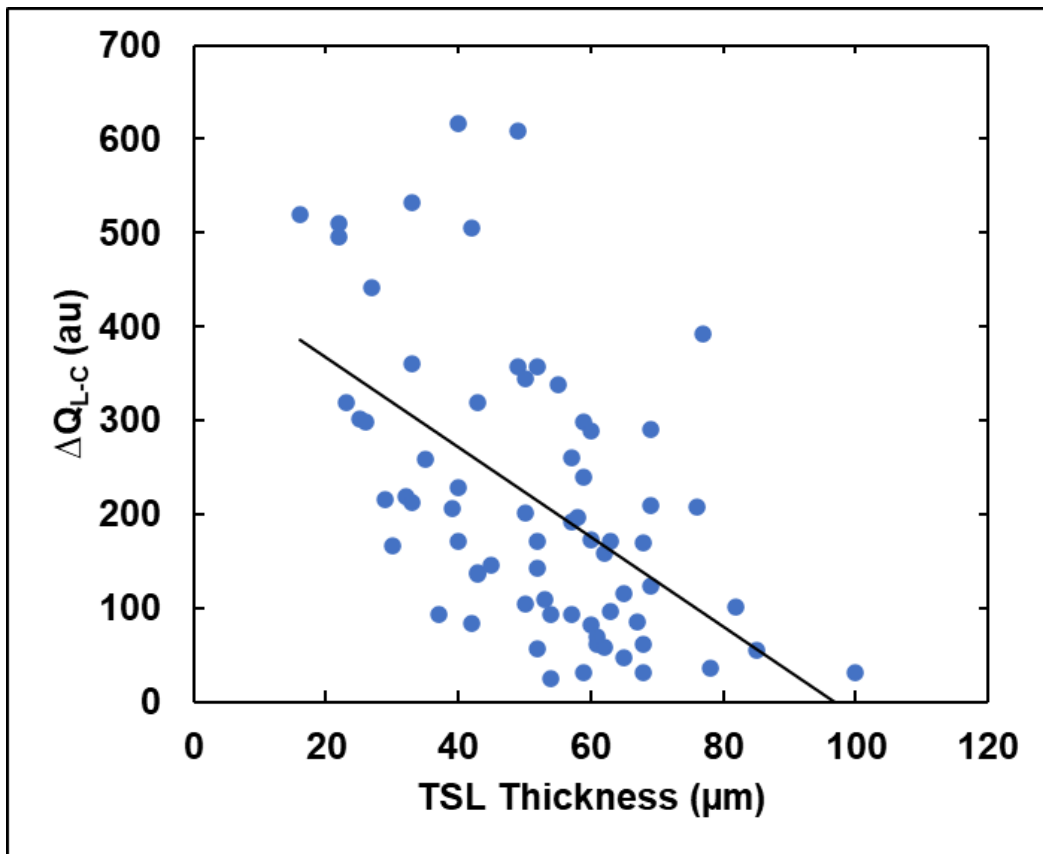


Figure 5.11 Smooth Surface Lesion Correlation Plots: TSL vs. Thermal Permeability

TSL by OCT and thermal dehydration measurements (ΔQ_{L-C}) showed significantly negative correlation ($r = -0.54$, $p < 0.05$) for smooth surface secondary lesions.

CHAPTER VI

***EX VIVO* EVALUATION OF SWIR AND THERMAL IMAGING PROBES FOR THE ASSESSMENT OF THE ACTIVITY OF CORONAL AND ROOT CARIES LESIONS**

6.1 Summary

New imaging methods are needed to assess the activity of caries lesions on tooth surfaces. Recent studies have shown that changes in the contrast of lesions during dehydration with air at SWIR and thermal wavelengths can be used to determine if lesions are active or arrested. For this investigation, changes in the reflectance of caries lesions during dehydration with air was monitored at 1500-1750 nm and on interproximal and occlusal surfaces of extracted teeth using an imaging system with an InGaAs camera, a light source, and a 3D printed handpiece with an integrated air nozzle suitable for clinical use. Changes in the thermal emission of root caries lesions on extracted teeth during dehydration with air was also monitored using an imaging system with a miniature thermal camera and a 3D printed handpiece with an integrated air nozzle suitable for clinical use. The studies evaluated the performance of the SWIR and thermal camera for imaging coronal and root caries on extracted teeth prior to their use for *in vivo* studies.

Lesion structure was also assessed with optical coherence tomography and microCT for comparison. These preclinical studies demonstrated that a 3D printed appliance with integrated air for dehydration can be used to acquire SWIR and thermal dehydration curves similar to those acquired previously by benchtop imaging systems. There was a significant difference in the thermal response of sound and root lesion areas of human teeth under dehydration at constant airflow.

6.2 Introduction

Caries lesions can be arrested by the preferential deposition of mineral at the lesion surface that inhibits diffusion into the lesion and reduces the rate of water loss (Cate & Arends, 1977; Lepri et al., 2013; ten Cate & Featherstone, 1991). Since arrested lesions do not need further intervention, an accurate assessment of lesion activity is paramount for clinical diagnosis.

Many lesions have been arrested or do not require intervention. Even so, it is difficult to identify active lesions with current diagnostic methods. Accurate assessment of lesion activity,

depth, and severity is important to determine whether intervention is necessary. Gold standards for lesion assessment such as transverse microradiography (TMR) and polarized light microscopy (PLM) either require destruction of the tooth, or in the case of microCT are unsuitable for use *in vivo*. New non-destructive diagnostic tools are needed that can assess lesion activity with a single measurement. Effective employment of new optical diagnostic technologies that can exploit the changes in the light scattering of the lesion have great potential for diagnosing the present state of the lesions. Therefore, the development of new methods, such as short wavelength infrared (SWIR) imaging and thermal imaging, are needed for the clinical assessment of lesion activity to avoid unnecessary cavity preparations.

Clinical diagnosis of root caries is highly subjective and is based on visual and tactile parameters. In contrast to coronal caries, root caries lacks a valid diagnostic standard, such as radiography (Banting, 2001). Moreover, early root caries lesions are much more difficult to detect than the early incipient white spot lesions seen with coronal caries. There are often no clinical symptoms with root caries, although pain may be present in advanced lesions. Traditional methods of visual-tactile diagnosis for root caries can result in a correct diagnosis, but not until the lesion is at an advanced stage (Banting, 2001). In addition, investigators have not developed a reliable relationship between lesion appearance and activity (Banting, 1993; Hellyer et al., 1990; Schaeken et al., 1991). Even though most experts agree that active root lesions are soft, tactile hardness assessments remain subjective and lack reliability (Banting, 1993). Multifactorial root caries scoring systems have been developed with mixed success (Ekstrand et al., 2008; Fejerskov et al., 1991). More recently, the International Caries Detection and Assessment System (ICDAS) coordinating committee and Ekstrand et al. proposed clinical scoring systems for assessing root caries lesion activity (Ekstrand et al., 2008; Ismail, 2005). Criteria include: color (light /dark brown, black); Texture (smooth, rough); Appearance (shiny or glossy, matte or non-glossy); Tactile (soft, leathery, hard); Cavitation (loss of anatomical contour); and proximity to the

gingival margin (Pitts, 2009). However, such clinical methods for root caries lesion activity assessment lack histological validation and are composed of only visual and tactile exams, which are prone to subjective bias and interference from staining (Lynch & Beighton, 1994). Histological analyses for lesion assessment such as transverse microradiography (TMR) and polarized light microscopy (PLM) require destruction of the tooth and are not suitable for use *in vivo*. Incorrect diagnosis can result in under treatment or over treatment. If a decision to restore is made prematurely when remineralization was feasible, the patient is committed to a restoration, or replacement restorations, that can become progressively larger. If the lesion is active and intervention is delayed, often the patient will require a root canal or extraction.

When lesions become arrested by mineral deposition, or remineralization, in the outer layers of the lesion, the diffusion of fluids into the lesion is inhibited. Hence, the rate of water diffusion out of the lesion reflects the degree of lesion activity. Previous studies have demonstrated that the optical changes due to the loss of water from porous lesions can be exploited to assess lesion severity and activity with fluorescence, thermal, and SWIR imaging (Ando et al., 2017; Kaneko et al., 1999; R. C. Lee et al., 2015, 2017; R. C. Lee, Staninec, et al., 2016; Usenik et al., 2014; Zakian et al., 2010). Since arrested lesions and developmental defects (fluorosis) are less permeable to water due to the highly mineralized surface layer, changes in the rate of water loss can be related to changes in lesion structure and porosity. We have investigated optical methods for assessing water diffusion rates from lesions since the porosity of the outer layers of active lesions is significantly greater than arrested lesions. This can be indirectly measured via SWIR reflectance methods (Chung et al., 2011; W. A. Fried et al., 2013; Simon et al., 2014). Normal enamel is transparent at SWIR wavelengths, whereas early demineralization causes increased SWIR reflectance due to scattering. Water in the pores at the surface of the lesion absorbs the incident SWIR light, particularly at wavelengths greater than 1450 nm, reducing surface scattering and lesion contrast. Loss of that water during dehydration produces a marked increase in reflectivity and lesion contrast.

Although the penetration depth of near-IR light is limited in dentin compared to enamel, high quality images of early root caries and demineralization in dentin are feasible (Amaechi et al., 2004). CP-OCT has been used successfully to measure demineralization in simulated caries models in dentin and on root surfaces (cementum) (C. Lee et al., 2009; Manesh et al., 2009a, 2009b). CP-OCT has also been used to measure remineralization on dentin surfaces and to detect the formation of a highly mineralized layer on the lesion surface after exposure to a remineralization solution (Manesh et al., 2009a). OCT has also been used to help discriminate between non-carious cervical lesions and root caries *in vivo* (Wada et al., 2015). Kaneko et al. and Zakian et al. (Kaneko et al., 1999; Zakian et al., 2010) demonstrated that lesions on coronal surfaces could be differentiated from sound enamel in thermal images. We recently demonstrated that thermal imaging via dehydration can be used to assess lesion activity on both enamel (R. C. Lee et al., 2015) and dentin surfaces. In previous studies, thermal imaging during lesion dehydration was more successful than near-IR imaging for assessing lesion activity on root and dentin surfaces (R. C. Lee et al., 2017).

The only clinical study that has been carried out using optical methods to assess lesion activity via forced air-drying employed fluorescence on smooth surface enamel lesions (Ando et al., 2017). The purpose here is to develop and evaluate SWIR reflectance probe and thermal imaging probe suitable for lesion activity measurements *in vivo*. We built handheld SWIR and thermal imaging probes with miniature SWIR and thermal cameras and 3D printed handpieces with integrated air nozzles suitable for clinical use. SWIR measurements were performed on extracted teeth with lesions on tooth occlusal and interproximal surfaces. We evaluated the performance of the handheld thermal imaging probe for imaging root caries on extracted teeth. Higher resolution OCT and microCT images of lesion structure were used as a gold standard to assess lesion activity for comparison.

6.3 Materials and Methods

6.3.1 Sample Preparation

Total 28 extracted teeth from patients in the San Francisco Bay Area were collected, cleaned, sterilized with gamma radiation, and stored in a 0.1% thymol solution to maintain tissue hydration and prevent bacterial growth. Twelve of 28 were selected for occlusal and approximal lesions and the other 16 teeth containing root lesions were then mounted on 1.2 x 3 cm rectangular blocks of black orthodontic composite resin with the outward tooth lesion surface facing upwards. The teeth were imaged using Microcomputed X-ray tomography (μ CT) with a 10- μ m resolution. A Scanco μ CT 50 from Scanco USA (Wayne, PA) located at the UCSF Bone Imaging Core Facility was used to acquire the images.

6.3.2 Design and Fabrication of SWIR and Thermal Dehydration Imaging Probes

The probe was designed in Fusion 360 from Autodesk (San Francisco, CA). The reflectance probe body utilized black resin to reduce artifacts from unwanted scattering in the probe assembly. A side view of the reflectance probe body is shown in **Figure 6.1A**. The reflectance fiber comes in from the back of the probe, and light is diffusely scattered to the sample. The bottom of the reflectance probe is designed to be attached to the camera, and the camera view is reflected off an aluminum mirror fitted to a 45° angle attached to the top of the probe. There is an air nozzle near the mirror to prevent fogging of the mirror. The air nozzle can also be used to dry the lesion to increase lesion contrast and potentially assess lesion activity (R. C. Lee et al., 2015, 2017; R. C. Lee, Staninec, et al., 2016). The handpiece body was printed with standard black resin from Formlabs (Somerville, MA) using Form 2 and 3 printers. These probes were printed using the standard black resin and a right-angle mirror was attached at the distal end of the handpiece.

For SWIR imaging, a SLS201L Stabilized Tungsten-Halogen lamp from Thorlabs (Newton, NJ) with a 1500-nm long pass filter and a 1 mm in diameter low-OH optical fiber was used as the light source for reflectance. The SWIR reflectance images were captured using a 12-bit Model

GA1280J (Sensors Unlimited, Princeton, NJ) with a 1280 x 1024-pixel format and 15- μm pixel pitch. A lens assembly consisting of 1 inch in diameter $f=200$ and 60 mm lenses along with an adjustable aperture was attached to a 3D printed handpiece equipped with a 10 mm aluminum mirror with channels for air and the 1 mm optical fiber. The distal end of the 1 mm fiber was inserted into a Teflon plug to provide diffuse illumination. Air at 25 psi was connected to the probe as shown in **Figure 6.1** for dehydration of the lesion.

Thermal images were captured using a FLIR Boson 640 (Wilsonville, Oregon) thermal camera that uses an uncooled vanadium oxide microbolometer with a 12 μm pixel pitch, a 640 x 512 array and a thermal sensitivity of 50 mK. The spectral range is 7.5 - 13.5 μm . The size of the camera itself is only 21 x 11 x 11 mm equivalent to a 4.9 cm^3 volume. The camera was equipped with the integrated 24 mm focal length lens and an additional 100 mm focal length planoconvex ZnSe lens was attached to the probe as shown in **Figure 6.2**.

For clinical use, a cap was also printed using biocompatible Dental LT resin which was held in contact with the tooth surface. All parts of the probe with the exception of the Dental LT cap were covered with polypropylene film for infection control as shown in **Figure 6.1B**.

6.3.3 SWIR Dehydration Measurements

Each of the 12 teeth with approximal and occlusal was immersed by hand in a water bath for 30 seconds while being vigorously shaken to enhance water diffusion. After the sample was removed from the water bath, an image was captured as an initial reference image and the air spray was activated. Each measurement consisted of capturing a sequence of images at 1 frame per second for 240 seconds. For each measurement, the air nozzle and the light source were centered on the region of interest (ROI) which encompasses the entire enamel/dentin sample. The dehydration setup was completely automated and image acquisition was carried out using a custom program using LabVIEW™ (National Instruments, Austin, TX).

6.3.4 Thermal Dehydration Measurements

Each of the 16 teeth containing root lesions were removed from the storage solution and placed under the window of the handpiece in contact for thermal capture. The resolution of each captured frame was 293 x 277 pixels. Airflow over the samples was set at 5 psi. Frames were captured at 4 frames per second for a period of 60 seconds. Thermal images acquired at different time points over a period of 60 seconds of drying are shown in **Figure 6.3**. For each thermal dehydration sample, a 5 x 5-pixel lesion area and corresponding 5 x 5-pixel sound area were identified as ROIs. These two areas were tracked over the total duration of time for intensity changes. For each 5 x 5 area, the intensity of all pixels within that area was averaged at each time point.

6.3.5 Analysis of SWIR Intensity-Time Curves

To compare tire dehydration curves between each sample group, the curves were fitted to a sigmoid function, where a-c are coefficients and $I(t)$ is the intensity value at time (t) in seconds. The Levenberg-Marquardt algorithm was used to estimate the best fit of each curve to the equation. The overall growth rate (OGR) of the function was given by a/b (R. C. Lee et al., 2015; R. C. Lee, Staninec, et al., 2016):

$$I(t) = \frac{a}{1 + e^{\frac{(c-t)}{b}}} + d$$

Each curve was fit using Igor Pro from Wavemetrics (Portland, OR) and the OGR was calculated.

6.3.6 Analysis of Thermal Emission Curves

Figure 6.4 provides a flowchart of the steps taken in analyzing the thermal images. Thermal curves were inspected and found to have a sharp dip in intensity, followed by a gradual asymptotic growth to a final intensity level. This behavior corresponds to the evaporation of water, cooling

the surface of the tooth, and then gradual warming back to ambient temperature. To simplify analysis, the curves were split in two at the minimum intensity. The minimum intensity is where the intensity changes from a negative to a positive slope and is representative of the coolest temperature the sample reaches over the experimental time. The corresponding time and intensity at that point are noted as t_{\min} and I_{\min} , respectively (Note: “I” in this instance is not the same as ΔI for SWIR measurements). The maximum intensity, I_{\max} , is the intensity reached after complete thermal drying. These three values are shown on the sample curve in **Figure 6.5**, which is a sample thermal curve of one lesion area of one sample. The intensity values over time after this cutoff were normalized, smoothed using a moving average over 5 time points, and fitted to a three-parameter logistic growth curve. The fit equation is

$$I = \frac{1}{1 + e^{a(t-b)}} + c$$

where “a” is the growth coefficient. It characterizes the growth in intensity over time.

Another important value is integrated intensity. It is a representative measure of heat leaving the tooth at the region of interest. This value can be found by integrating the area of the curve above the intensity versus time graph, but below the maximum intensity reached. The area is represented in **Figure 6.5** as ΔQ .

Contrast was calculated over the 60 seconds of drying and is a measure of the visibility of the lesion against the sound surface. Contrast is calculated by taking the difference in intensities between the sound and lesion ROIs and dividing the result by the intensity of the sound ROI, or

$$\frac{I_S - I_L}{I_S}$$

for each timepoint, where I_S = intensities at sound region, and I_L = intensities at lesion region.

6.3.7 Optical Coherence Tomography (OCT)

An IVS-2000-HR-C OCT system purchased from Santec (Komaki, Aichi, Japan) was used for this study. This system utilizes a swept laser source and a handpiece with a microelectromechanical (MEMS) scanning mirror and the imaging optics. It is capable of acquiring complete tomographic images of a volume of 5 x 5 x 5 mm in approximately 3 seconds. The body of the handpiece is 7 x 18 cm with an imaging tip that is 4 cm long and 1.5 cm across. This system operates at a wavelength of 1312-nm with a bandwidth of 173-nm with a measured resolution in air of 8.8 μm (3 dB). The lateral resolution is 30- μm ($1/e^2$) with a transverse imaging window of 5 mm x 5 mm and a measured imaging depth of 5-mm in air.

6.3.8 Data Analyses

ΔI , growth coefficient, minimum and maximum intensities, ΔQ , and growth start time values were compared between sound and lesion areas using paired t-tests. If $p < 0.05$, then the difference between data was considered significantly different. Tests were carried out using GraphPad Prism 8 (San Diego, CA).

6.4 Results and Discussion

6.4.1 Lesion Activity Assessment by SWIR Dehydration Probe

The 12 teeth imaged with SWIR dehydration probe were divided into four groups based on microCT images of each tooth. The groups were designated as approximal arrested and approximal active; and occlusal arrested and occlusal active. If a highly mineralized surface zone was present on the microCT image of the lesion, the lesion was considered arrested. OCT images were also taken of the arrested lesions confirming that a transparent surface layer was present. If there was no obvious highly mineralized or transparent surface zone present, the lesion was considered active.

SWIR reflectance dehydration measurements for two of the approximal lesions are shown in **Figure 6.6**. The active lesion changes very rapidly and most of the changes occurred in the first 60 seconds of dehydration. Mean dehydration curves for the four lesion groups are shown in **Figure 6.7**. For active lesions the overall intensity change, ΔI , is greater and is more rapid. The OGR was compared between both active and arrested sample groups using a one-tailed t-test, **Figure 6.8**. With $p = 0.036$, the difference in OGR between both active and arrested samples was considered statistically significant.

6.4.2 Lesion Activity Assessment by Thermal Dehydration Probe

A comparison of the images for the 16 root lesions indicated that there were significant differences ($p < 0.05$) for the growth coefficients, minimum intensities, ΔQ and growth start times between sound and lesion areas. However, there was no significant difference for the maximum intensity. There was a significant difference in the thermal response of sound and root lesion areas of human teeth under dehydration at constant airflow. Further *in vitro* studies will be carried out to compare active and arrested root caries lesions. Moreover, we have just completed a clinical study on 30 test subjects in which root caries lesions were imaged *in vivo* using this imaging handpiece along with cross polarization optical coherence tomography (CP-OCT). The thermal imaging appeared to work well *in vivo*, and changes in the thermal emission of the lesions were clearly visible.

6.5 Conclusions

Lesion activity is an important characteristic for determining whether treatment should be given or withheld on a lesion. Histological analyses for lesion assessment such as transverse microradiography (TMR) and polarized light microscopy (PLM) require destruction of the tooth and are not suitable for *in vivo* use. Incorrect diagnosis can result in undertreatment or overtreatment. If a decision to restore is made prematurely when remineralization was feasible,

the patient is committed to a restoration, and often replacement restorations can become progressively larger. If the lesion is active and intervention is delayed, the lesion might require a more invasive and expensive restorative procedure.

This preclinical study demonstrated that a 3D printed appliance with integrated air for SWIR and thermal dehydration can be used to acquire dehydration curves similar to those acquired previously by benchtop imaging systems. Future studies will attempt to discern between active and arrested lesion areas and understand how active lesions respond to treatment *in vivo* under clinically relevant timescales.

6.6 Figures and Figure Legends



Figure 6.1 3D Printed SWIR Imaging Probe

A: The CAD design rendering of the imaging probe body. B: The fully assembled probe with miniature InGaAs array ready for *in vivo* imaging.



Figure 6.2 3D Printed Thermal Imaging Prototype

3D Printed prototype appliance for conducting thermal imaging. The window is centered over the lesion and forced air is delivered through the cylindrical shaped channel to the window.

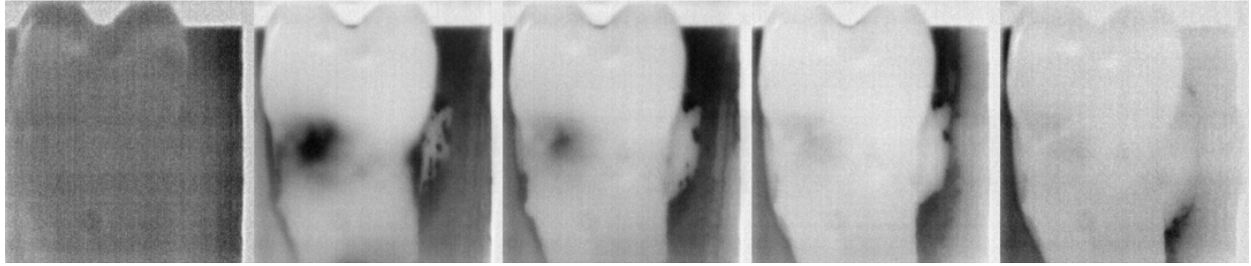


Figure 6.3 Thermal images over time

Thermal images of after 0, 7.5, 15, 30, and 60 seconds of drying elapsed show the behavior of the lesion compared to the corresponding sound surfaces.

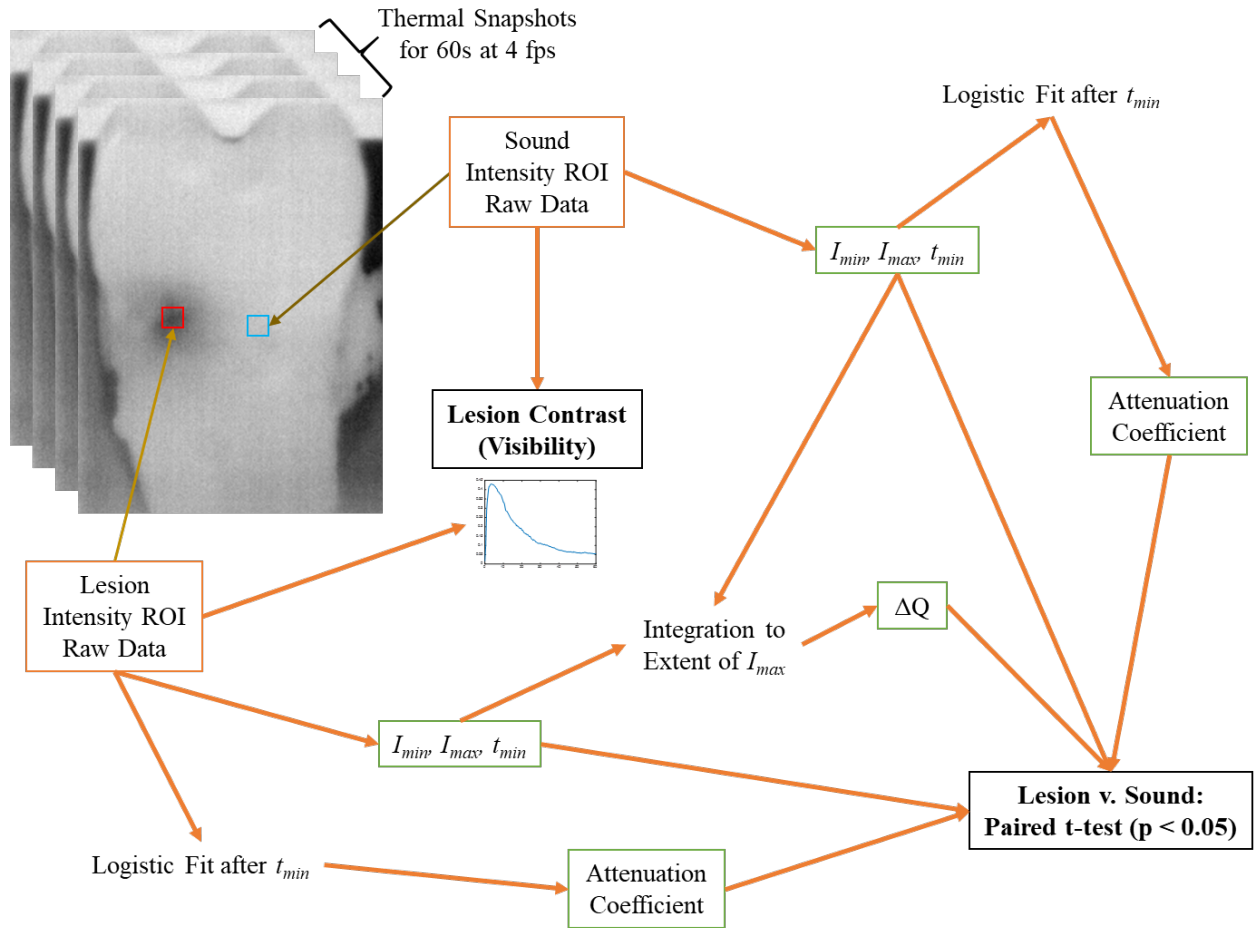


Figure 6.4 Thermal imaging processing steps

Regions of interest (ROI) of 5 x 5 pixels each for sound and lesion areas are designated for each frame at the same location. Lesion contrast is calculated for each corresponding frame. Maximum and minimum intensities (I_{max} , I_{min}) and growth start time (t_{min}) are derived and fitted with logistic regression and referenced to attenuation coefficient, followed by integration with maximum intensity to arrive at ΔQ . ΔQ for lesion and for sound control are compared.

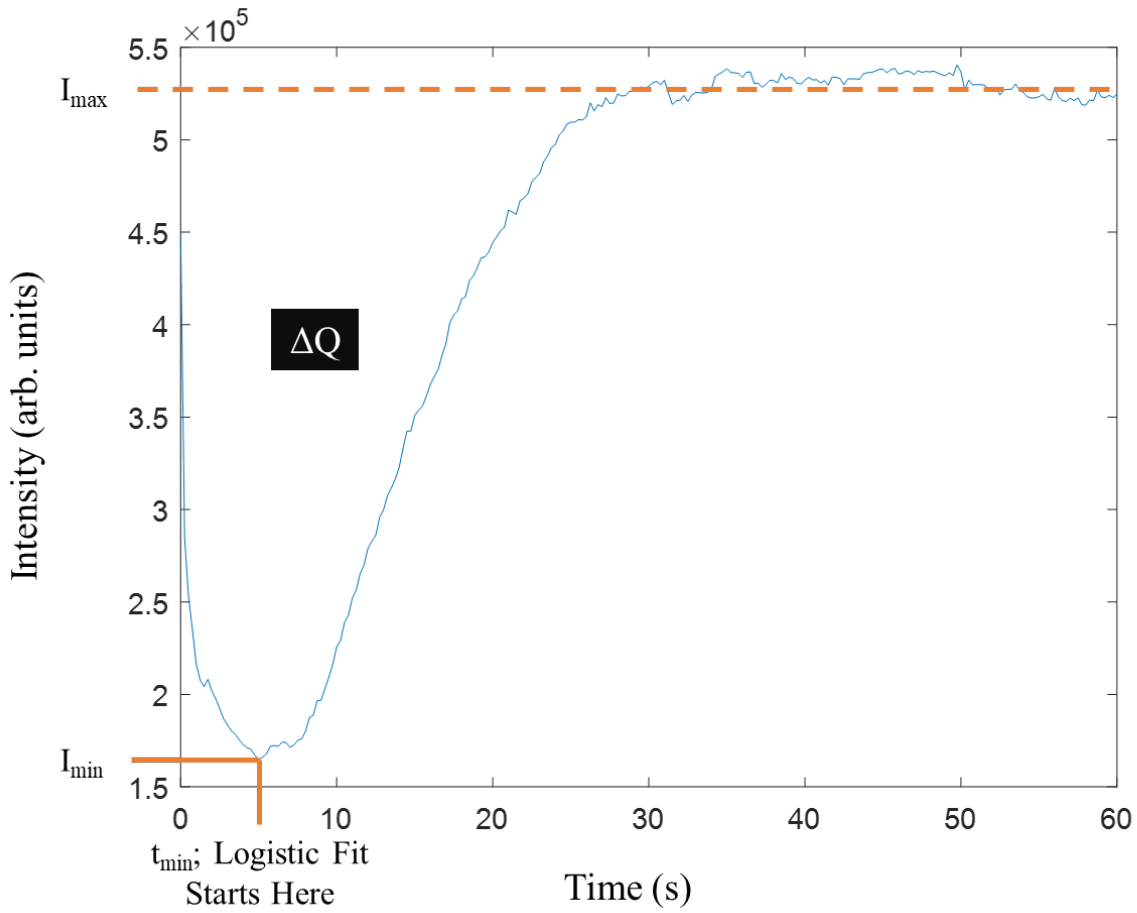


Figure 6.5 Sample thermal dehydration curve plot
 Intensity vs time for the thermal emission showing I_{\min} , I_{\max} , ΔQ and growth start time (t_{\min}).

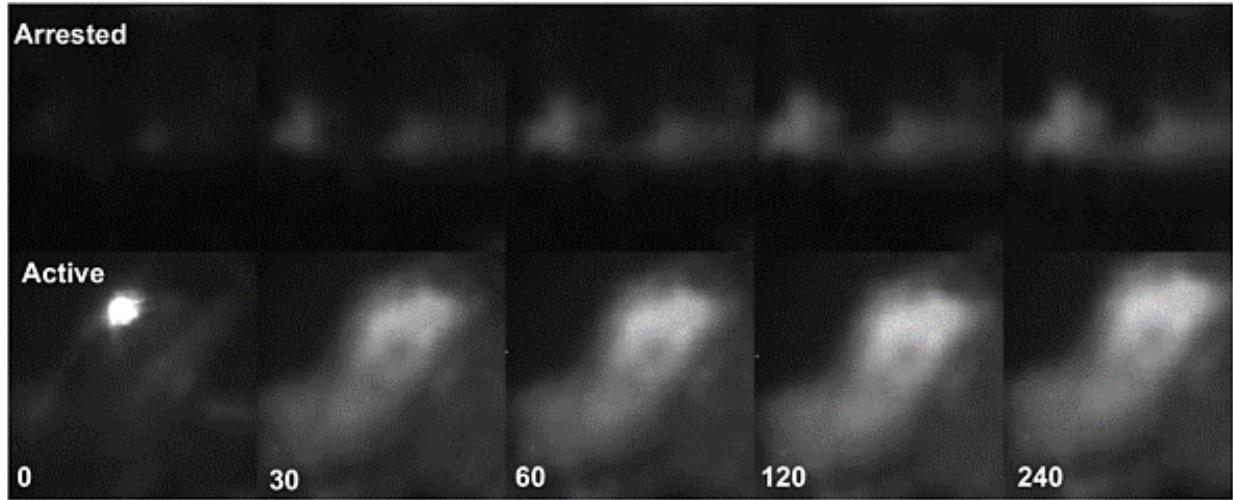


Figure 6.6 SWIR reflectance images throughout dehydration

SWIR reflectance images for active and arrested approximal lesions at time points 0, 30, 60, 120, and 240 seconds after drying elapsed. The intense spot in the active lesion at time point 0 is due to specular reflection of water pooling.

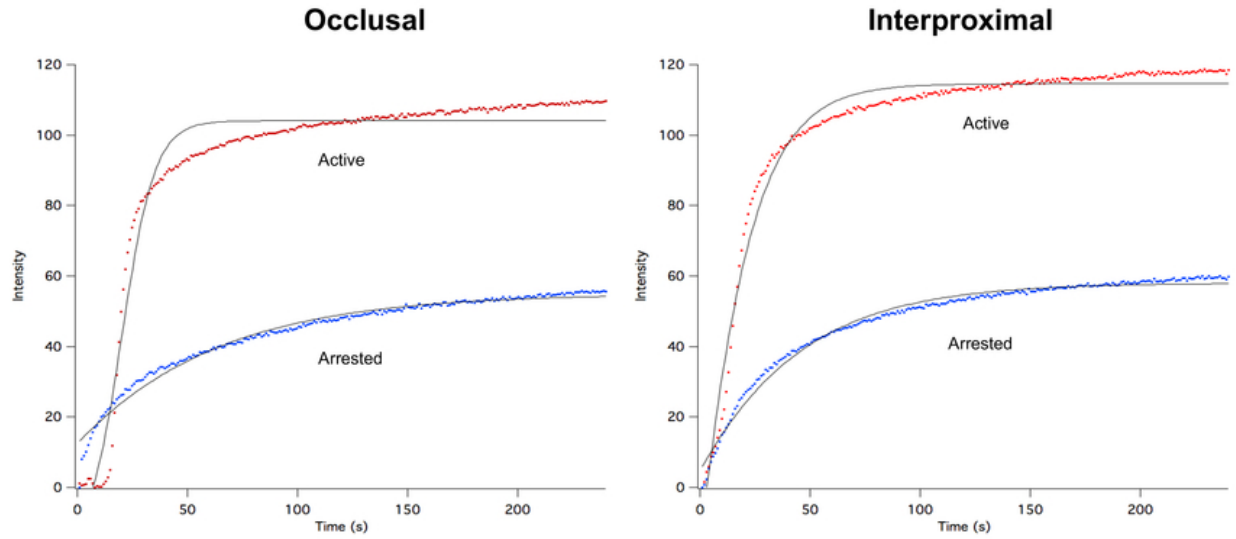


Figure 6.7 Mean SWIR dehydration curves

Mean dehydration curves for occlusal and approximal lesions (n = 3 for each group). Note the differences in curve growth between active vs. arrested lesions.

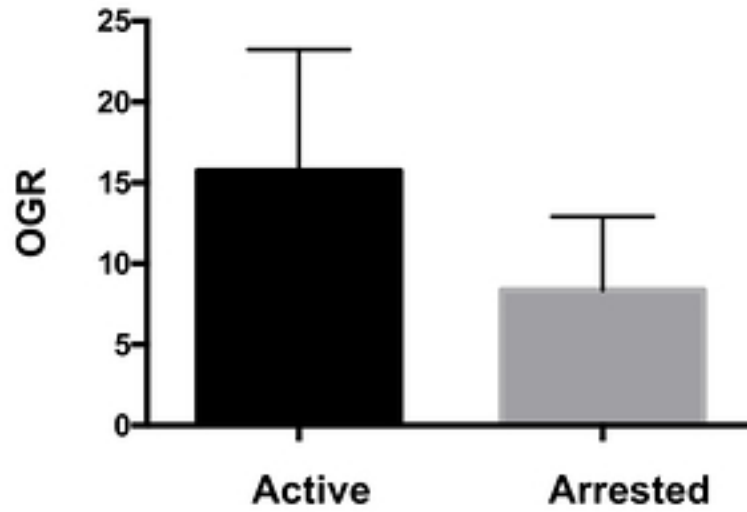


Figure 6.8 OGR between active and arrested lesions

The difference in overall growth rate (OGR) between active and arrested lesions were statistically significant ($p < 0.05$, indicated by different color bar graphs).

CHAPTER VII

SWIR, THERMAL, AND CP-OCT IMAGING PROBES FOR THE *IN VIVO* ASSESSMENT OF THE ACTIVITY OF ROOT CARIES LESIONS

7.1 Summary

New imaging technologies are needed for the clinical assessment of lesions on root surfaces. It is not sufficient to simply detect caries lesions; methods are needed to assess lesion depth, structural composition and activity to determine if chemical intervention has the potential to be effective and if remineralization has occurred. Lesions were monitored using CP-OCT during lesion dehydration to assess the lesion structure and any shrinkage. Thermal imaging at 6-10 μm wavelengths and short wavelength-IR imaging at 1450-1750-nm were used to monitor thermal emission during lesion dehydration to assess lesion activity. Imaging probes were custom fabricated for clinical use. Previous *ex vivo* studies using these imaging probes have shown promise in assessing lesion activities. This presents the first clinical results of a small feasibility study employing CP-OCT, thermal and SWIR imaging to assess lesion activity *in vivo* on thirty test subjects with suspected root caries lesions.

7.2 Introduction

Root caries is an increasing problem with our aging population and likely to be an increasing concern because of an increase in number of people maintaining teeth (B. Dye et al., 2015; B. A. Dye et al., 2007; V. Yang & Fried, 2019). Tooth loss is the most significant oral health-related negative variable of quality of life for the elderly (Saunders & Handelman, 1991). Clinical diagnosis of root caries is highly subjective and is based on visual and tactile parameters. In contrast to coronal caries, root caries lacks a valid diagnostic standard, such as radiography (Banting, 2001). Moreover, early root caries lesions are much more difficult to detect than the early incipient white spot lesions seen with coronal caries. There are often no clinical symptoms with root caries, although pain may be present in advanced lesions. Traditional methods of visual-tactile diagnosis for root caries can result in a correct diagnosis, but not until the lesion is at an advanced stage (Banting, 2001). In addition, investigators have not developed a reliable relationship of appearance with lesion activity (Banting, 1993; Hellyer et al., 1990; Schaeken et al., 1991). Even

though most experts agree that active root lesions are soft, tactile hardness assessments remain subjective and lack reliability (Banting, 1993). Multifactorial root caries scoring systems have been developed with mixed success (Ekstrand et al., 2008; Fejerskov et al., 1991). More recently, the International Caries Detection and Assessment System (ICDAS) coordinating committee and Ekstrand et al. proposed clinical scoring systems for assessing root caries lesion activity (Ekstrand et al., 2008; Ismail, 2005). Criteria include: color (light/dark brown, black); texture (smooth, rough); appearance (shiny or glossy, matte or non-glossy); tactile (soft, leathery, hard); cavitation (loss of anatomical contour); and proximity to the gingival margin (Pitts, 2009). However, such clinical methods for root caries lesion activity assessment lack histological validation and are composed of visual and tactile exams, which are prone to subjective bias and interference from staining (Lynch & Beighton, 1994). Histological analyses for lesion assessment such as transverse microradiography (TMR) and polarized light microscopy (PLM) require destruction of the tooth and are not suitable for use *in vivo*. Incorrect diagnosis can result in under treatment or over treatment.

Several studies have demonstrated that cross-polarized optical coherence tomography (CP-OCT) can be used to quantify changes in the demineralization of enamel and dentin and measure the internal structure and depth of lesions with high-resolution. CP-OCT studies have successfully measured demineralization in simulated caries models in dentin and on root surfaces (cementum) (C. Lee et al., 2009; Manesh et al., 2009a, 2009b). CP-OCT can be used to accurately discriminate demineralized dentin from sound dentin and cementum (C. Lee et al., 2009). CP-OCT has also been used to measure remineralization on dentin surfaces and to detect the formation of a highly mineralized layer on the lesion surface after exposure to a remineralization solution (Manesh et al., 2009a). Cementum has lower reflectivity than dentin in OCT images, making it possible to easily discriminate the remaining cementum thickness (C. Lee et al., 2009; Manesh et al., 2009a). OCT has also been used to help discriminate between non-carious cervical lesions and root caries *in vivo* (Wada et al., 2015). Arrested root caries lesions

typically form an outer layer of highly mineralized dentin that reduces the permeability of the lesion that limits further mineral loss. Furthermore, we have demonstrated the unique ability of CP-OCT to nondestructively determine the thickness of the highly-mineralized transparent surface zone formed on the outside surface of dentinal lesions during remineralization (R. C. Lee et al., 2017; Manesh et al., 2009a, 2009b). Therefore, we postulate that CP-OCT is well suited for detecting structural differences in active and arrested lesions.

Several studies have shown that the unsupported collagen matrix of the demineralized cementum and dentin in active root lesions manifests considerable shrinkage with loss of water (C. Lee et al., 2009; V. Yang & Fried, 2019). OCT is well suited for the accurate measurement of dimensional changes *in vivo*. In a recent study we showed that the shrinkage can also be measured during drying by measuring the contraction of the thickness of the demineralized dentin in addition to the change in the position of the lesion surface (V. Yang & Fried, 2019). We fabricated autoclavable probes with an integrated air-nozzle to fit on the CP-OCT handpiece to measure shrinkage *in vivo* during forced air-drying. CP-OCT can also be used to assess shrinkage, lesion depth, integrated reflectivity over the lesion depth and the transparent surface layer thickness. Therefore, the lesion structure and shrinkage measured with CP-OCT can both be used to assess lesion activity.

Significant changes in surface porosity occurs when a root surface lesion is arrested due to remineralization. Since the heat of water vaporization is large, the use of forced air to evaporate water from dentin pores near the lesion surface induces a large drop in the lesion temperature that can be imaged with a thermal camera. Arrested lesions are less permeable since mineral has filled many of the pores resulting in less water loss leading to smaller temperature changes from forced air-drying. The optical changes associated with water loss have been investigated *in vitro* via thermal, fluorescence, and SWIR imaging for lesions on enamel surfaces (Ando et al., 2012; Kaneko et al., 1999; Usenik et al., 2014). The only clinical study that has been carried out employing optical methods to assess lesion activity via forced air-drying used fluorescence on

smooth surface enamel lesions (Ando et al., 2017). The organic scaffold and dentinal tubules are occupied by mostly water when hydrated (Kinney et al., 1993). The capacity of water retention of dentin increases with the increase in severity of demineralization (Özok et al., 2002). Kaneko et al. and Zakian et al. carried out thermal imaging studies using an infrared camera and an air-jet for evaporation on occlusal and smooth natural tooth enamel surfaces (Kaneko et al., 1999; Zakian et al., 2010) to detect lesions. Lee et al. demonstrated that thermal imaging was highly effective *in vitro* on assessing the activity of simulated and natural lesions on root surfaces (R. C. Lee et al., 2017). Compact and inexpensive high-resolution thermal cameras are now available for intraoral imaging.

Another approach to assessing lesion activity is to use SWIR imaging. Several studies have shown that SWIR imaging at wavelengths from 1450-1750 nm can be used to assess lesion activity on coronal surfaces due to the large change in lesion contrast during drying (R. C. Lee et al., 2015; R. C. Lee, Staninec, et al., 2016). SWIR images can also be used to show high contrast images of calculus and demineralization on root caries lesions on extracted teeth (V. B. Yang et al., 2018). In a recent study, SWIR imaging was effective in assess changes in the activity of simulated lesions on dentin however SWIR imaging was not as effective on natural root caries lesions on extracted teeth (R. C. Lee et al., 2017).

In this study, thirty test subjects with at least one suspected active root caries lesion were imaged with CP-OCT and SWIR and thermal imaging. Drying the lesions with air for thirty seconds was used to assess the potential of these three novel approaches for assessing the activity of lesions on root surfaces *in vivo*.

7.3 Materials and Methods

7.3.1 Participant Recruitment and Procedures

Thirty test subjects at the UCSF Comprehensive Dental Clinics were recruited for this study (UCSF IRB 18-24558). The test subjects' age range was 18-90 years old. Each test subject had

at least one root caries lesion that was accessible to imaging and was determined to be active based on conventional assessment by clinicians. Each lesion was imaged with a cross-polarized USB visible camera with a dental mirror, and the color, texture (roughness), and softness were assessed. Two 3D cross-polarization OCT images of the lesion were acquired while it was wet and after it had been dried for 30 seconds with pressured air at 10 psi. In addition, a 2D OCT image (b-scan) was recorded while the lesion was dried for 30 seconds. The lesion was wetted, and thermal images were recorded for 30 seconds during drying. Images were also acquired using SWIR imaging at 1450-1750 nm as the lesion was dried for 30 seconds.

7.3.2 SWIR Reflectance (1450-1750 nm) Dehydration Handpiece

A highly sensitivity, InGaAs, micro-SWIR camera (SU640CSX) measuring only 32 x 32 x 28 mm from Sensors Unlimited (Princeton, NJ), with a 640 x 512-pixel focal plane array and 12.5- μ m pixel pitch was used to capture SWIR images from 1450-1750 nm. A SLS201L Stabilized Tungsten-Halogen lamp from Thorlabs (Newton, NJ) with a 1450 nm long-pass filter and a 1 mm in diameter low-OH optical fiber was used as the light source for reflectance. A lens assembly consisting of 1 inch in diameter $f = 75$ - and 60-mm lenses along with an adjustable aperture was attached to a 3D printed handpiece equipped with a 10 mm aluminium mirror with channels for air and the 1-mm optical fiber. The distal end of the 1-mm fiber was inserted into a Teflon plug to provide diffuse illumination. Air at 10 psi was connected to the probe as shown in **Figure 7.1** to prevent fogging of the handpiece window and to facilitate dehydration of the lesion.

The handpiece body was printed with standard black resin from Formlabs (Somerville, MA) using Form 2 and 3 printers. A cap was also printed using biocompatible Dental LT resin which was held in contact with the tooth surface. All parts of the probe with the exception of the Dental LT cap were covered with polypropylene film for infection control as shown in **Figure 7.1**. Image acquisition was carried out using a custom program using LabVIEW™ from National Instruments (Austin, TX) (W. A. Fried et al., 2020).

7.3.3 Thermal Imaging Dehydration Handpiece

Thermal images were captured using a FLIR Boson 640 (Wilsonville, Oregon) thermal camera that employs an uncooled vanadium oxide microbolometer with a 12- μm pixel pitch, a 640 \times 512 array, a thermal sensitivity of 50 mK, and a bit depth of 14 bits (**Figure 7.1**). The spectral range is 7.5 to 13.5 μm . The size of the camera itself is only 21 \times 11 \times 11 mm, equivalent to a 4.9 cm^3 volume. The camera was equipped with an integrated 24-mm focal length lens. An additional 100-mm focal length was attached to a handpiece that was 3D printed using autoclavable Dental-SG resin (**Figure 7.1**). A 12.5-mm polished aluminum plane surface was attached at the distal end so the handpiece could be held in contact with the tooth surface at a right angle to minimize motion during dehydration. Thermal emission from the tooth surface at a distance of 8 cm from the second lens was focused onto the camera array. An air nozzle was attached to the handpiece to provide focused air to dry the lesion area at 5 to 10 psi. Raw images of the intensity were recorded at 4 Hz for 30 seconds using a program custom written with LabVIEW from National Instruments and imported into MATLAB for further analysis. Lesions were wetted with a cotton swab before each measurement. Intensity profiles versus time were extracted from the mean intensity of a 5 \times 5-pixel region of interest (ROI) manually selected and designated as sound, active, or arrested based on the presence of demineralization in the corresponding CP-OCT images with (arrested) or without (active) a transparent surface zone. Integration of the thermal profiles from 0 to 30 s yielded the change in heat or overall thermal emission, ΔQ (V. B. Yang et al., 2020). A larger ΔQ represents a greater loss of heat during drying or less thermal emission. Statistical comparisons between ΔQ for sound and suspected active and arrested lesion areas were performed in GraphPad Prism 8 (GraphPad Software).

7.3.4 Cross Polarization Optical Coherence Tomography (CP-OCT)

The cross-polarization OCT system used for this study was purchased from Santec (Komaki, Aichi, Japan). This system acquires only the cross-polarization image (CP-OCT), not both the

cross and co-polarization images (PS-OCT). The Model IVS-3000-CP utilizes a swept laser source; Santec Model HSL-200-30 operating with a 30 kHz a-scan sweep rate. The Mac-Zehnder interferometer is integrated into the handpiece which also contains the microelectromechanical (MEMS) scanning mirror and the imaging optics. It is capable of acquiring complete tomographic images of a volume of 6 x 6 x 7 mm in approximately 3 seconds. The body of the handpiece is 7 x 18 cm with an imaging tip that is 4 cm long and 1.5 cm across. The lateral resolution is 80- μm ($1/e^2$) with a transverse imaging window of 6 mm x 6 mm and a measured imaging depth of 7-mm in air. The polarization extinction ratio was measured to be 32 dB. This system operates at a wavelength of 1321-nm with a bandwidth of 111-nm with a measured resolution in air of 11.4 μm (3 dB). This system has been used for multiple *in vivo* caries imaging studies (Chan et al., 2016; Nee et al., 2014; Simon et al., 2017).

An appliance made of Dental-LT resin printed using a Formlabs 3D printer was attached to the OCT scanning handpiece (V. B. Yang & Fried, 2019). Air at 10 psi was connected to the probe to prevent fogging of the mirror and to facilitate dehydration of the lesion. the handpiece was covered with polyethylene film for infection control as shown in **Figure 7.1**. Images were captured before and after drying and imported into MATLAB (MathWorks) for analysis. Entire (3D) CP-OCT cross-polarization images of each lesion were acquired before and after drying with air. In addition, continuous CP-OCT 2-dimensional (2D) images were recorded for 30 s during drying to assess shrinkage. In order to match the surface position and transparent surface zone thickness, image processing was applied to the images as described previously for *in vitro* studies (R. C. Lee et al., 2014; V. Yang & Fried, 2019). For each, a 3D Gaussian filter was applied ($\sigma = 4$), followed by 3D Canny edge detection at a low threshold to resolve the surface of the tooth with minimal surface breaks.

7.4 Results and Discussion

In this study, thirty root caries lesions were imaged on thirty test subjects. This was the first time an appliance was attached to the OCT scanner to provide dehydration of the lesion, and it worked well. The air also prevented condensation on the OCT window which had been a problem in past OCT imaging studies in which we had to have an assistant to provide air at imaging window during imaging via the air-water syringe of the dental chair unit. There were some considerable difficulties holding the handpiece steadily during imaging, which will need to be investigated whether lesion shrinkage during lesion dehydration could be shown successfully. We were able to acquire high quality OCT images of the root caries lesions, resolve the transparent surface zones that were present and see visible changes in the root caries lesions during dehydration.

Two OCT b-scans acquired from two of the lesions are shown in **Figure 7.2**. A transparent surface zone was visible on one of the lesions which suggests that the area of that lesion is likely arrested. In contrast, there is no surface zone visible near the surface in the CP-OCT b-scan of the other lesion that is shown in **Figure 7.2** and on most of the other lesions imaged during the study.

Originally, there was no intention to include SWIR imaging during dehydration since the method was not as effective for natural root caries lesions on extracted teeth as it was for simulated lesions on dentin. In this preliminary assessment of its performance, it appeared to be effective for only a few lesions and dehydration for 30 seconds did not appear sufficient to dehydrate most lesions.

To the best of our knowledge, this was the first clinical study involving the thermal imaging of caries lesions *in vivo* and this method appears to show great potential. Most of the lesions were visible in the thermal images and the time course of the thermal emission from the lesion area during dehydration was distinctly different from the sound regions of the tooth. Matching color and thermal images are shown in **Figure 7.3** for two of the lesions that are shown in the CP-OCT

scans of **Figure 7.2**. The lesion in the top images appeared arrested in the CP-OCT scans with a surface layer visible; the lesion at the bottom images appeared active.

There were some initial complications. Data for 5 of the test subjects were discarded due to the inability to acquire suitable thermal images for analysis that included fogging of the sensor windows, equipment malfunction, or insufficient air pressure during the first 4 test subjects. After the first 4 test subjects, we determined that an air pressure of 5 psi was insufficient and that variations in humidity during breathing interfered with the measurements. Subsequently, we increased the air pressure to 10 psi, and the fluctuations due to breathing no longer interfered with the thermal images.

Color, thermal, and OCT images of a test subject lesion are shown in **Figure 7.4**. This is a shallow lesion that is brown, rough, and soft that is located just at the cementum-enamel junction (CEJ). This active lesion is of particular interest as one of the only samples that has a large area of sound-exposed root surface located below the lesion for comparison. Thermal images at different time intervals are shown in **Figure 7.4B**. After 1 second of drying, the area of exposed dentin and the lesion appear much darker than the enamel above the lesion. After 5 s, the cooler/darker area is localized to the lesion, and after 15 s, the temperature over most of the tooth surface has equilibrated. A plot of the thermal emission intensity from areas of sound enamel (E), active lesion (L), and sound dentin (D) after 30 s of drying is shown in **Figure 7.4D**. In areas of the lesion, the temperature drop is of a much greater magnitude and is of a longer duration than other areas of the tooth. A CP-OCT b-scan taken along the path of the black arrow with the position of the 3 colored markers indicated is shown in **Figure 7.4C**. The lesion appears as the brighter area (red circle) just below the position of the CEJ due to the higher reflectivity of the demineralized dentin. The position of the CEJ can be visualized by following the intersection of the tooth surface and the dentinal-enamel junction (DEJ), which is visible below the tooth surface. The OCT scan also shows that the cementum has been lost from the root surface and that a small

section of enamel has broken off near the CEJ. No transparent surface zone indicative of an arrested lesion is visible on this lesion in the CP-OCT scan.

Another lesion that has 2 distinct zones is shown in **Figure 7.5**. The upper zone closer to the enamel appears darker and rougher than the lower zone in the color image. The lower zone (R) appears to have a distinct surface zone in the CP-OCT image and appears less active in the thermal images. Extracted thermal images are shown in Figure 3B. The lower “remineralized” (R) zone shows intermediate behavior between the sound and more “active” (A) lesion area, and we suspect that this area is arrested. After 30 s of air drying, the most severe/active area of the lesion appears as a dark band centered on the upper zone of the root caries lesion. Thermal profiles shown in **Figure 7.5D** were taken at the 3 positions identified as sound (S), upper lesion (A), and lower lesion (R). Thermal emission is lower (darker) from the upper lesion area than from the lower lesion area, suggesting that it is more active. The cooler area (A) has not recovered after 30 seconds, indicating that more drying time would be needed to completely dehydrate this highly porous lesion area. The CP-OCT b-scan image shown in **Figure 7.5C** shows that there is no surface zone visible in the upper lesion area while the lower lesion area shows a distinct surface layer (orange dotted arrow) that is more than 100 μm thick. It appears that a large section of the overlying enamel has broken off and exposed the more active upper lesion area.

Useful thermal images were acquired for 25 of the 30 lesions, and ΔQ was calculated for the most demineralized part of the lesion and an adjacent sound area. A comparison of ΔQ between sound tooth structure and active lesion areas using a paired *t* test for the 25 lesions showed a statistically significant difference, with a mean \pm SD in relative intensity units of 4.8 ± 4.6 and 18.1 ± 5.7 ($p < 0.0001$). Ten of the lesions had areas with measurable surface zones in the CP-OCT images similar to the lesion shown in **Figure 7.5**, suggesting that those areas were arrested. Transparent surface zone thicknesses in these arrested regions ranged from 62 to 140 μm , with a mean \pm SD thickness of 98 ± 26 μm . ΔQ was calculated for the thermal profiles in those suspected arrested areas and compared with the sound and suspected active areas on

those teeth. Repeated-measures analysis of variance indicated that the 3 groups were significantly different, with a mean \pm SD of 5.9 ± 5.6 , 13.0 ± 6.4 , and 21.4 ± 5.9 for sound, arrested, and active lesion areas, respectively ($p < 0.0001$). The comparisons are shown graphically in **Figure 7.6**.

The exact surface positions of the CP-OCT scans could be co-registered before and after drying for only 12 of the lesions. The mean shrinkage was $61 \pm 54 \mu\text{m}$ for those 12 samples. Surface zones were visible for 3 of those 12 lesions, suggesting they were arrested. The mean shrinkage for those lesions with surface zones ($n = 3$) was significantly less than the lesions without surface zones ($n = 9$), $7.7 \pm 6.7 \mu\text{m}$ versus $78 \pm 51 \mu\text{m}$ ($p < 0.003$).

All the lesions were classified as active lesions based on clinical assessment and the multiple ICDAS II lesion activity criteria. Thirteen of the lesions were colored brown, 16 black, and 1 gray; 28 were rough and 2 were smooth; and 27 were scored soft and 3 were leathery. Ten lesions in the study appeared to have both active and arrested areas (see Fig. 3) based on the CP-OCT and thermal data. The clinical assessment was for the lesion as a whole, and therefore it is not appropriate to compare the clinical assessments with the thermal and CP-OCT shrinkage data that are for specific areas of a lesion. Only 5 of the lesions had a clinical description that would indicate the possibility of an arrested lesion. None of the lesions were clinically designated as shiny or hard, and only 3 were designated as leathery and 2 as smooth. Out of the 10 lesions that had areas with surface zones, 1 appeared smooth and another was leathery.

7.5 Conclusions

The presence of the highly mineralized transparent surface zone was used as the hallmark for an arrested lesion surface with the caveat that this is not a gold standard. Although the validity of this approach is supported by good agreement of histopathology and CP-OCT images for in vitro studies, transparent surface zones are not yet a gold standard to identify an arrested surface. Before the introduction of optical coherence tomography, a tooth had to be extracted, sectioned,

and imaged with transverse microradiography to detect a transparent surface zone. Even though the presence of a highly mineralized outer layer at the surface of the lesion appears to be the best indicator that a lesion is arrested, it is unclear how thick or how highly mineralized that layer must be for it to be clinically inactive and to remain so with acid assaults.

CP-OCT can be used to detect the transparent surface zone that is indicative of arrested lesions in vivo. The use of CP-OCT to measure lesion shrinkage during drying was only partially successful since we were only able to co-register CP-OCT images for 12 of the lesions before and after drying due to movement during imaging. In future studies, a method will need to be developed to prevent movement during drying. However, the mean shrinkage for those 12 samples in which the surface position could be matched before and after drying was more than 60 μm , which can be easily measured with OCT.

In summary, based on the initial results of this pilot clinical study, thermal and CP-OCT imaging appear highly promising for the clinical assessment of lesion activity on root surfaces. We have demonstrated that thermal and CP-OCT imaging have great potential for the in vivo assessment of the activity of root caries lesions in a single appointment. Future efforts will be to evaluate if these imaging methods can be used to monitor remineralization efforts over time.

7.6 Figures and Figure Legends

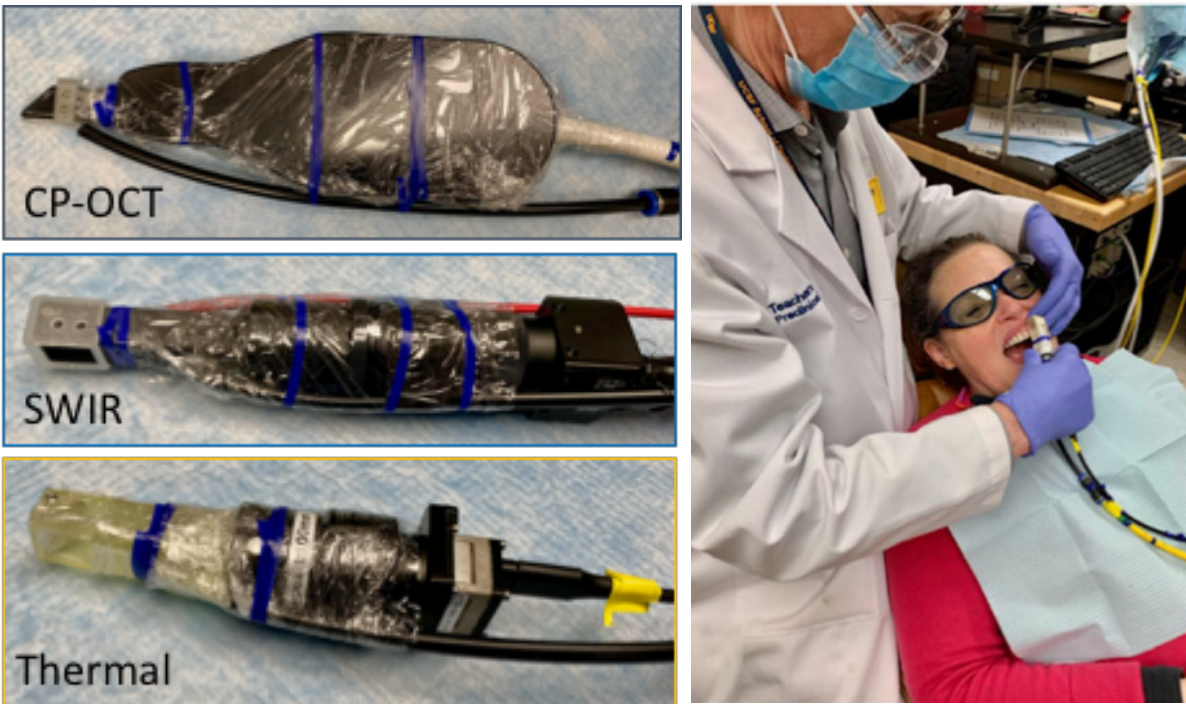


Figure 7.1 Imaging Probes Used

Left: The three 3D printed imaging probes used to image each of the root caries lesions. The SWIR and thermal probes have 3D printed autoclavable attachment with an air channel to focus air across the tooth surface and a right-angle aluminum mirror. These are attached to an additional lens and small respective sensor and camera. *Right:* A photo of the handpiece being used clinically.

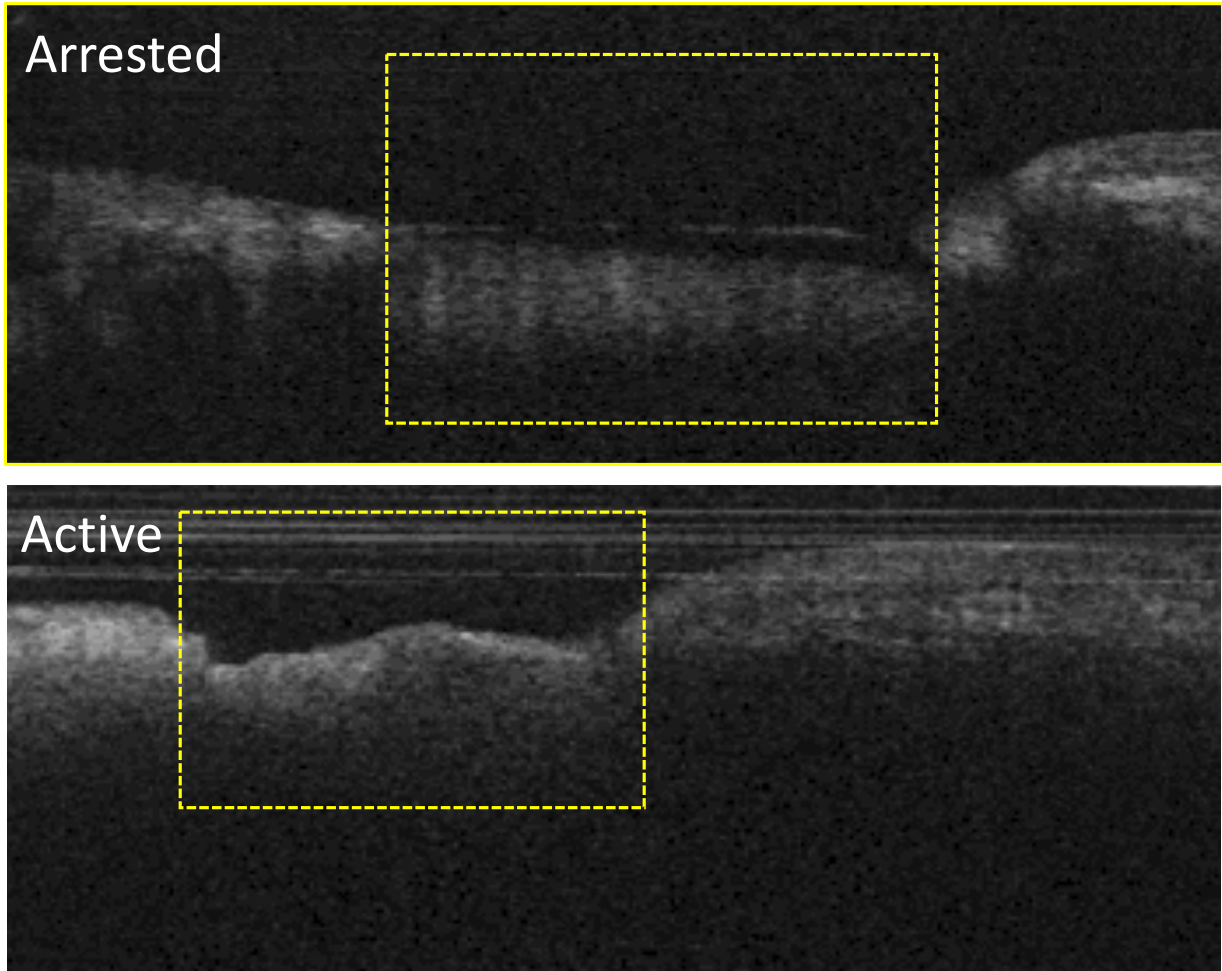


Figure 7.2 Two CP-OCT b-scans of root caries lesions

“Arrested” root caries lesion with transparent surface zones visible at the surface of the lesions.
“Active” lesion does not have the transparent surface zones. Lesions are in yellow boxes.

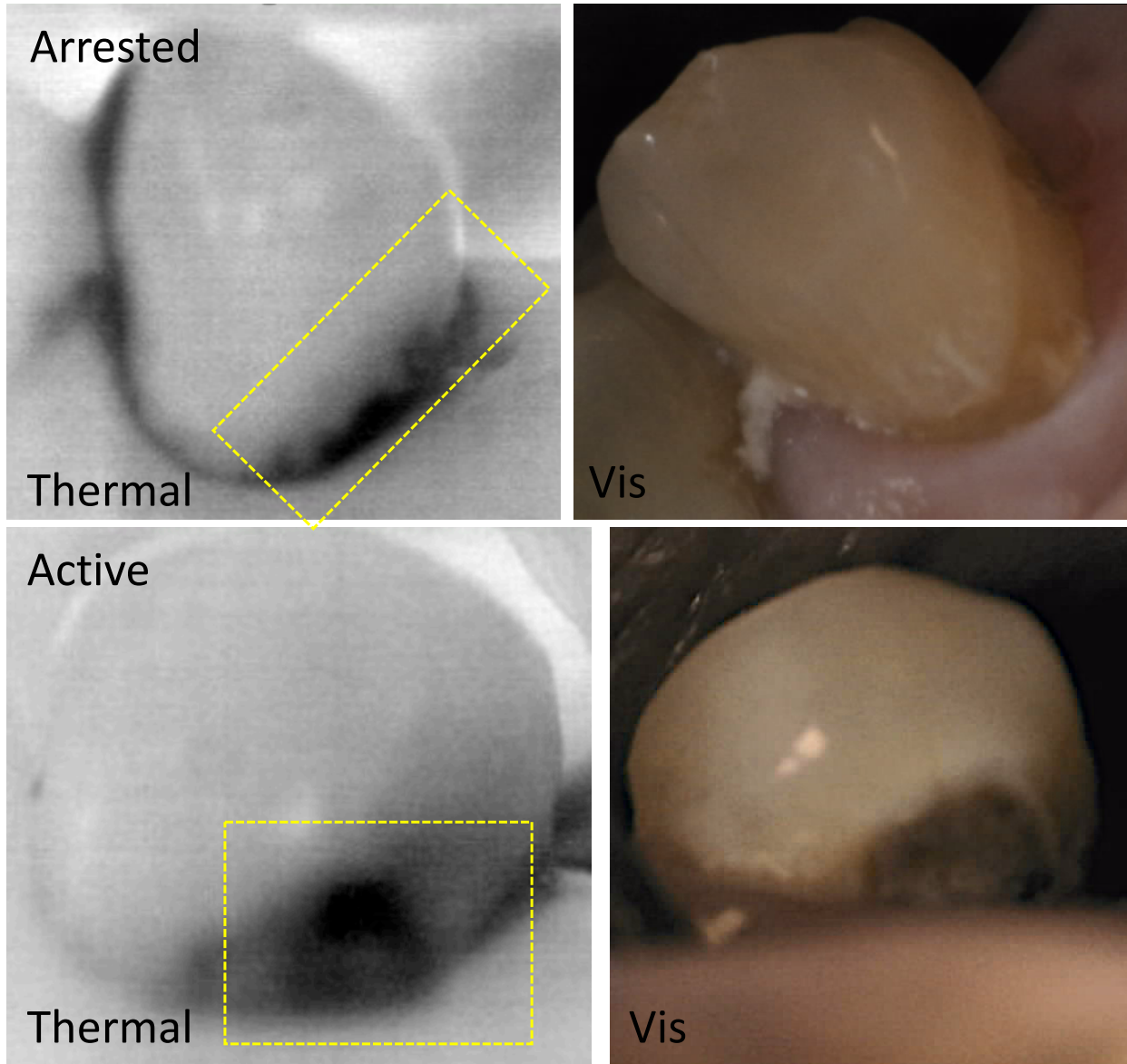


Figure 7.3 Two thermal and visible images of root caries lesions

Same lesions as depicted in Fig. 7.2. “Arrested” root caries lesion with transparent surface zones visible at the surface of the lesions. “Active” lesion does not have the transparent surface zones. Lesions are in yellow boxes.

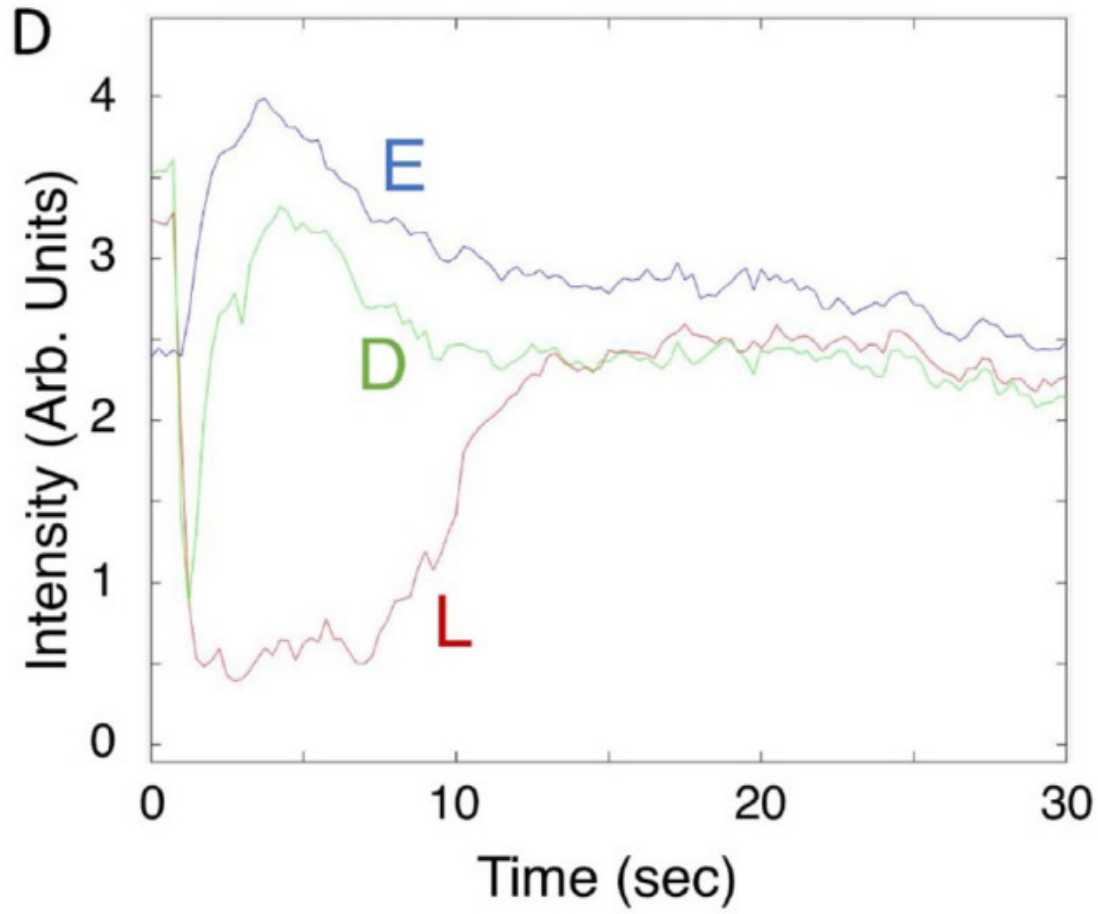
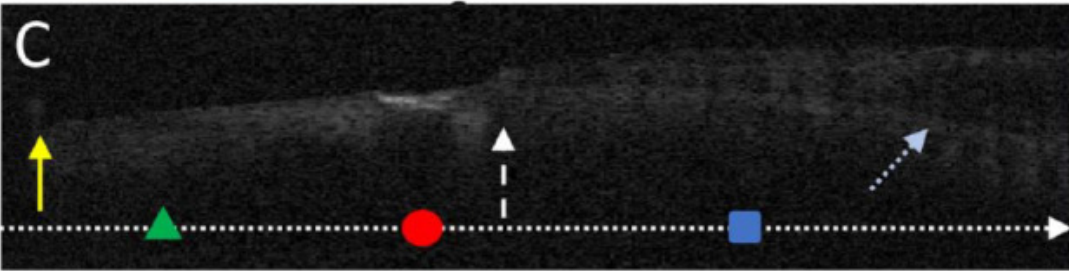
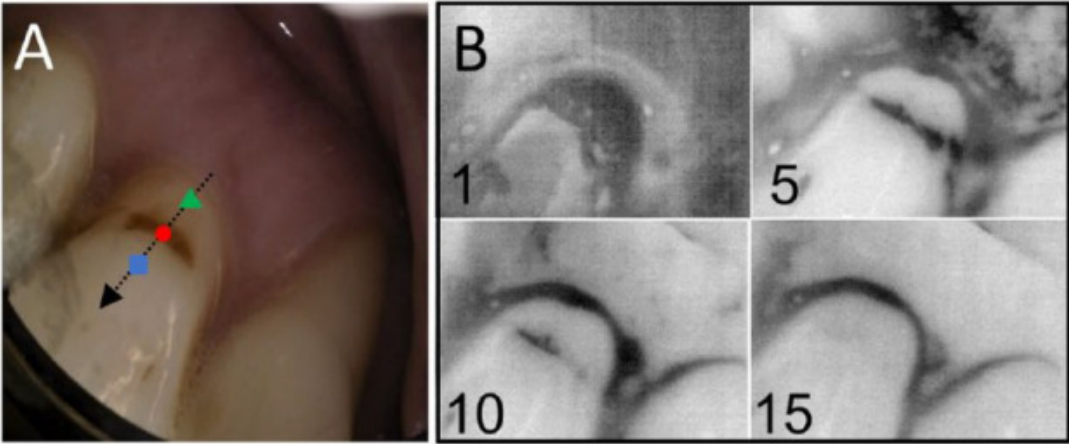


Figure 7.4 Visible, thermal, and CP-OCT images of a shallow active root lesion

Images of a root lesion with a large area of exposed sound dentin. *A*: Color image of the tooth; *B*: Four thermal images extracted at 1-, 5-, 10-, and 15-s time intervals during drying are shown. *C*: the black arrow shows the path of the CP-OCT image, and the colored markers show the respective positions of the *D*: thermal emission profiles, where the green triangle is in the area of sound-exposed dentin (*D*), the red circle is in the active lesion area (*L*), and the blue square is in sound enamel (*E*). Intensity increases from black to white in the grayscale false color images for both the CP-OCT and thermal images. A CP-OCT scan was taken at the position of the arrow in *A* with the position of the 3 markers on the arrow. The white dashed arrow points to the position of the cementum-enamel junction (CEJ), the yellow solid arrow the gingiva, and the light blue dotted arrow the dentinal-enamel junction (DEJ). The DEJ can be seen clearly in the image as the lower line beneath the surface on the right side of the image. Some of the enamel has broken off near the CEJ, and the cementum layer has been worn away. The lesion is visible as a bright region at the position of the red circle. The dimensions of the CP-OCT image are 2 mm depth (y-axis) and 6-mm lateral position (x-axis). The thermal emission from the tooth surface during drying is shown for the 3 positions indicated.

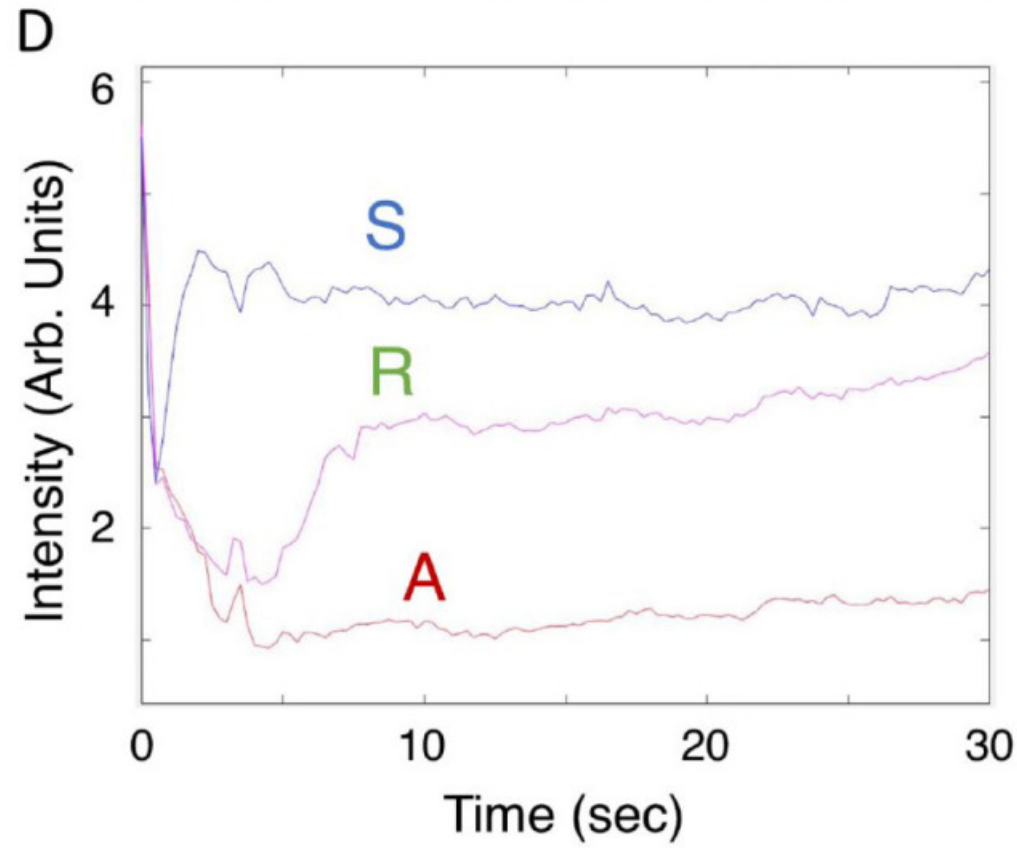
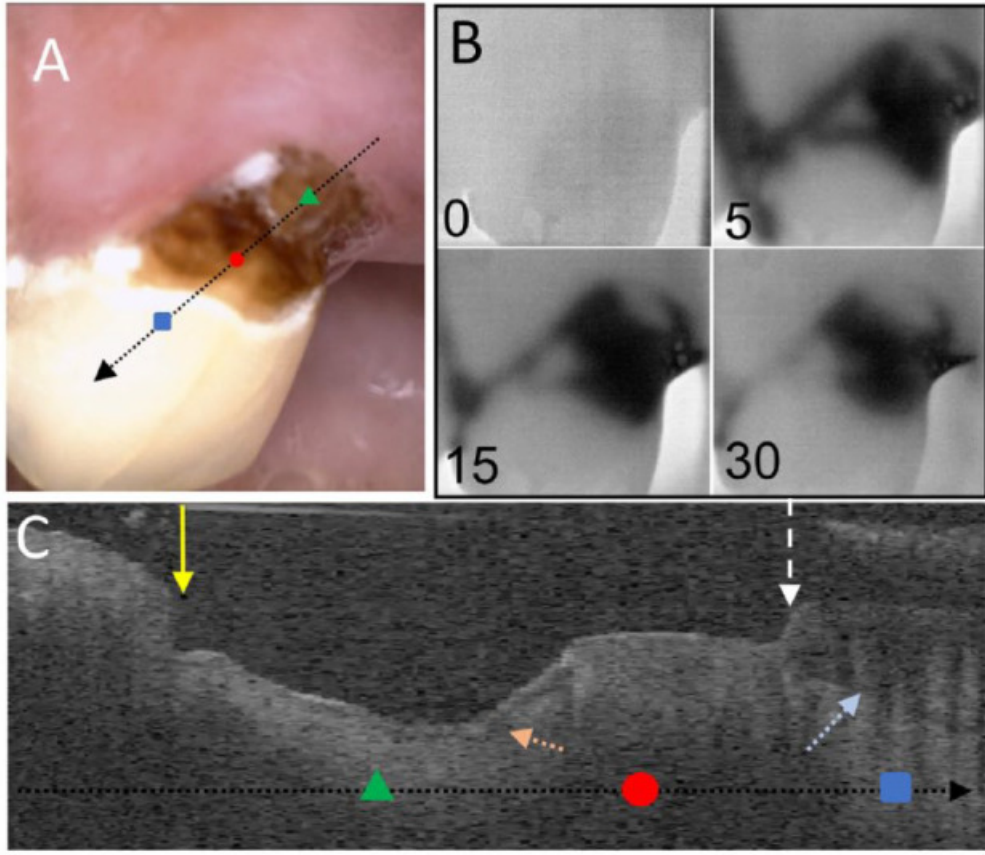


Figure 7.5 Visible, thermal, and CP-OCT images of a large root lesion with both active and arrested areas

The lower half of the lesion appears distinctly lighter and glossy in the visible image, and the CP-OCT image shows that a transparent surface zone is present on that part of the lesion, suggesting that it is arrested. *A*: Color image of the tooth; *B*: Four thermal images extracted at 0-, 5-, 15-, and 30-s time intervals during drying are shown. *C*: the arrow shows the path of the CP-OCT image, and the colored markers show the respective positions of the *D*: thermal emission profiles, where the green triangle is in the arrested lesion area (R), the red circle is in the active lesion area (A), and the blue square is in a sound area (S). A CP-OCT scan is shown, taken at the position of the arrow in *A*, with the position of the 3 dots marked on the arrow. The white dashed arrow points to the position of the cementum-enamel junction (CEJ), the yellow solid arrow the gingiva, and the light blue dotted arrow the dentinal-enamel junction (DEJ). A large part of the enamel has broken off near the CEJ, and there is significant loss of cementum and dentin. A distinct surface zone is visible (orange dotted arrow) on the lower portion of the lesion. The dimensions of the CP-OCT image are 2 mm (axial depth in air) and 6 mm lateral position. The thermal emission from the tooth surface during drying is shown for the 3 positions indicated.

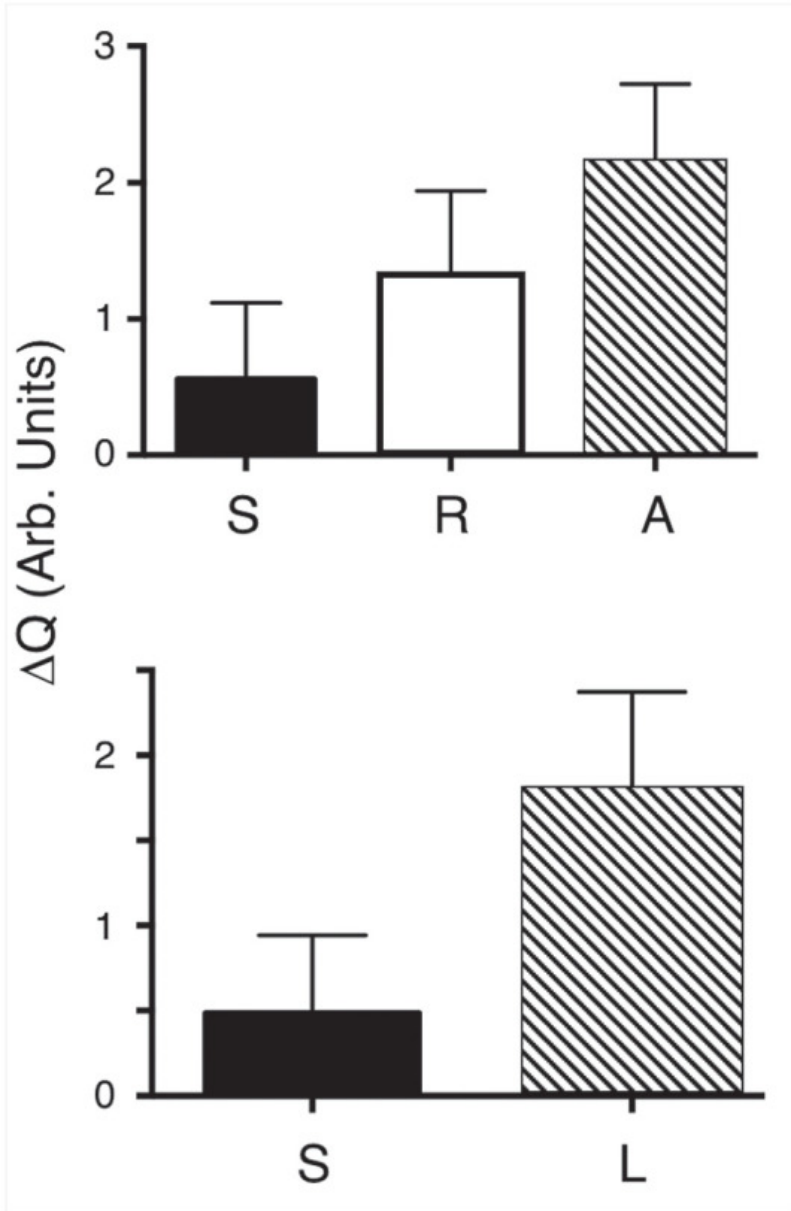


Figure 7.6 Comparisons of ΔQ for different lesion zones

Top: The mean \pm SD of ΔQ for the $n = 10$ samples for regions that had sound (S), active (A), and arrested (R) lesion zones. All groups are significantly different, $p < 0.001$. *Bottom:* The mean \pm SD of ΔQ for lesion (L) and sound (S) areas for all 25 of the teeth that yielded acceptable thermal images. All groups are significantly different, $p < 0.0001$.

CHAPTER VIII

SUMMARY AND FUTURE PERSPECTIVE

8.1 Summary

The overall objective of this dissertation work is to develop infrared methods for the clinical assessment of lesion structure and activity. Improved imaging technologies employing non-ionizing radiation will significantly improve caries diagnosis and management. It is not sufficient to simply detect carious lesions, methods are needed to assess the lesion activity and depth to determine if chemical intervention is a viable option. There are structural differences between active lesions and arrested lesions, and these differences can be quantified using infrared imaging methods. A transparent highly mineralized outer surface zone is formed due to remineralization on the top of arrested lesions, which leads to decreased permeability to fluids including water and plaque generated acids. Before the introduction of optical coherence tomography, a tooth had to be extracted, sectioned, and imaged with transverse microradiography to detect the transparent surface layer. Histological analyses for lesion assessment such as transverse microradiography (TMR) and polarized light microscopy (PLM) require destruction of the tooth and are not suitable for *in vivo* use. Lesion activity is an important characteristic for determining whether treatment should be given or withheld on a lesion. Incorrect diagnosis can result in undertreatment or overtreatment. If a decision to restore is made prematurely when remineralization is still feasible, the patient is committed to a restoration, and often replacement restorations can become progressively larger. If the lesion is active and intervention is delayed, the lesion might require a more invasive and expensive restorative procedure.

Previous studies have shown that the thickness of this transparent surface layer can be measured nondestructively using optical coherence tomography (OCT) and have demonstrated that SWIR reflectance and thermal imaging coupled with dehydration can be used to measure changes in the permeability of lesions in enamel and dentin (N.-Y. N. Chang et al., 2018, 2019; Jones et al., 2006; Jones & Fried, 2006; Kang et al., 2012; R. C. Lee et al., 2014; Mandurah et al., 2013). Even though the presence of a highly mineralized outer layer at the surface of the lesion appears to be the best indicator that a lesion is arrested, it is unclear how thick or how

highly mineralized that layer must be for it to be clinically inactive. Utilizing *in vitro* bench top infrared imaging methods, studies conducted in this body of work have developed methods for *ex vivo* assessments of lesion severity and activity. Incorporating modern imaging and 3D CAD design and printing technologies, methods for clinical assessments of lesion activity *in vivo* were developed and tested. These studies have increased our understanding of the structural changes occurred to arrest active lesions and provide methods for assessing the activity of lesions in a single examination to avoid unnecessary treatment and cavity preparations.

8.2.1 *In Vitro* Lesion Activity Assessments

In **Chapter 2**, SWIR dehydration was used to assess the activity of simulated bovine enamel lesions. The results were also compared with the transparent surface layer thickness generated by simulated remineralization as measured by OCT. The results suggest that the permeability decreased with increasing transparent surface layer thickness. A small increase in transparent surface layer thickness of <20 μm lead to large permeability changes, indicating a potentially consistent characteristic of arrested lesions.

The study conducted in **Chapter 3** helped further define the relationship between transparent surface layer thickness and permeability measurement by analyzing serial SWIR dehydration permeability measurements of simulated lesions following different durations of exposure to remineralization solutions. SWIR permeability measurements and OCT imaging of simulated lesions subjected to different days of remineralization were compared. The greatest changes to permeability were seen after 18 days of remineralization, and the greatest changes to integrated reflectivity occurred after 12 days. This indicates that remineralization for inhibiting active lesions towards becoming arrested lesions do not follow a linear profile over time. However, no further changes to the simulated enamel lesions were seen by SWIR permeability measurement and OCT imaging after 32 days of exposure to the remineralization solution.

8.2.2 Ex Vivo Lesion Activity Assessments

Based on the conclusions from *in vitro* studies, *ex vivo* assessments of lesion activity on extracted teeth were the logical next step for further evaluation of infrared methods for lesion activity assessment. The highly mineralized transparent surface layer also plays an integral role in arresting natural lesions. SWIR reflectance permeability measurements of surface lesions on extracted teeth appears to negatively correlate with the thickness of the transparent surface layer determined by OCT imaging. The correlation remains non-linear, but significantly negative. The results indicate that at thicknesses greater than 50 μm , the permeability of the lesions is significantly lower than lesions with transparent surface layers thinner than 50 μm . Permeability seems to no longer change when transparent layer thicknesses exceed 70 μm . This further provides evidence that SWIR reflectance permeability measurement may be an effective clinical method for assessing surface lesion activity.

The prevalent use of tooth-matched and radiopaque composites for restoring primary decay in clinical dentistry has led to a dramatic increase in the number of secondary caries due to a multitude of clinical placement factors. To address this changing clinical need, studies were conducted to evaluate infrared methods for assessing secondary lesion activity. We employed modified permeability measurements previously developed to assess the activity of secondary caries lesions. The results suggest that the permeability increased significantly with increasing integrated reflectivity. Furthermore, small increases in integrated reflectivity led to large permeability changes. Increasing transparent surface layer thickness led to decreased permeability of lesions, potentially indicating an arrest in activity at thicknesses exceeding 70 μm . SWIR imaging performed better than thermal imaging for activity assessment for secondary caries lesions on tooth coronal surfaces. Thermal imaging performed well in identifying crevices between composite material and tooth structure, but at times can be masked by the complex topography of the occlusal anatomy. SWIR imaging did not appear as susceptible to such interference, owing to the ability to differentiate composite materials, tooth structures, and lesions with high contrast.

In all, permeability measurements performed best on smooth surface lesions. These results further substantiated the usefulness of SWIR permeability measurements and OCT as promising methods for assessing secondary lesion activity and severity.

With imaging technology becoming more miniaturized and 3D CAD and printing techniques now more available, fabrication of small handheld probes allows for conducting studies to determine the suitability of employing infrared methods for lesion activity assessment. Preclinical studies demonstrated that a 3D printed appliance with integrated air for SWIR and thermal dehydration can be used to acquire permeability measurements similar to those acquired previously by benchtop imaging systems.

8.2.3 *In Vivo Lesion Activity Assessments*

The culmination of promising results from previous *in vitro* and *ex vivo* studies have provided evidence for further evaluation of these infrared imaging methods in clinical settings *in vivo*. A small pilot study with 30 patients was conducted to determine the use of CP-OCT to detect the transparent surface zone that is indicative of arrested lesions *in vivo*. Short SWIR and thermal dehydration sessions were also conducted concurrently to determine the permeability of identified lesions and assess their activity. CP-OCT was also used to measure lesion shrinkage during drying.

Based on the initial results of this pilot clinical study, thermal and CP-OCT imaging appear highly promising for the clinical assessment of lesion activity on root surfaces. The mean shrinkage for those 12 samples in which the surface position could be matched before and after drying was more than 60 μm , which can be easily measured with OCT. However, SWIR permeability measurement did not work as well for root lesions due to the confounding optical behavior of dentin and the tissues surrounding the lesions. This study demonstrated that thermal and CP-OCT imaging have great potential for the *in vivo* assessment of the activity of root caries lesions in a single appointment.

8.2 Future Perspective

The course of developing non-ionizing and more efficacious and accurate methods for assessing lesion activity have resulted in promising outcomes for future development. However, existing limitations remain that will need to be overcome for successful implementation into the clinic. The presence of the highly mineralized transparent surface zone was used as the hallmark for an arrested lesion surface with the caveat that this is not a gold standard. Although the validity of this approach is supported by good agreement of histopathology and CP-OCT images for *in vitro* studies, transparent surface zones are not yet a gold standard to determine whether a lesion surface is arrested. A reason for this is because SWIR and OCT imaging methods have not yet been widely accepted as established diagnostic techniques in clinical dentistry. Another reason might be that the current gold standard requires sectioning the teeth for imaging with traditional histology methods such as TMR and PLM. Even though not suitable for clinical use, MicroCT presents a less labor-intensive and more accurate analysis of histology for whole tooth samples. Additional studies are underway to further correlate the transparent surface layer measured by OCT with the surface layer measured by MicroCT. The purpose is to be able to further specify the portions of lesion surface zone that is remineralized to a similar mineral level to that of sound enamel or dentin for the assessment of lesion severity. Results from these studies might further confirm the hypotheses and introduce more future clinical studies or trials. The next step may include studies that identify the chemical and ionic composition of the transparent surface layer, and whether such layers are likely to endure further demineralizing challenges within *in vitro* and *in vivo* environments.

At present, an ongoing *in vivo* study in the lab that utilizes SWIR dehydration for measuring permeability of suspected coronal lesions in pediatric patients have alluded to some limitations. In the preliminary image analysis, saliva pooling on the lesion area seemed to interfere with the dehydration process thereby confounding the results. Furthermore, as revealed from recent *in vivo* studies, movement artifacts during imaging presents a challenge for image analyses.

Development of an isolation system in combination with a bite-block system that is familiar to clinicians and patients in dentistry may help with excluding saliva from lesion areas while providing necessary support to prevent movement during drying and imaging.

While the studies presented here have shown high potential for monitoring lesion status, future efforts should be devoted to evaluating if these imaging methods can be used to monitor remineralization efforts over time. Clinical follow-up *in vivo* studies will be important to establish how active lesions respond to treatment *in vivo* under clinically relevant timescales. These permeability imaging techniques can also be used to evaluate clinical work (e.g., presence of gap and roughness of restoration at initial placement) and study the life cycle of different restorative materials after placement.

The purpose of this work was to provide more foundational knowledge for the use of non-ionizing optical methods for assessing lesion activity, and to further identify and specify the advantages and limitations for its utility in clinical dentistry. One remaining issue is the potential cost of infrared imaging devices. High resolution thermal imaging arrays have decreased in cost by orders of magnitude over the past two decades and are now affordable for use in dentistry. InGaAs imaging devices required for SWIR imaging have also decreased in cost while improving in imaging performance, though devices are still somewhat expensive for use in dentistry. However, if InGaAs costs continue to decline at the same rate as the past two decades and alternative semiconductor technologies become available, the cost of devices will soon be practical for dental use. With newer and faster SWIR and infrared imaging technologies and better mechanical components, more affordable manufacturing options may give way to the adaptation of infrared methods for lesion activity assessments as part of routine dental exams for the public.

REFERENCES

- Almaz, E. C., Simon, J. C., Fried, D., & Darling, C. L. (2016). Influence of stains on lesion contrast in the pits and fissures of tooth occlusal surfaces from 800–1600-nm. *Proceedings of SPIE--the International Society for Optical Engineering*, 9692, 96920X. <https://doi.org/10.1117/12.2218663>
- Amaechi, B. T., Podoleanu, A. G., Komarov, G., Higham, S. M., & Jackson, D. A. (2004). Quantification of root caries using optical coherence tomography and microradiography: A correlational study. *Oral Health & Preventive Dentistry*, 2(4), 377–382.
- Ando, M., Ferreira-Zandoná, A. G., Eckert, G. J., Zero, D. T., & Stookey, G. K. (2017). Pilot clinical study to assess caries lesion activity using quantitative light-induced fluorescence during dehydration. *Journal of Biomedical Optics*, 22(3), 35005. <https://doi.org/10.1117/1.JBO.22.3.035005>
- Ando, M., Sharp, N., & Adams, D. (2012). Pulse thermography for quantitative nondestructive evaluation of sound, de-mineralized and re-mineralized enamel. *Health Monitoring of Structural and Biological Systems* 2012, 8348, 212–218. <https://doi.org/10.1117/12.914371>
- Arends, J., Ruben, J. L., & Inaba, D. (1997). Major topics in quantitative microradiography of enamel and dentin: R parameter, mineral distribution visualization, and hyper-remineralization. *Advances in Dental Research*, 11(4), 403–414.
- Banting, D. W. (1993). Diagnosis and Prediction of Root Caries. *Advances in Dental Research*, 7(2), 80–86. <https://doi.org/10.1177/08959374930070021901>
- Banting, D. W. (2001). The Diagnosis of Root Caries. *Journal of Dental Education*, 65(10), 991–996. <https://doi.org/10.1002/j.0022-0337.2001.65.10.tb03475.x>
- Baumgartner, A., Dichtl, S., Hitzemberger, C. K., Sattmann, H., Robl, B., Moritz, A., Fercher, A. F., & Sperr, W. (1999). Polarization–Sensitive Optical Coherence Tomography of Dental Structures. *Caries Research*, 34(1), 59–69. <https://doi.org/10.1159/000016571>

- Cate, J. M., & Amerongen, J. P. (1996). *Caries diagnosis, conventional methods*. Indiana University School of Dentistry. <http://dare.uva.nl/record/1/123460>
- Cate, J. M., & Arends, J. (1977). Remineralization of artificial enamel lesions in vitro. *Caries Research*, 11(5), 277–286. <https://doi.org/10.1159/000260279>
- Chan, K. H., Chan, A. C., Fried, W. A., Simon, J. C., Darling, C. L., & Fried, D. (2015). Use of 2D images of depth and integrated reflectivity to represent the severity of demineralization in cross-polarization optical coherence tomography. *Journal of Biophotonics*, 8(1–2), 36–45. <https://doi.org/10.1002/jbio.201300137>
- Chan, K. H., & Fried, D. (2018). Multispectral cross-polarization reflectance measurements suggest high contrast of demineralization on tooth surfaces at wavelengths beyond 1300 nm due to reduced light scattering in sound enamel. *Journal of Biomedical Optics*, 23(6), 060501. <https://doi.org/10.1117/1.JBO.23.6.060501>
- Chan, K. H., Tom, H., Lee, R. C., Kang, H., Simon, J. C., Staninec, M., Darling, C. L., Pelzner, R. B., & Fried, D. (2016). Clinical Monitoring of Smooth Surface Enamel Lesions Using CP-OCT During Nonsurgical Intervention. *Lasers in Surgery and Medicine*, 48(10), 915–923. <https://doi.org/10.1002/lsm.22500>
- Chang, N.-Y. N., Abdelaziz, M., & Fried, D. (2019). The relationship of dehydration rate and transparent surface layer thickness for coronal lesions on extracted teeth. *Lasers in Dentistry XXV*, 10857, 34–38. <https://doi.org/10.1117/12.2512921>
- Chang, N.-Y. N., Jew, J. M., & Fried, D. (2018). Lesion Dehydration Rate Changes with the Surface Layer Thickness during Enamel Remineralization. *Proceedings of SPIE--the International Society for Optical Engineering*, 10473. <https://doi.org/10.1117/12.2296023>
- Chang, N.-Y., Zhu, Y., Curtis, D., Le, O., Yang, V., Fried, W. A., Simon, J. C., Banan, P., Darling, C. L., & Fried, D. (2020). SWIR, thermal and CP-OCT imaging probes for the in vivo assessment of the activity of root caries lesions. *Lasers in Dentistry XXVI*, 11217, 23–28. <https://doi.org/10.1117/12.2550982>

- Chauncey, H. H., Glass, R. L., & Alman, J. E. (1989). Dental caries. Principal cause of tooth extraction in a sample of US male adults. *Caries Research*, 23(3), 200–205.
- Chen, Y., Otis, L., Piao, D., & Zhu, Q. (2005). Characterization of dentin, enamel, and carious lesions by a polarization-sensitive optical coherence tomography system. *Applied Optics*, 44(11), 2041. <https://doi.org/10.1364/AO.44.002041>
- Chong, S. L., Darling, C. L., & Fried, D. (2007). Nondestructive measurement of the inhibition of demineralization on smooth surfaces using polarization-sensitive optical coherence tomography. *Lasers in Surgery and Medicine*, 39(5), 422–427. <https://doi.org/10.1002/lsm.20506>
- Chung, S., Fried, D., Staninec, M., & Darling, C. L. (2011). Multispectral near-IR reflectance and transillumination imaging of teeth. *Biomedical Optics Express*, 2(10), 2804–2814. <https://doi.org/10.1364/BOE.2.002804>
- Dean, J. A. (2015). *McDonald and Avery's Dentistry for the Child and Adolescent*. Elsevier Health Sciences.
- Dye, B. A., Tan, S., Smith, V., Barker, L. K., Thornton-Evans, G., Eke, P. I., & Beltrán-Aguilar, E. D. (2007). *Trends in oral health status; United States, 1988-1994 and 1999-2004*.
- Dye, B., Thornton-Evans, G., Li, X., & Iafolla, T. (2015). Dental caries and tooth loss in adults in the United States, 2011-2012. *NCHS Data Brief*, 197, 197.
- Eke, P. I., Thornton-Evans, G. O., Wei, L., Borgnakke, W. S., Dye, B. A., & Genco, R. J. (2018). Periodontitis in US Adults: National Health and Nutrition Examination Survey 2009-2014. *The Journal of the American Dental Association*, 149(7), 576-588.e6. <https://doi.org/10.1016/j.adaj.2018.04.023>
- Ekstrand, K., Martignon, S., & Holm-Pedersen, P. (2008). Development and evaluation of two root caries controlling programmes for home-based frail people older than 75 years. *Gerodontology*, 25(2), 67–75. <https://doi.org/10.1111/j.1741-2358.2007.00200.x>

- Featherstone, J. D. B. (1996). Clinical implications: New strategies for caries prevention. *Indiana Conference*, 287–295.
- Featherstone, J. D. B. (1999). Prevention and reversal of dental caries: Role of low level fluoride. *Community Dentistry and Oral Epidemiology*, 27(1), 31–40. <https://doi.org/10.1111/j.1600-0528.1999.tb01989.x>
- Fejerskov, O., & Kidd, E. (2003). *Dental Caries: The Disease and its Clinical Management* Blackwell. Oxford.
- Fejerskov, O., Luan, W. M., Nyvad, B., Budtz-Jørgensen, E., & Holm-Pedersen, P. (1991). Active and Inactive Root Surface Caries Lesions in a Selected Group of 60- to 80-Year-Old Danes. *Caries Research*, 25(5), 385–391. <https://doi.org/10.1159/000261396>
- Fried, D., Glana, R. E., Featherstone, J. D. B., & Seka, W. (1995). Nature of light scattering in dental enamel and dentin at visible and near-infrared wavelengths. *Applied Optics*, 34(7), 1278–1285. <https://doi.org/10.1364/AO.34.001278>
- Fried, D., Xie, J., Shafi, S., Featherstone, J. D. B., Breunig, T. M., & Le, C. (2002). Imaging caries lesions and lesion progression with polarization sensitive optical coherence tomography. *Journal of Biomedical Optics*, 7(4), 618–627. <https://doi.org/10.1117/1.1509752>
- Fried, W. A., Abdelaziz, M., Darling, C. L., & Fried, D. (2021). High Contrast Reflectance Imaging of Enamel Demineralization and Remineralization at 1950-nm for the Assessment of Lesion Activity. *Lasers in Surgery and Medicine*, 53(7), 968–977. <https://doi.org/10.1002/lsm.23371>
- Fried, W. A., Fried, D., Chan, K. H., & Darling, C. L. (2013). High contrast reflectance imaging of simulated lesions on tooth occlusal surfaces at near-IR wavelengths. *Lasers in Surgery and Medicine*, 45(8), 533–541. <https://doi.org/10.1002/lsm.22159>
- Fried, W. A., Simon, J. C., Darling, C. L., Le, O., & Fried, D. (2017). High-contrast reflectance imaging of composite restorations color-matched to tooth structure at 1000-2300-nm. *Lasers in Dentistry XXIII*, 10044, 45–50. <https://doi.org/10.1117/12.2256733>

- Fried, W. A., Zhu, Y., Yang, V., Chang, N.-Y., & Fried, D. (2020). A SWIR imaging handpiece for the clinical assessment of lesion activity via dehydration: Preclinical assessment. *Lasers in Dentistry XXVI*, 11217, 67–70. <https://doi.org/10.1117/12.2550981>
- Gordan, V. V., Riley, J. L., Geraldeli, S., Rindal, D. B., Qvist, V., Fellows, J. L., Kellum, H. P., & Gilbert, G. H. (2012). Repair or replacement of defective restorations by dentists in The Dental PBRN. *Journal of the American Dental Association (1939)*, 143(6), 593–601.
- Hale, G. M., & Querry, M. R. (1973). Optical Constants of Water in the 200-nm to 200- μ m Wavelength Region. *Applied Optics*, 12(3), 555–563. <https://doi.org/10.1364/AO.12.000555>
- Hee, M. R., Swanson, E. A., Fujimoto, J. G., & Huang, D. (1992). Polarization-sensitive low-coherence reflectometer for birefringence characterization and ranging. *Journal of the Optical Society of America B*, 9(6), 903. <https://doi.org/10.1364/JOSAB.9.000903>
- Hellyer, P. H., Beighton, D., Heath, M. R., & Lynch, E. J. (1990). Root caries in older people attending a general dental practice in East Sussex. *British Dental Journal*, 169(7), 201–206. <https://doi.org/10.1038/sj.bdj.4807326>
- Hume, W. R. (1996). Need for change in dental caries diagnosis. *Early Detection of Dental Caries. Indianapolis: Indiana University*, 1–10.
- Ismail, A. I. (2005). Rationale and Evidence for the International Caries Detection and Assessment System (ICDAS II). *ResearchGate*. https://www.researchgate.net/publication/267383865_Rationale_and_Evidence_for_the_International_Caries_Detection_and_Assessment_System_ICDAS_II
- Jones, R. S., Darling, C. L., Featherstone, J. D. B., & Fried, D. (2006). Remineralization of in vitro dental caries assessed with polarization-sensitive optical coherence tomography. *Journal of Biomedical Optics*, 11(1), 014016-014016–014019. <https://doi.org/10.1117/1.2161192>
- Jones, R. S., & Fried, D. (2002). Attenuation of 1310- and 1550-nm laser light through sound dental enamel. *Lasers in Dentistry VIII*, 4610, 187–190. <https://doi.org/10.1117/12.469324>

- Jones, R. S., & Fried, D. (2006). Remineralization of Enamel Caries Can Decrease Optical Reflectivity. *Journal of Dental Research*, 85(9), 804–808. <https://doi.org/10.1177/154405910608500905>
- Jones, R. S., Staninec, M., & Fried, D. (2004). Imaging artificial caries under composite sealants and restorations. *Journal of Biomedical Optics*, 9(6), 1297–1304. <https://doi.org/10.1117/1.1805562>
- Kaneko, K., Matsuyama, K., & Nakashima, S. (1999). Quantification of early carious enamel lesions by using an infrared camera in vitro. *Proceedings of the 4th Annual Indiana Conference*, 83–100.
- Kang, H., Darling, C. L., & Fried, D. (2012). Nondestructive monitoring of the repair of enamel artificial lesions by an acidic remineralization model using polarization-sensitive optical coherence tomography. *Dental Materials*, 28(5), 488–494. <https://doi.org/10.1016/j.dental.2011.11.020>
- Kaste, L., Selwitz, R., Oldakowski, R., Brunelle, J., Winn, D., & Brown, L. (1996). Coronal caries in the primary and permanent dentition of children and adolescents 1-17 years of age: United States, 1988-1991. *Journal of Dental Research*, 75 Spec No, 631–641.
- Kidd, E. A. (1983). The histopathology of enamel caries in young and old permanent teeth. *British Dental Journal*, 155(6), 196–198. <https://doi.org/10.1038/sj.bdj.4805177>
- Kidd, E. A. M., & Fejerskov, O. (2004). What Constitutes Dental Caries? Histopathology of Carious Enamel and Dentin Related to the Action of Cariogenic Biofilms. *Journal of Dental Research*, 83(1_suppl), 35–38. <https://doi.org/10.1177/154405910408301s07>
- Kinney, J. H., Balooch, M., Marshall, G. W., & Marshall, S. J. (1993). Atomic-force microscopic study of dimensional changes in human dentine during drying. *Archives of Oral Biology*, 38(11), 1003–1007. [https://doi.org/10.1016/0003-9969\(93\)90114-2](https://doi.org/10.1016/0003-9969(93)90114-2)

- Lee, M. H., Darling, C. L., & Fried, D. (2010). Automated analysis of lesion depth and integrated reflectivity in PS-OCT scans of tooth demineralization. *Lasers in Surgery and Medicine*, 42(1), 62–68. <https://doi.org/10.1002/lsm.20862>
- Lee, C., Darling, C. L., & Fried, D. (2009). Polarization Sensitive Optical Coherence Tomographic Imaging of Artificial Demineralization on Exposed Surfaces of Tooth Roots. *Dental Materials: Official Publication of the Academy of Dental Materials*, 25(6), 721–728. <https://doi.org/10.1016/j.dental.2008.11.014>
- Lee, R. C., Darling, C. L., & Fried, D. (2015). Assessment of remineralization via measurement of dehydration rates with thermal and near-IR reflectance imaging. *Journal of Dentistry*, 43(8), 1032–1042. <https://doi.org/10.1016/j.jdent.2015.03.005>
- Lee, R. C., Darling, C. L., & Fried, D. (2016a). Assessment of remineralization in simulated enamel lesions via dehydration with near-IR reflectance imaging. *Lasers in Dentistry XXI; Proc SPIE*, 9306, H1-6. <https://doi.org/10.1117/12.2083655>
- Lee, R. C., Darling, C. L., & Fried, D. (2016b). Assessment of remineralized dentin lesions with thermal and near-infrared reflectance imaging. *Lasers in Dentistry XXII; Proc SPIE*, 9692, B1-5. <https://doi.org/10.1117/12.2218661>
- Lee, R. C., Darling, C. L., Staninec, M., Ragadio, A., & Fried, D. (2016). Activity assessment of root caries lesions with thermal and near-IR imaging methods. *Journal of Biophotonics*, (in press). <https://doi.org/10.1002/jbio.201500333>
- Lee, R. C., Darling, C. L., Staninec, M., Ragadio, A., & Fried, D. (2017). Activity assessment of root caries lesions with thermal and near-IR imaging methods. *Journal of Biophotonics*, 10(3), 433–445. <https://doi.org/10.1002/jbio.201500333>
- Lee, R. C., Kang, H., Darling, C. L., & Fried, D. (2014). Automated assessment of the remineralization of artificial enamel lesions with polarization-sensitive optical coherence tomography. *Biomedical Optics Express*, 5(9), 2950–2962. <https://doi.org/10.1364/BOE.5.002950>

- Lee, R. C., Staninec, M., Le, O., & Fried, D. (2016). Infrared Methods for Assessment of the Activity of Natural Enamel Caries Lesions. *IEEE Journal of Selected Topics in Quantum Electronics*, 22(3), 102–110. <https://doi.org/10.1109/JSTQE.2016.2542481>
- Lepri, T. P., Colucci, V., Turssi, C. P., & Corona, S. A. M. (2013). Permeability of eroded enamel following application of different fluoride gels and CO2 laser. *Lasers in Medical Science*, 28(1), 235–240. <https://doi.org/10.1007/s10103-012-1123-2>
- Lin, M., Liu, Q. D., Xu, F., Bai, B. F., & Lu, T. J. (2009). In vitro investigation of heat transfer in human tooth. *Fourth International Conference on Experimental Mechanics; Proc SPIE*, 7522, N1-7. <https://doi.org/10.1117/12.851623>
- Logan, C. M., Co, K. U., Fried, W. A., Simon, J. C., Staninec, M., and, D. F., & Darling, C. L. (2014). Multispectral Near-Infrared Imaging of Composite Restorations in Extracted Teeth. *Proceedings of SPIE--the International Society for Optical Engineering*, 8929, 89290R. <https://doi.org/10.1117/12.2045687>
- Lynch, E., & Beighton, D. (1994). A Comparison of Primary Root Caries Lesions Classified According to Colour. *Caries Research*, 28(4), 233–239. <https://doi.org/10.1159/000261971>
- Mandurah, M., Sadr, A., Shimada, Y., Kitasako, Y., Nakashima, S., Bakhsh, T. A., Tagami, J., & Sumi, Y. (2013). Monitoring remineralization of enamel subsurface lesions by optical coherence tomography. *Journal of Biomedical Optics*, 18(4), 046006. <https://doi.org/10.1117/1.JBO.18.4.046006>
- Manesh, S. K., Darling, C. L., & Fried, D. (2009a). Polarization-sensitive optical coherence tomography for the nondestructive assessment of the remineralization of dentin. *Journal of Biomedical Optics*, 14(4), 044002. <https://doi.org/10.1117/1.3158995>
- Manesh, S. K., Darling, C. L., & Fried, D. (2009b). Nondestructive assessment of dentin demineralization using polarization-sensitive optical coherence tomography after

- exposure to fluoride and laser irradiation. *Journal of Biomedical Materials Research Part B: Applied Biomaterials*, 90B(2), 802–812. <https://doi.org/10.1002/jbm.b.31349>
- National Institutes of Health (U.S.). (2001). Diagnosis and management of dental caries throughout life. *NIH Consensus Statement*, 18(1), 1–23.
- Nee, A., Chan, K., Kang, H., Staninec, M., Darling, C. L., & Fried, D. (2014). Longitudinal monitoring of demineralization peripheral to orthodontic brackets using cross polarization optical coherence tomography. *Journal of Dentistry*, 42(5), 547–555. <https://doi.org/10.1016/j.jdent.2014.02.011>
- Neville, B. W., Damm, D. D., Chi, A. C., & Allen, C. M. (2015). *Oral and Maxillofacial Pathology*. Elsevier Health Sciences.
- Ng, C., Almaz, E. C., Simon, J. C., Fried, D., & Darling, C. L. (2019). Near-infrared imaging of demineralization on the occlusal surfaces of teeth without the interference of stains. *Journal of Biomedical Optics*, 24(3), 036002. <https://doi.org/10.1117/1.JBO.24.3.036002>
- Ngaotheppitak, P., Darling, C. L., & Fried, D. (2005). Measurement of the severity of natural smooth surface (interproximal) caries lesions with polarization sensitive optical coherence tomography. *Lasers in Surgery and Medicine*, 37(1), 78–88. <https://doi.org/10.1002/lsm.20169>
- Özok, A. R., Wu, M.-K., ten Cate, J. M., & Wesselink, P. R. (2002). Effect of Perfusion with Water on Demineralization of Human Dentin in vitro. *Journal of Dental Research*, 81(11), 733–737. <https://doi.org/10.1177/0810733>
- Pitts, N. (2009). *Detection, Assessment, Diagnosis and Monitoring of Caries*. Karger Medical and Scientific Publishers.
- Ribeiro, F. V., Hirata, D. Y., Reis, A. F., Santos, V. R., Miranda, T. S., Faveri, M., & Duarte, P. M. (2014). Open-Flap Versus Flapless Esthetic Crown Lengthening: 12-Month Clinical Outcomes of a Randomized Controlled Clinical Trial. *Journal of Periodontology*, 85(4), 536–544. <https://doi.org/10.1902/jop.2013.130145>

- Saunders, R., & Handelman, S. (1991). Coronal and root decay in institutionalized older adults. *The New York State Dental Journal*, 57(8), 25–28.
- Schaecken, M. J. M., Keltjens, H. M. A. M., & Van Der Hoeven, J. S. (1991). Effects of Fluoride and Chlorhexidine on the Microflora of Dental Root Surfaces and Progression of Root-surface Caries. *Journal of Dental Research*, 70(2), 150–153. <https://doi.org/10.1177/00220345910700021101>
- Schüpbach, P., Lutz, F., & Guggenheim, B. (1992). Human Root Caries: Histopathology of Arrested Lesions. *Caries Research*, 26(3), 153–164. <https://doi.org/10.1159/000261436>
- Simon, J. C., A. Lucas, S., Lee, R. C., Darling, C. L., Staninec, M., Vaderhobli, R., Pelzner, R., & Fried, D. (2016). Near-infrared imaging of secondary caries lesions around composite restorations at wavelengths from 1300–1700-nm. *Dental Materials*, 32(4), 587–595. <https://doi.org/10.1016/j.dental.2016.01.008>
- Simon, J. C., Chan, K. H., Darling, C. L., & Fried, D. (2014). Multispectral near-IR reflectance imaging of simulated early occlusal lesions: Variation of lesion contrast with lesion depth and severity. *Lasers in Surgery and Medicine*, 46(3), 203–215. <https://doi.org/10.1002/lsm.22216>
- Simon, J. C., Kang, H., Staninec, M., Jang, A. T., Chan, K. H., Darling, C. L., Lee, R. C., & Fried, D. (2017). Near-IR and CP-OCT Imaging of Suspected Occlusal Caries Lesions. *Lasers in Surgery and Medicine*, 49(3), 215–224. <https://doi.org/10.1002/lsm.22641>
- Stahl, J., Kang, H., & Fried, D. (2010). Imaging Simulated Secondary Caries Lesions with Cross Polarization OCT. *Proceedings of SPIE--the International Society for Optical Engineering*, 7549, 754905.
- Staninec, M., Douglas, S. M., Darling, C. L., Chan, K., Kang, H., Lee, R. C., & Fried, D. (2011). Non-destructive clinical assessment of occlusal caries lesions using near-IR imaging methods. *Lasers in Surgery and Medicine*, 43(10), 951–959. <https://doi.org/10.1002/lsm.21139>

- Staninec, M., Lee, C., Darling, C. L., & Fried, D. (2010). In vivo near-IR imaging of approximal dental decay at 1,310 nm. *Lasers in Surgery and Medicine*, 42(4), 292–298. <https://doi.org/10.1002/lsm.20913>
- ten Cate, J. M., & Featherstone, J. D. B. (1991). Mechanistic Aspects of the Interactions Between Fluoride and Dental Enamel. *Critical Reviews in Oral Biology & Medicine*, 2(3), 283–296. <https://doi.org/10.1177/10454411910020030101>
- Tressel, J., Abdelaziz, M., & Fried, D. (2021). High contrast reflectance imaging at 1950-nm for the assessment of lesion activity on extracted teeth. *Photonic Therapeutics and Diagnostics in Dentistry, Head and Neck Surgery, and Otolaryngology*, 11627, 43–48. <https://doi.org/10.1117/12.2584909>
- Tressel, J. T., Abdelaziz, M., & Fried, D. (2021). Dynamic SWIR imaging near the 1950-nm water absorption band for caries lesion diagnosis. *Journal of Biomedical Optics*, 26(5), 056006. <https://doi.org/10.1117/1.JBO.26.5.056006>
- Usenik, P., Bürmen, M., Fidler, A., Pernuš, F., & Likar, B. (2014). Near-infrared hyperspectral imaging of water evaporation dynamics for early detection of incipient caries. *Journal of Dentistry*, 42(10), 1242–1247. <https://doi.org/10.1016/j.jdent.2014.08.007>
- Wada, I., Shimada, Y., Ikeda, M., Sadr, A., Nakashima, S., Tagami, J., & Sumi, Y. (2015). Clinical assessment of non carious cervical lesion using swept-source optical coherence tomography. *Journal of Biophotonics*, 8(10), 846–854. <https://doi.org/10.1002/jbio.201400113>
- White, S. C., & Pharoah, M. J. (2014). *Oral Radiology: Principles and Interpretation*. Elsevier Health Sciences.
- Winn, D., Brunelle, J., Selwitz, R., Kaste, L., Oldakowski, R., Kingman, A., & Brown, L. (1996). Coronal and root caries in the dentition of adults in the United States, 1988-1991. *Journal of Dental Research*, 75 Spec No, 642–651.

- Wu, J., & Fried, D. (2009). High Contrast Near-infrared Polarized Reflectance Images of Demineralization on Tooth Buccal and Occlusal Surfaces at $\lambda=1310\text{-nm}$. *Lasers in Surgery and Medicine*, 41(3), 208–213. <https://doi.org/10.1002/lsm.20746>
- Yamazaki, H., Litman, A., & Margolis, H. C. (2007). Effect of fluoride on artificial caries lesion progression and repair in human enamel: Regulation of mineral deposition and dissolution under in vivo-like conditions. *Archives of Oral Biology*, 52(2), 110–120. <https://doi.org/10.1016/j.archoralbio.2006.08.012>
- Yamazaki, H., & Margolis, H. C. (2008). Enhanced Enamel Remineralization under Acidic Conditions in vitro. *Journal of Dental Research*, 87(6), 569–574. <https://doi.org/10.1177/154405910808700612>
- Yang, J., & Dutra, V. (2005). Utility of radiology, laser fluorescence, and transillumination. *Dental Clinics of North America*, 49(4), 739–752.
- Yang, V. B., Chang, N.-Y., & Fried, D. (2020). A thermal imaging handpiece for the clinical assessment of lesion activity on root surfaces via dehydration. *Proceedings of SPIE--the International Society for Optical Engineering*, 11217, 112170H. <https://doi.org/10.1117/12.2550977>
- Yang, V. B., Curtis, D. A., & Fried, D. (2018). Cross-polarization reflectance imaging of root caries and dental calculus on extracted teeth at wavelengths from 400 to 2350 nm. *Journal of Biophotonics*, 11(11), e201800113. <https://doi.org/10.1002/jbio.201800113>
- Yang, V. B., & Fried, D. (2019). An appliance for monitoring the shrinkage of root caries with OCT. *Proceedings of SPIE--the International Society for Optical Engineering*, 10857, 108570L. <https://doi.org/10.1117/12.2512933>
- Yang, V., & Fried, D. (2019). Measurement of the shrinkage of natural and simulated lesions on root surfaces using CP-OCT. *Journal of Dentistry*, 90, 103213. <https://doi.org/10.1016/j.jdent.2019.103213>

- Yang, V., Zhu, Y., Curtis, D., Le, O., Chang, N. Y. N., Fried, W. A., Simon, J. C., Banan, P., Darling, C. L., & Fried, D. (2020). Thermal Imaging of Root Caries In Vivo. *Journal of Dental Research*, 99(13), 1502–1508. <https://doi.org/10.1177/0022034520951157>
- Zakian, C. M., Taylor, A. M., Ellwood, R. P., & Pretty, I. A. (2010). Occlusal caries detection by using thermal imaging. *Journal of Dentistry*, 38(10), 788–795. <https://doi.org/10.1016/j.jdent.2010.06.010>
- Zhu, Y., & Fried, D. (2022). Measurement of the Depth of Lesions on Proximal Surfaces with SWIR Multispectral Transillumination and Reflectance Imaging. *Diagnostics*, 12(3), 597. <https://doi.org/10.3390/diagnostics12030597>
- Zuluaga, A. F., Yang, V., Jabbour, J., Ford, T., Kemp, N., & Fried, D. (2019). Real-time visualization of hidden occlusal and approximal lesions with an OCT dental handpiece (Conference Presentation). *Lasers in Dentistry XXV*, 10857, 108570E. <https://doi.org/10.1117/12.2513442>

Publishing Agreement

It is the policy of the University to encourage open access and broad distribution of all theses, dissertations, and manuscripts. The Graduate Division will facilitate the distribution of UCSF theses, dissertations, and manuscripts to the UCSF Library for open access and distribution. UCSF will make such theses, dissertations, and manuscripts accessible to the public and will take reasonable steps to preserve these works in perpetuity.

I hereby grant the non-exclusive, perpetual right to The Regents of the University of California to reproduce, publicly display, distribute, preserve, and publish copies of my thesis, dissertation, or manuscript in any form or media, now existing or later derived, including access online for teaching, research, and public service purposes.

DocuSigned by:

Nai-Yuan Nicholas Chang

9867282323D149C...

Author Signature

4/19/2022

Date